THE UNIVERSITY
of ADELAIDE

FACULTY OF SCIENCES
SCHOOL OF PHYSICAL SCIENCES

High precision measurement of optical absorption in ultra-low-OH fused silica at wavelengths near 2 µm

Craig Ingram

Supervisors:
Prof. Peter VEITCH
Prof. David OTTAWAY
Dr Sebastian NG

For Kirsten, Phoebe and Heather

Contents

Abstract ix

Statement of Originallity xi

Acknowledgements xiii

List of Figures xvii

List of Tables xix

1 Introduction 1
- 1.1 Gravitational-waves . . . 1
- 1.2 Detector Design . . . 4
- 1.3 Detector Noise Sources . . . 6
  - 1.3.1 Seismic and Newtonian Noise . . . 8
  - 1.3.2 Thermal Noise . . . 9
  - 1.3.3 Quantum Noise . . . 10
- 1.4 Squeezed Light . . . 11
- 1.5 Thermal Compensation System . . . 12
  - 1.5.1 HWS measurement system . . . 15
- 1.6 Voyager Upgrade . . . 16
- 1.7 Project aims . . . 20
- 1.8 Thesis structure . . . 21

2 Optical Loss in Transparent Media 23
- 2.1 Loss Mechanisms . . . 24
  - 2.1.1 Fresnel Reflections . . . 24
  - 2.1.2 Diffraction losses due to surface roughness . . . 25
  - 2.1.3 Rayleigh scattering . . . 25
  - 2.1.4 Mie Scattering . . . 26
  - 2.1.5 Brillouin Scattering . . . 27
  - 2.1.6 Raman Scattering . . . 27
  - 2.1.7 Intrinsic Absorption . . . 28
    - Multi-phonon absorption . . . 28
  - 2.1.8 Extrinsic Absorption . . . 29
- 2.2 Review of Measurement Techniques . . . 29
  - 2.2.1 Transmission Measurements . . . 30
    - Spectrophotometry . . . 30
    - Fourier-Transform Infra-Red Spectroscopy . . . 30
    - Cut Back Techniques . . . 31
- 2.3 Thermal lensing techniques . . . 32
  - 2.3.1 GEO600 . . . 32

2.4 Photothermal Deflection Techniques . . . 34
2.4.1 Colinear Mirage Bench . . . 34
2.4.2 Photothermal Common-path Interferometry . . . 35
2.4.3 Shack-Hartmann wavefront detector . . . 36
2.5 Summary . . . 37

3 Absorption Measurement System 39
3.1 Coaxial photothermal HWS measurement system . . . 40
3.2 Differential Hartmann Wavefront Sensor . . . 42
3.3 Centroiding . . . 47
3.4 Sensitivity of the HWS . . . 50
3.4.1 Characterisation of CCD camera . . . 50
CCD Noise . . . 51
3.4.2 Sensitivity of HWS . . . 52
3.5 Heating Beam . . . 58
3.6 HWS Probe Beam . . . 62
3.6.1 Removing sensitivity to intensity changes . . . 63
3.6.2 Minimising sensitivity to air currents . . . 63
3.6.3 Probe beam collimation . . . 64
3.6.4 colinearity of heating and probe beams . . . 66
3.7 Absorption in auxiliary optics . . . 67
3.8 Off-Axis Measurement . . . 72
3.8.1 Angle of incidence of heating beam . . . 73
3.8.2 Improving SNR in WFD maps . . . 74
3.9 Summary . . . 75

4 Quantifying Thermal Absorption 77
4.1 Description of Finite Element Analysis Model . . . 78
4.2 Validation of FEA model . . . 82
4.3 Calculation of absorption coefficient using FEA . . . 83
4.4 Sensitivity analysis for Finite Element Analysis (FEA) model . . . 87
4.4.1 Angle between heating and probe beams . . . 87
4.4.2 Heating Beam Size . . . 87
4.4.3 Sensitivity to length . . . 88
4.4.4 Summary . . . 89

5 Results 91
5.1 Reducing noise in HWS measurement . . . 91
5.2 Averaging of HWS images . . . 93
5.3 Absorption Coefficient in FS . . . 94
5.4 Discussion . . . 97

6 Conclusion 101
6.1 Summary . . . 101
6.2 Future work . . . 103

A Linear Approximation of Lambert Beer Law **105**

B Cartesian to spherical transformation **107**

C Thermal expansion **109**

D Variance in digital value **111**

Bibliography **119**

Abstract

The first detection of Gravitational Waves from a Binary Black Hole (BBH) inspiral in September 2015 heralded the beginning of a new age in Gravitational Wave astronomy. This has been further enhanced by the detection of a binary neutron inspiral in mid 2017 and has opened up a new era of multi-messenger astronomy.
To further increase detection rate in third generation gravitational wave interferometers numerous upgrades have been determined including a move to cryogenically cooled silicon test masses to reduce thermal noise and an increase in intra-cavity laser power in the interferometric optical cavities, which should reduce the shot-noise in the interferometer. This move to silicon test masses requires a shift to wavelengths longer than 1.3 µm as determined by the transparency of silicon.
It has been suggested that the compensation plates, beam-splitter and other optics be composed of Fused Silica. Small, but finite, absorption of optical power in the interferometer will result in thermal gradients within the optics of the detector leading to wavefront distortion of the cavity eigenmode. Therefore accurate measurement of the optical absorption is required to better determine the suitability of fused silica optics at these wavelengths. In this thesis, I describe a method determine the wavefront distortion and hence calculate the amount of optical absorption in fused silica at 2 µm. I shall describe a Hartmann Wavefront Sensor that can measure wavefront distortion such as that cased by substrate absorption with extremely high precision and accuracy.

Statement of Originality

I certify that this work contains no material which has been accepted for the award of any other degree or diploma in my name, in any university or other tertiary institution and, to the best of my knowledge and belief, contains no material previously published or written by another person, except where due reference has been made in the text. In addition, I certify that no part of this work will, in the future, be used in a submission in my name, for any other degree or diploma in any university or other tertiary institution without the prior approval of the University of Adelaide and where applicable, any partner institution responsible for the joint-award of this degree.

I give permission for the digital version of my thesis to be made available on the web, via the University's digital research repository, the Library Search and also through web search engines, unless permission has been granted by the University to restrict access for a period of time.

I acknowledge the support I have received for my research through the provision of an Australian Government Research Training Program Scholarship

List of Figures

1.1 Gravitational-wave spectrum 2
1.2 Time Domain data from GW150914 2
1.3 Gravitational-wave Quadroploe moment 4
1.4 A simplified optical layout of the Advanced LIGO interferometer . . . 5
1.5 Noise and range from second observing run. 5
1.6 Modelled sensitivity for aLIGO detector. 7
1.7 Noise curve for LVC detectors from O3. 8
1.8 Schematic of a system used in the aLIGO detectors. 9
1.9 Fused Silica (FS) suspension fibres 10
1.10 Shot noise and radiation pressure noise 11
1.11 Time series and phase space representation of stabilized laser. 12
1.12 Phasor diagram of coherent and squeezed state light. 13
1.13 Squeezing noise reduction 13
1.14 Thermo-refractive lensing and thermo-elastic deformation. 14
1.15 aLIGO Thermal Compensation System overview. 14
1.16 Diagrammatic representation of Working principle of the HWS 15
1.17 Evolution of spherical power due to thermal lensing 16
1.18 Hartmann image showing distortion due to a point absorber 17
1.19 Proposed strain sensitivity of LIGO Voyager 18
1.20 Typical transmission losses in Silicon and Fused Silica 19
1.21 Published absorption coefficient at 2 µm 20

2.1 Processes involved in light–matter interaction 23
2.2 Fresnel reflection ar FS/Air interface 25
2.3 Rayleigh and Mie scattering in relation to particle size 26
2.4 Contribution of scattering and absorption processes in FS 27
2.5 Illustration of the cutback technique to measure fibre loss. 31
2.6 GEO 600 layout 33
2.7 Colinear mirage setup 34
2.8 Alignment in colinear Mirage Setup 35
2.9 Schematic of Photothermal Common-Path Interferometry 36
2.10 Schematic of SH wavefront detector 37

3.1 Schematic of on-axis measurement system showing colinear probe and heating beams. 40
3.2 Transmission of dichroics at 45° angle of incidence measured using a Carry NIR UV VIS spectrophotometer. 41
3.3 Dual x, y translation stages used to align the test optic to ensure that it is normal to the probe beam while pins are used to support the optic while minimising thermal conduction. Low transmission at 830 nm due to Fresnel reflection which is not accounted for in Spectrometer measurement. 41

3.4 The Hartmann Wavefront Sensor. 43
3.5 False colour image example of a Hartmann spot pattern. 44
3.6 Representation of wavefront deformation 45
3.7 Example quiver plot showing discrete gradient field calculated. 46
3.8 Integrated wavefront change 46
3.9 Example of spot and centroiding using WCoG algorithm. 48
3.10 Average DN use determine hot pixels 49
3.11 Location of 'hot' pixels on CCD compared with centroid locations. . . 50
3.12 Experimental setup to test the precision of the Hartmann sensor using a single-mode fibre-coupled SLED that directly illuminates the sensor. 53
3.13 Hartmann sensor measurement of the background shot-noise level made by comparing two Hartmann images separated in time by approximately 10 seconds. Shown are a) the gradient field of the apparent wavefront change and b) a numerical reconstruction of the apparent wavefront change. 53
3.14 Wavefront slices showing noise floor 54
3.15 Graphic showing selection of frames for investigating noise reduction due to averaging. Reference centroids were created by averaging the first and last 500 images. 55
3.16 The improvement in HWS sensitivity due to averaging over N_{avg} Hartmann images. 55
3.17 Plots showing temperature dependence of the Hartmann Wavefront Sensor (HWS) gradient fields, (a) before and (b) after temperature stabilisation of the HWS camera. 57
3.18 Variation of camera temperature after stabilization, recorded using the PID temperature controller probe. 57
3.19 Dark noise vs temperature 58
3.20 Spectrum of 2 µm heating beam. 59
3.21 Power stability of 2 µm heating beam recorded using thermal power head showing the stability of the heating laser will not affect the measurement. 59
3.22 Data used to determine the thermal time constant of the 3002 FS rod. The plot shows spherical power response, (blue) and power incident on the front face of the test sample (red). 60
3.23 Estimating the thermal time constant of the 3002 FS by comparing the data from Figure 3.22 with an exponential decay 60
3.24 Simplified schematic showing experimental setup used to calibrate photodiode for continuous monitoring of power incident on test sample. 61
3.25 Power recoded at input face of test sample used to calibrate Photodiode such that constant monitoring of power was possible. 61
3.26 Image of heating beam at origin (a) and intensity profiles in x and y along test path. These images were used to determine beam size and collimation of the heating beam. 62

3.27 Spherical Power from consecutive Hartman images when experimental setup was open to the lab environment (blue) and enclosed (orange) showing an approximately 10x decrease in noise in the system. 64
3.28 Power Spectral Density of prism in x and y showing noise before (a,b) and after enclosing beam path (c,d) to reduce temperature fluctuations and air currents. 65
3.29 using triangulation to determine collimation of probe beam 66
3.30 Frequency histogram of triangle side lengths determined using Delauny triangulation 67
3.31 A gradient field due to the heating in two thin highly-absorbing glass slides when the probe beam is not colinear with the heating beam. . . 68
3.32 Wave Front Deformation (WFD) recorded with no test sample, showing absorption in auxiliary optics. 68
3.33 A third dichroic was placed between the output dichroic and the beam expanding telescope to investigate if 2 µm light was being absorbed in the optics of the beam expanding telescope and causing unwanted wavefront distortion. 69
3.34 The heating beam was misaligned such that it was incident only on the input dichroic to test effect on resulting WFD. 69
3.35 Hartmann image taken with 8 W incident power with heating beam misaligned to investigate absorption in a single dichroic mirror. 70
3.36 Numerical wavefront maps investigating the effect of absorption in (a) the dichroic mirror showing the absorption in a single dichroic mirror without the test sample in place and (b) with the test sample in place (heating beam is not incident on the sample) using experimental setup shown in Figure 3.34 used to investigate the dichroic absorption. . . . 70
3.37 Aberration showing similar structure in 24 cm test sample when images were separated in time by 60 seconds. 71
3.38 Wavefront map showing no matching structure in 24 cm test sample when images were separated by 180 seconds. 71
3.39 WFD maps before and after rotating the test sample by 5° for a time separation of about 60 seconds. 72
3.40 Schematic of off-axis photothermal measurement system. 72
3.41 To determine the angle of incidence the distance between the probe and heating beams and the distance to the centre of the optic were measured. The Angle Of Incidence, θ_i was determined to be 2.3°. . . 73
3.42 RMS Gradient vs number of frames averaged (N_{avg}) with and without test sample in place (no heating beam). For small (<100) frames averaged the noise is reduced as expected. This is not so for $N_{avg} >$ 100. The most likely cause of this is fluctuations in heating beam power and environmental noise during image capture. 74
3.43 Wavefront maps from two Hartmann image where $N_{avg} = 100$ taken 60 seconds apart showing random fluctuation in wavefront deformation. 75

4.1 Schematic of FEA model 78

4.2 Schematic of Fresnel reflection at entrance and exit faces in $(x, 0, z)$ plane. . . . 79
4.3 COMSOL model of test optic in XY plane showing higher density mesh in the region adjacent to the z axis. This meshing extends along the z axis of the model. . . . 81
4.4 Typical temperature increase, in mK, relative to ambient predicted by the Finite Element Analysis model of 24 cm long FS rod with $\alpha = 30$ ppm/cm and $P_0 = 6.5$ W. . . . 82
4.5 False colour plot at front face of test optic showing temperature rise above ambient [K] for a 10 mm thick BK7 FEA model. . . . 82
4.6 False colour plot of (a) front face of test optic showing temperature rise above ambient [K] and (b) Wave Front Deformation for 5.2 W incident on a 10 mm thick BK7 FEA model. . . . 83
4.7 The residuals from the FEA predicted (orange) and measured WFD data (blue) provide and RMS value of less than 0.05 nm indicating the validity of the measurement process. . . . 84
4.8 Predicted WFD from FEA for the FS 3002 rod and different value absorption coefficients, including piston due to the increase in temperature above ambient. . . . 85
4.9 Wave front deformation for the FS 3002 rod with maximum WFD values matched. . . . 86
4.10 Predicted change in WFD near $\theta_i = 2.3°$. . . . 87
4.11 Change due to heating beam size 88
4.12 Predicted maximum value of WFD as a function of length of the FS rod. . . . 88

5.1 Single Hartmann image showing wavefront deformation from 6.45 W where $N_{avg} = 100$. . . . 92
5.2 Histogram of variation in RMS Gradient normalised by the power in the heating beam. . . . 92
5.3 RMS gradient normailised by incident power as a function of temperature. . . . 93
5.4 Single wavefront map (a) where $N_{avg} = 100$ for both reference and live images showing aberation in wavefront and averaged wavefront map (b) created from five gradient maps of separate Hartmann images each $N_{avg} = 100$. . . . 94
5.5 Numerical wavefront and location of centroids used to determine wavefront deformation showing reduced number of spots in region if interest for y versus X profile. . . . 95
5.6 RMS difference as a function of absorption coefficient used to optimise calculation of absorption coefficient (α). . . . 96
5.7 Wavefront slice in horizontal profile, x, (blue) matched to predicted FEA profile (orange) and residual (dashed). . . . 96
5.8 Wavefront slice in vertical profile, y, (blue) matched to predicted FEA profile (orange) and residual (dashed). . . . 97

5.9 Heating beam focused to a spot (left) and in the near field (right) showing structure in the beam 98
5.10 FWHM of heating beam profile along the test optic. Astigmatism leads to a mismatch in heating profiles. 98

6.1 Absorption in FS. The blue line indicates the measurements made by Heraeus [1] with shaded region indicating the uncertainty in the measurement (SH [2], GEO600 [3], PCI [4]). 102

A.1 linear approximation of Lambert Beer Law where $\alpha = 80$ ppm/cm. . 105

B.1 107

List of Tables

1.1 Main parameters for Advanced LIGO 7
1.2 Baseline parameters for present (aLIGO) and Voyager upgrade configurations 18

3.1 Specifications of Dalsa 1M60 Charged Coupled Device (CCD) camera 51
3.2 CCD Noise from each source expressed in electrons(el). 52
3.3 Properties for Thorlabs SLED 63

4.1 Parameters used for modelling of FS and BK7 80

5.1 Power and absorption comparison for current aLIGO detector (1064 nm science beam) and proposed next generation Gravitational-Wave detectors operating at 2 µm assuming a 6 cm thick beamsplitter. . . 99

Acronyms

AO Adaptive Optics

α absorption coefficient

AOI Angle Of Incidence

ALS Arm Length Stabilization

ADC Anologue to Digital Converter

BS Beam Splitter

BBH Binary Black Hole

BNS Binary Neutron Star

CCD Charged Coupled Device

CP Compensation Plate

DN Digital Number

ERM End Reaction Mass

ETM End Test Mass

FP Fabry-Pérot

FEA Finite Element Analysis

FEM Finite Element Model

FTIR Fourier-Transform Infra-Red spectroscopy

FS Fused Silica

GW Gravitational-Wave

HP Hartmann Plate

HWS Hartmann Wavefront Sensor

HR High-Reflectivity

IR InfraRed

IFO Interferometer

IMC Input Mode Cleaner

ITM Input Test Mass

LED Light Emitting Diode

LIGO Laser Interferometer Gravitational-wave Observatory

MOS metal-oxide-semiconductor

NIR Near Infra-Red

NSBH Neutron Star Black Hole

OH hydroxyl

OMC Output Mode Cleaner

PDE partial differential equations

PD PhotoDiode

PCI Phototherrmal Common-path Interferometry

PDS Photothermal Deflection Spectroscopy

PRC Power Recycling Cavity

QE Quantum Efficiency

RF Radio Frequency

RH Ring Heater

SRC Signal Recycling Cavity

SH Shack Hartmann

SLD Super Luminescent Diode

TEC Thermo-Electric Cooler

TCS Thermal Compensation System

Vis Visible Light

WF Wave Front

WFD Wave Front Deformation

WCoG weighted center of gravity

Chapter 1

Introduction

1.1 Gravitational-waves

The first direct detection of Gravitational-Waves (GWs) from a pair of coalescing black holes by the Laser Interferometer Gravitational-wave Observatory (LIGO) opened a new window on the universe [5]. Since then numerous other Binary Black Hole (BBH) coalescences have been detected [6] and in 2017 the LIGO-Virgo collaboration detected the merger of two neutron stars [7]. Subsequent identification of transient counterparts across the electromagnetic spectrum in the same location further supports the interpretation of this event as a neutron star merger. This unprecedented joint gravitational and electromagnetic observation provides insight into astrophysics, dense matter, gravitation, and cosmology [8].

First proposed by Henri Poincáre in 1905 [9] and later confirmed via Einstein's general theory of relativity, GWs are 'ripples' in the fabric of space-time caused by some of the most violent and energetic processes in the universe. Einstein's mathematics showed that massive accelerating objects, such as neutron stars or black holes orbiting each other, would disrupt space-time in a way that 'waves' of distorted space would radiate from the source much like the movement of waves away from a stone thrown into a pond. Furthermore, these ripples would travel at the speed of light through the Universe, carrying with them information about their cataclysmic origins, as well as invaluable clues to the nature of gravity itself.

The gravitational-wave spectrum spreads across at least 13 decades from below 10×10^{-9} Hz to greater than 10×10^{3} Hz (Figure 1.1). The terrestrial detection band (above 1 Hz) consists of GW signals from stellar mass objects [10].

Gravitational-wave sources can be classified into three distinct classes based on the signal extraction technique used. The first class consists of catastrophic *burst sources* such as the final coalescence of compact binary systems, or the formation of neutron stars and black holes in core-collapse supernova event. The binary coalescence systems include Binary Neutron Stars (BNSs), BBHs and Neutron Star

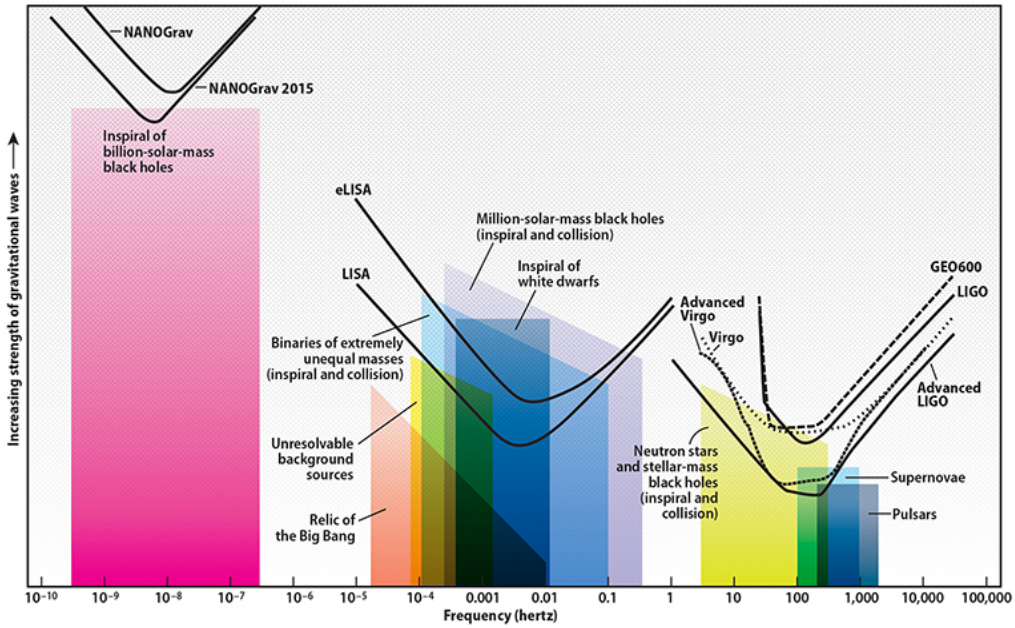

Figure 1.1: The frequency of the GW signals depends on the masses of the source objects. This plot compares those sources against operating and future detectors [11].

Black Hole (NSBH) systems. BBH sources are in-band for a few cycles as the two bodies spiral in towards each other while the signal from BNS sources can last for minutes. The event GW150914 represents an excellent example of a GW signal from a compact burst source (Figure 1.2). The signal enters the GW detector in the low frequency range at 35 Hz and progressively increases in amplitude and frequency to 150 Hz as the two objects reach the merger state [12].

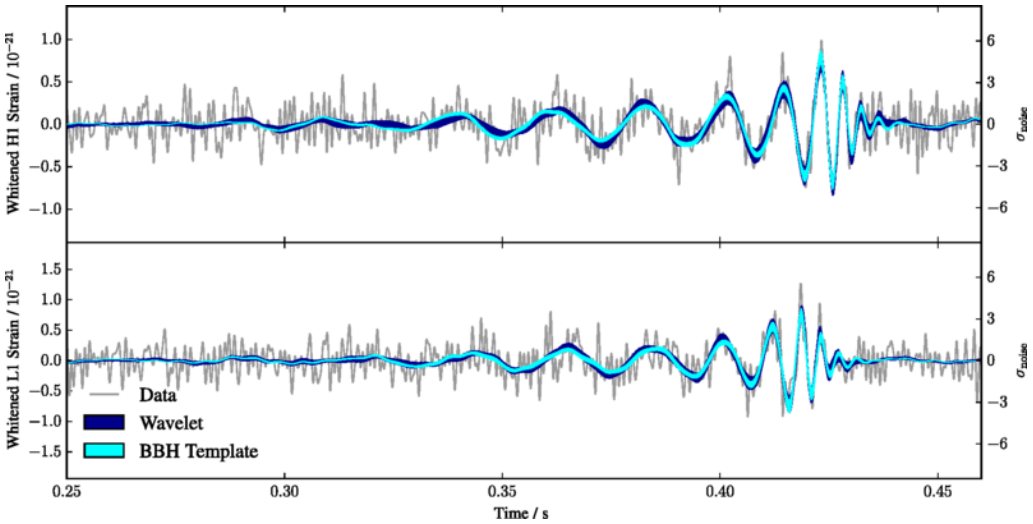

Figure 1.2: Time-domain data, (grey), (sampled at 2048 Hz) and reconstructed waveform, (blue), of GW150914, for the Hanford (top) and Livingston (bottom) detectors [12].

The second class of sources are known as *narrow band sources*. These include single pulsars or accreting neutron stars emitting GWs due to an asymmetry in its orbit, or a binary system far from coalescence. The orbital period of these systems evolve with time as the source loses energy via radiation of GWs. The signals are also periodically Doppler shifted by the binary motion and the Earth's orbital motion. The detection of GW signals from narrow band sources relies on the accurate knowledge of the modulation in the frequency of the source and the relevant doppler effects. Long integration times are required to extract the signal from the noise [13] due to the weak signals emitted.

Due to the large number of GW sources in the universe astrophysicists also predict a third class of sources known as the *stochastic background*. This stochastic background of GWs is due to the multiple effects of continuous sources, burst sources and coalescing binary systems [14] as well as the physical processes occurring at the earliest moments of the universe. Such sources are difficult to detect as they are virtually indistinguishable from detector noise. However, by measuring the cross-correlation of stochastic and instrumental noise at two nearby detectors, the effect of uncorrelated instrumental noise can be minimized and the signal can be extracted [15].

Detection of signals from GW sources will significantly advance our understanding of the physics of extreme phenomena in the universe. Signals from catastrophic burst sources provide an opportunity to explore the origin and evolution of black holes, neutron stars and binary systems. Accurately determining the constraints on the neutron star's equation of state is the key to understanding how they evolve and collapse. Detection of GWs also provides a platform for testing general relativity as the observed signal can be compared against simulated waveforms from numerical relativity.

The gravitational-wave signals from compact binary systems with well-defined parameters can be used to estimate a distance to the source. These systems are known as standard sirens and enhance our capabilities to measure or put constraints on various cosmological parameters. The stochastic background provides an exciting opportunity to probe the earliest epochs of the star formation in the first galaxies [16] and explore physics on energy scales far beyond those accessible in Earth based particle accelerators.

Gravitational-waves experience little absorption or scattering due to the weakness of coupling of gravity to matter even over astronomical distances [17]. In particular gravitational-waves are expected to be unaffected by the opacity of the very early universe. In the early phases, space had not yet become 'transparent' to electromagnetic radiation and as such observations based on the electromagnetic spectrum are limited or unavailable. Therefore gravitational-waves are expected to

have the potential to provide a wealth of information in regards to the very early universe.

Detecting GW emission from supernova events may also help us put constraints on the masses of neutrinos, gravitons and other elementary particles [14].

Gravitational-waves are constantly passing through the planet. The effect of a passing gravitational-wave can be visualised by imagining a perfectly flat region of space time with a spherically symmetrical array of test particles. As a gravitational-wave passes perpendicular to the plane of particles (i.e., into the page), the particles oscillate such that the masses move closer along one axis while simultaneously stretching along the orthogonal axis. Figure 1.3 presents an exaggerated view of the deformation caused by a passing GW signal. This is analogous to the tidal deformation of Earth caused by the gravity gradient due to the moon.

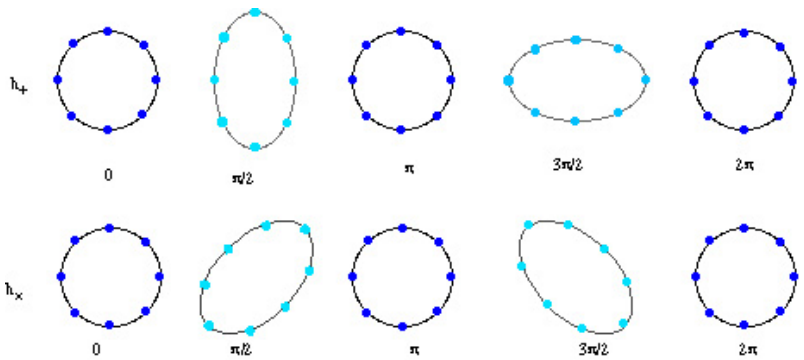

Figure 1.3: GWs stretch and compress the space-time in two directions (polarizations): '+' and 'x'. h_+ and $h_\times$ are time-varying and their amplitude depend on the source that is emitting GWs [14]

Only miniscule effects are produced on Earth due to the vast distances to these GW sources. The direct detection of which rely on an array of interferometric detectors with high sensitivity across a wide frequency band. The following section describes the current design of Earth-based detectors, the noise sources that limit their performance and proposed upgrades to mitigate these issues.

1.2 Detector Design

The LIGO detectors at Hanford, Washington, and Livingston, Louisiana, are currently the most sensitive ground-based gravitational-wave detectors in the world.

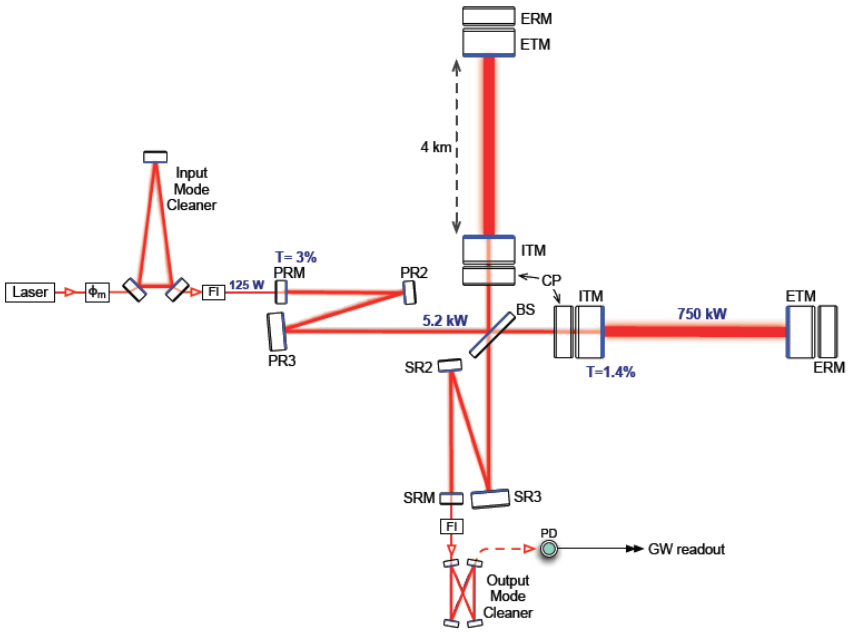

Figure 1.4: Advanced LIGO optical configuration Fabry-Pérot cavity arms and Power Recycling Cavity and Signal Recycling Cavity. [18].

Each site consists of a single Advanced LIGO (aLIGO) detector, that is a modified Michelson Interferometer (IFO) with Fabry-Pérot (FP) cavities in each arm (Figure 1.4) that uses the wave nature of light to detect gravitational-wave signals. The range and strain sensitivity of these detectors during the second observational run are shown in Figure 1.5.

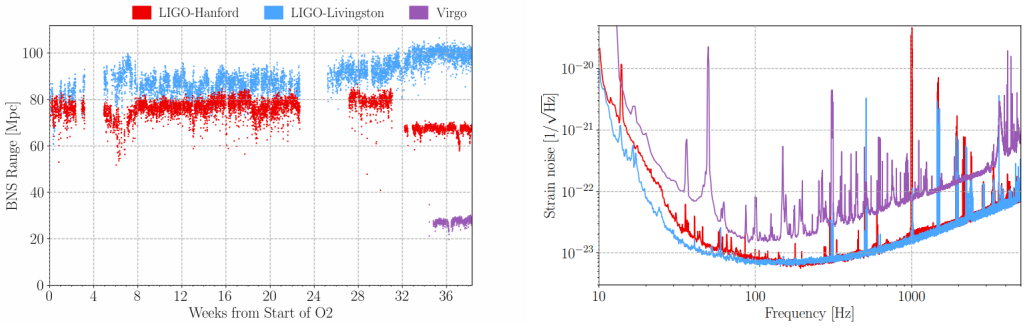

Figure 1.5: Left: BNS range during the second observation run. The Montana earthquake's impact on the Hanford instrument sensitivity can be seen at week 31. Right: Amplitude spectral density of the total strain noise of the Virgo, Hanford and Livingston detectors [6].

The basic operating principle relies on a Michelson IFO in which a 50/50 beam splitter divides the input laser equally between two 4 km arms ending in high reflective mirrors, known as the End Test Mass (ETM). The length of the arms is maintained such that the optical fields in the two orthogonal arms are matched and

destructively interfere when recombined at the beam splitter and read out at a photodetector. Light is stored in the arms by transmitting through highly reflective Input Test Mass (ITM) to create a FP resonator amplifying the effect of passing gravitational-waves. A passing gravitational-wave alters the length of the arms such that the two orthogonal fields effectively travel different distances causing a phase mismatch. This results in a non-zero output at the photodetector which is converted into a gravitational-wave signal. The main parameters for the aLIGO detectors are detaild in Table 1.1.

Increasing laser power improves the IFO's sensitivity. The more photons that merge at the beam splitter, the sharper the resulting interference pattern becomes, making it 'easier' to recognize a gravitational-wave signature.

The input laser is amplified via a number of amplification stages before passing through an Input Mode Cleaner to further stabilize laser beam in position and mode content, and to provide a high-quality laser frequency reference.

To further increase laser power in the IFO, partially reflective 'power recycling' mirrors are placed between the laser source and the beam splitter. Differential phase matching at teh beam-splitter reflects nearly all the reflected laser light from the arms to follow a path back to the recycling mirrors rather than to the photodetector [19]. Laser light coming from the ends of the arms is thereby reflected back into the IFO (hence 'recycling') from the Power Recycling Cavity (PRC).

A Signal Recycling Cavity (SRC) is used between the photodiode and the beam splitter to allow further tuning of the signal response bandwidth of the interferometer. This broadens the bandwidth of the arm cavities allowing for a wider range of GW frequencies to be detected.

The last optical interface in aLIGO is the Output Mode Cleaner. It is designed and configured to transmit the signal field of the carrier light as much as possible, while removing any other field like carrier higher-order modes and RF modulation sidebands.

1.3 Detector Noise Sources

Advanced LIGO detectors are limited by several noise sources. A typical noise curve from the LIGO detectors is shown in Figures 1.6 and 1.7. The typical strain from

Table 1.1: Main parameters for Advanced LIGO [20]

Parameter	Value
Arm cavity length	3994.5m
Arm cavity finesse	450
Laser type and wavelength	Nd:YAG, $\lambda = 1064$ nm
Input power at PRM	up to 125 W
Beam polarization	linear, horizontal
Test mass material	Fused Silica
Test mass size and mass	34cm diam. x 20cm, 40 kg
Beam radius ($1/e^2$), ITM / ETM	5.3 cm / 6.2 cm
Radius of curvature, ITM / ETM	1934 m / 2245 m
Input mode cleaner length and finesse	32.9 m (round trip), 500
Recycling cavity lengths, PRC / SRC	57.6 m / 56.0 m

GWs reaching Earth is very small. The LIGO detectors are currently capable of detecting strains as small as 10^{-23} in the frequency band between 30 and 1200 Hz.

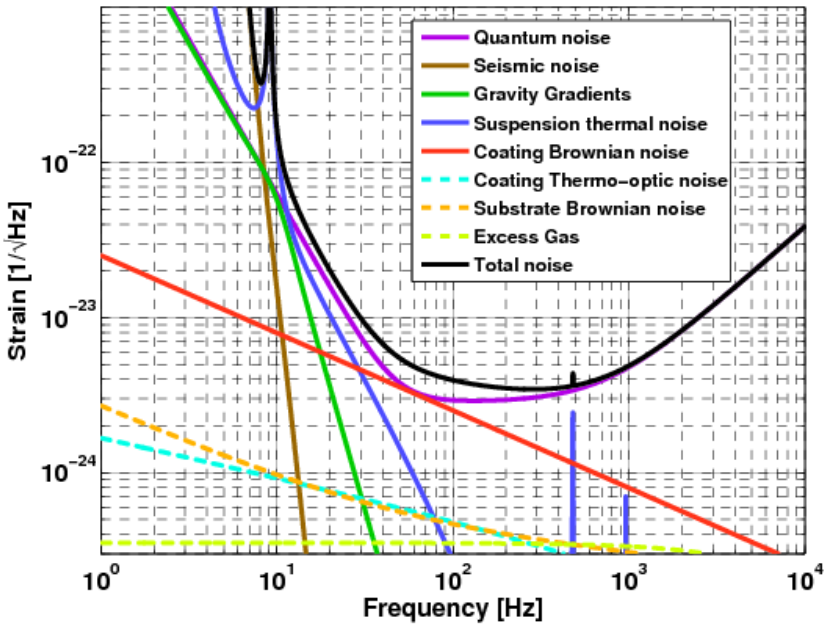

Figure 1.6: The modelled strain sensitivity for the Hanford LIGO detector during the second observation run. The noise spectrum is a sum of noise contributions from the quantum, thermal, seismic and Newtonian noise sources as well as 'Degree-Of-Freedom' noise sources. Countless other noise sources, such as laser frequency, beam jitter, sensor and actuation noise sources, which do not contribute significantly to the overall spectrum have been omitted for clarity. The strong peaks in the spectrum are due to the violin modes of the suspension system.

At frequencies lower than 100 Hz, the detectors are affected by thermal, seismic and Newtonian noise sources. The quantum nature of light also puts a fundamental limit on the maximum sensitivity. Other degrees of freedom such as alignment and control systems contribute to the overall noise budget of the IFO. Violin modes from the suspension system couple into the IFO and appear as discrete peaks in the strain sensitivity curve of the detector.

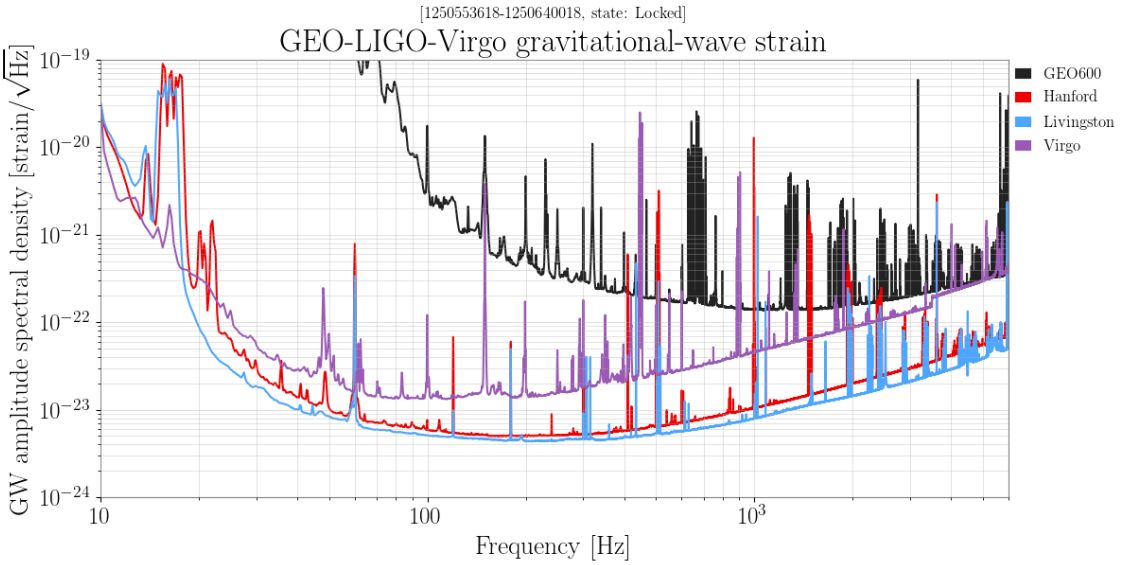

Figure 1.7: Noise curve for the four detectors involved in the third observation run. Several effects cause the sharp lines visible in the spectra: mechanical resonances in the mirror suspensions, resonances of the internal mirror modes, power line harmonics and so on. As the broadband floor of the sensitivity is most relevant for gravitational-wave detection, these lines are typically not too harmful.

1.3.1 Seismic and Newtonian Noise

Seismic noise refers to the displacement of the mirrors caused by ground vibrations, earthquakes, wind, and human activities such as vehicle traffic coupling into the detector. Newtonian or gravity gradient noise is due to fluctuations of the local gravitational field as a result of seismic and atmospheric displacements. This limits the sensitivity of ground based gravitational-wave detectors at frequencies below 10 Hz [21].

To mitigate the effect of ground vibrations, each test mass is suspended from a multi-stage suspension system (Figure 1.8). The entire pendulum system is mounted from an actively controlled seismic isolation platform which utilizes an array of motion sensors, hydraulic actuators and servo controls to further reduce the effect of large displacements caused by tidal motions and micro seismic activity [22].

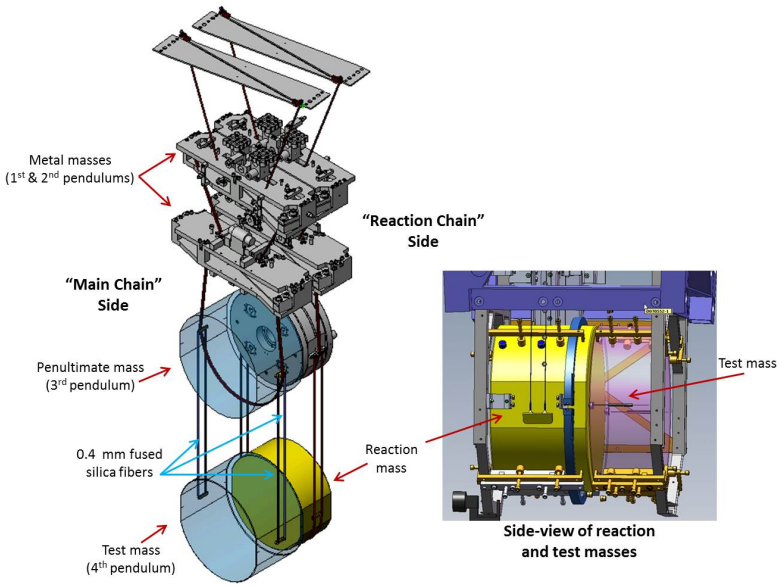

Figure 1.8: Schematic of a Dual-chain, quadrupole-pendulum system used in the aLIGO detectors. The lowest masses on the main chain are the test masses suspended using Fused Silica fibres. The reaction chain consists of electromagnetic actuators which actively correct for seismic and thermal effects. The lowest mass is a compensation plate in case of the ITMs and an end reaction mass for ETMs [23].

1.3.2 Thermal Noise

One of the fundamental noise sources in the detectors is thermal noise. LIGO classifies thermal noise into three distinct classes: suspension thermal noise, test mass substrate thermal noise and coating thermal noise.

Thermal noise in the test mass suspension is primarily due to mechanical loss in the Fused Silica fibres used in the final suspension stage. Thermally induced vibrations of the suspending wires result in a fluctuation of the masses position along the laser beam [24]. The four glass fibres have a circular, but variable diameter cross-section: they are thin in the main (middle) section of the fibre, and about twice as thick near the ends (Figure 1.9). This geometry minimizes thermal noise, while keeping the fibre violin mode frequency high (510 Hz fundamental) and the vertical stretching mode frequency low (9Hz).

Coating Brownian noise is the dominant source of the various thermal noise terms. It arises from mechanical dissipation in the coatings, and is minimized by making the beam size on the test masses as large as practical so that it averages over more of the mirror surface. Coating thermo-optic noise arises from thermal dissi-

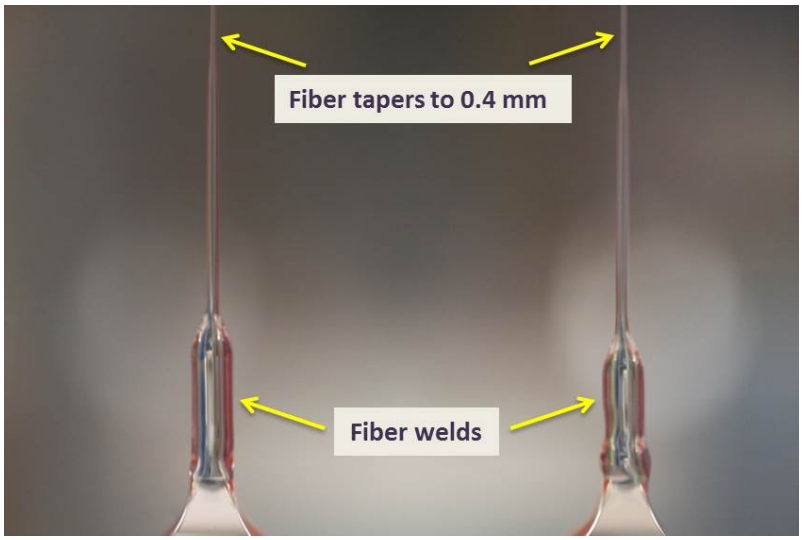

Figure 1.9: Fused Silica (FS) suspension wires bonded to 'ears' on the test mass. [25].

pation in the coatings, producing noise via the thermoelastic and thermo-refractive coefficients of the coating materials. To reduce the effect of thermal noise in the detector, the 40 kg test masses are made of low-mechanical-loss materials, which include a FS substrate with low-loss dielectric coatings [14].

1.3.3 Quantum Noise

The fundamental noise floor in the IFO is due to quantum noise. Quantum noise depends circulating power in the arms and the configuration of the signal recycling cavity [18]. Quantum noise encompasses the effects of statistical fluctuations in the detected photon arrival rate (shot noise) and radiation pressure due to photon number fluctuations (Figure 1.10).

Shot noise is caused by random fluctuations in the number of photons hitting the photodiodes, this dominates sensitivity at high frequencies and introduces amplitude noise in the gravitational-wave signal. At low frequencies radiation pressure noise becomes the limiting factor. Radiation pressure is due to the fact that light has momentum and imparts this on the test masses upon reflection. This results in a displacement of the test masses from their nominal positions due to the fluctuations in the pressure exerted by the incident photons.

Increasing stored laser power in the IFO arms decreases shot noise. This is due to the fact that the amplitude of the optical signal that results from the GW increases

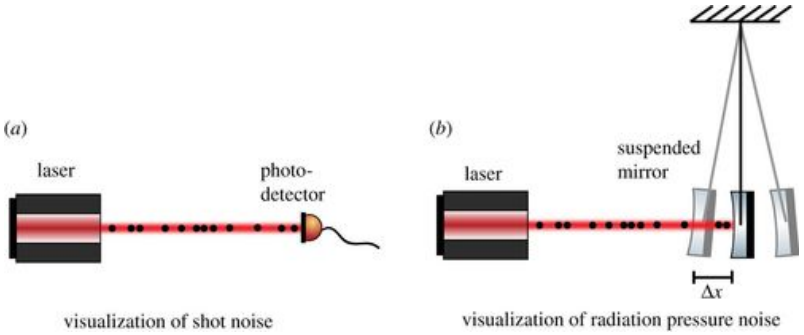

Figure 1.10: The photons of a coherent state arriving at a photodetector cause shot noise (i.e. detection noise). (b) The same stream of photons impinging on a suspended mirror causes the mirror position to fluctuate while the restoring force causes the mirror to fall back into its position of equilibrium (i.e. back-action noise) [26].

linearly with laser power whereas the shot noise decreases with the square of the laser power [14]. However, increasing laser power introduces thermal distortions in the test masses via coating and substrate absorption and parametric instabilities, all of which can cause instabilities in the IFO when run for extended periods. Parametric instabilities are a result of the interaction between higher-order modes in the optical cavity and acoustic modes of the mirrors which can lead to exponential growth of acoustic vibrations in the system.

1.4 Squeezed Light

The quantum noise in the IFO can be reduced by using squeesed light.

Light is an electromagnetic wave with amplitude, A, and phase, Φ. The precision that which these two quantities can be measured is limited by their fundamental uncertainty. This is due to the quantum nature of light which is governed by the Heisenberg uncertainty principle.

$$\Delta A \Delta \Phi \geq \frac{\hbar}{2}$$

where ΔA is the uncertainty in amplitude and $\Delta\Phi$ is the uncertainty in phase respectively.

Shot noise and radiation pressure noise are more rigorously described by the interaction of quantum vacuum fluctuations, which enter the readout port of the IFO with the circulating laser light. Variance in the vacuum's phase quadrature is associated with shot noise, which is significant at high frequencies; while variance in the vacuum's amplitude quadrature is related to radiation pressure noise and is most important at low frequencies (See Figure 1.12).

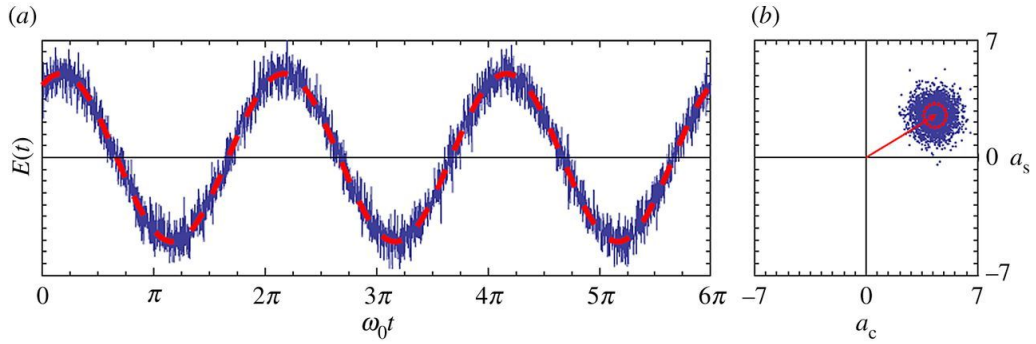

Figure 1.11: Time series (a) and phase space (phasor) representation of a coherent state (b), the state of light emitted by a well-stabilized laser showing variation (blue) from ideal (red). [27].

While the impact of quantum noise can be changed by, for example, altering the input laser power, changing the mass of the IFO optics or modifying the parameters of the signal recycling cavity, it may also be targeted directly by operating on incident vacuum fluctuations themselves.

The variances in orthogonal quadratures of a vacuum state are governed by a Heisenberg-like-inequality. Exploiting the techniques of nonlinear optics, one can reduce the variance in one quadrature, mitigating the corresponding noise term at the expense of increased variance in the orthogonal quadrature and heightened noise of a different type (Figure 1.12). The result is called a 'squeezed vacuum state', with the act itself known as squeezing. By replacing the naturally occurring vacuum fluctuations entering an IFO with squeezed vacuum, quantum noise in one quadrature can be reduced, see Figure 1.13).

1.5 Thermal Compensation System

In the final aLIGO design there is up to 750 kW incident on the coatings on the test masses and 5 kW passing through the ITM substrates. These coatings are made from low index silica and high index titania doped tantala to reduce coating thickness and have a nominal absorption of 0.5 ppm [29]. As a result, there will be 375 mW of laser power with a Gaussian spatial distribution absorbed in the coatings

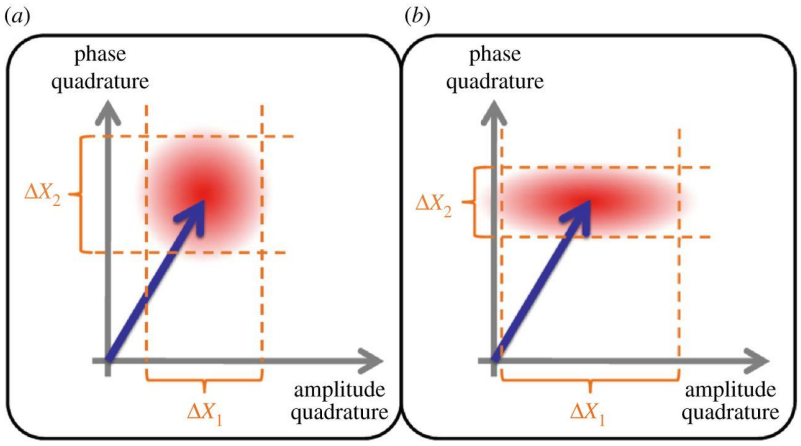

Figure 1.12: The above image shows the phase space representation of a coherent state (a) and a squeezed state (b) with reduced noise in the phase quadrature at the cost of increased noise in the amplitude quadrature, a so-called phase-quadrature-squeezed state. It still fulfils the Heisenberg Uncertainty Principle as the area of the distribution in phase space remains larger than (or equal to) 1. [27].

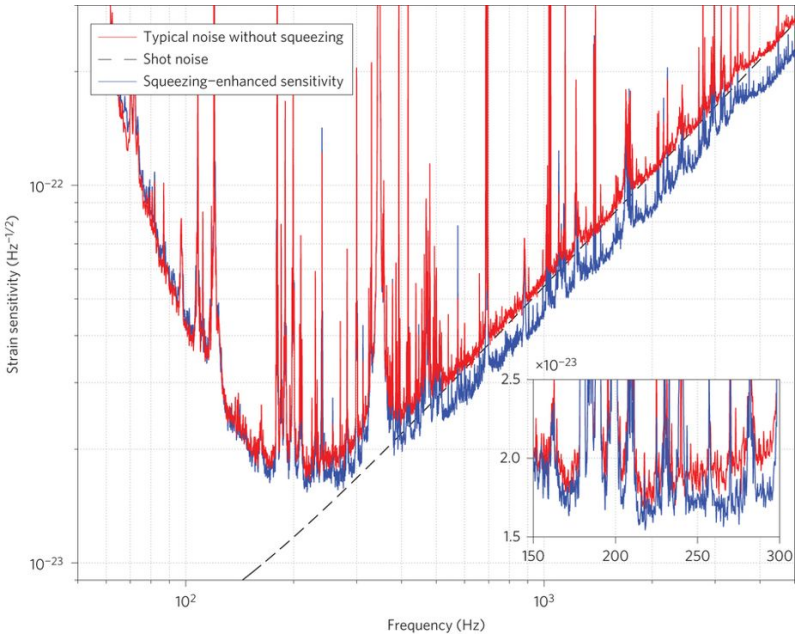

Figure 1.13: Noise reduction due to squeezing. The improvement is up to 2.15 dB in the shot-noise-limited frequency band. The inset magnifies the frequency region between 150 and 300 Hz, showing that the squeezing enhancement persists down to 150 Hz [28].

of the test masses. Absorption within the substrates results in a radial temperature gradient within the optics [30, 31]. The resulting temperature gradients will result in thermo-refractive wavefront distortion within the substrate of the optics (due to the dependence of refractive index on temperature) and thermo-elastic surface deformation. This is illustrated in Figure 1.14.

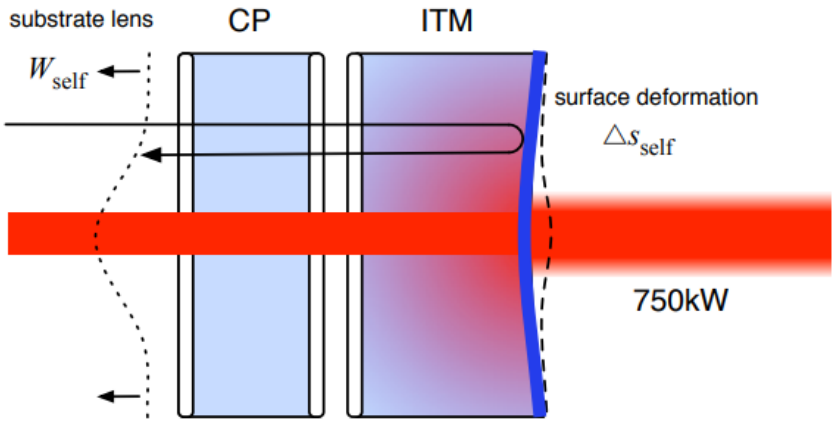

Figure 1.14: An illustration of the thermo-refractive substrate lens, W_{self}, and the thermo-elastic surface deformation, Δs_{self}, from self heating [29].

The wavefront distortion degrades the operation of the IFO and reduces its sensitivity. Thus aLIGO currently implements a Thermal Compensation System (TCS) to actively compensate for these effects [29]. The TCS includes Hartmann Wavefront Sensors (HWSs) that measure the wavefront distortion [29], and Adaptive Optics (AO) including ring heaters to correct for surface and substrate distortions by direct radiation onto the test mass and CO_2 lasers projected onto Compensation Plates suspended directly behind the ITM to actively correct for these distortions (see Figure 1.15). Fluctuations in the output CO_2 laser at high power can introduce additional noise to the detector if not actively stabilised.

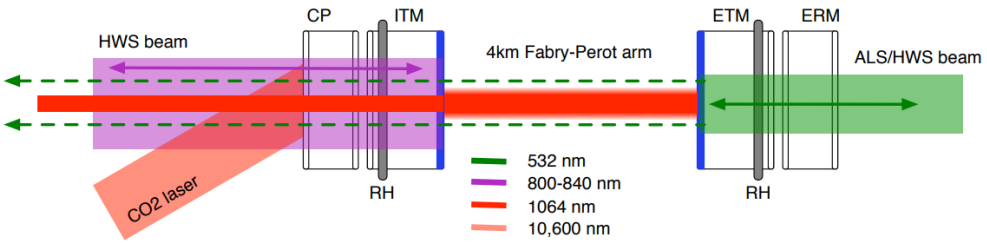

Figure 1.15: Absorption of the main interferometer beam (red) in the test masses induces thermal lenses. HWS probe beams, (purple) and (green), measure the thermal lens in the substrates of the ITM + Compensation Plate (CP) [29].

1.5.1 HWS measurement system

A HWS samples the wavefront using an array of apertures in an otherwise opaque plate, referred to as a Hartmann Plate (HP). The beam of light created by each aperture, known as 'Hartmann Rays', propagates perpendicularly to the local wavefront, creating an array of spots on the Charged Coupled Device (CCD) (Figure 1.16). Changes in the incident wavefront result in a transverse displacement of the spots, proportional to the change in local slopes of the wavefront and the "lever arm" distance between the HP and the active surface of the sensor. This gradient field is integrated to produce the wavefront change [32].

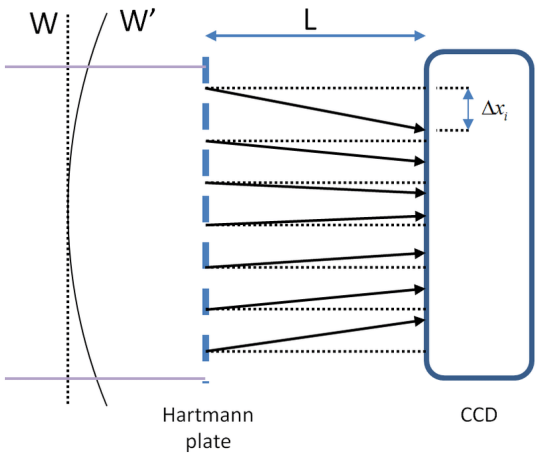

Figure 1.16: Working principle of the Hartmann Wavefront Sensor: an aberrated wavefront W' is incident on a Hartmann plate. The resulting rays propagate a distance L, normal to the wavefront, and are incident on a CCD. The new spot position, x_i', is measured and compared to a reference spot positions, x_i, determined using a non-aberrated wavefront W. The wavefront gradient in the i^{th} position is given by $\delta\Delta W/\delta x = \Delta x_i/L$ [33].

The HWS currently installed in aLIGO are used to tune the operation of the detector, and monitor changes in the thermally induced wavefront distortion for each of the FP mirrors. They measure on-axis distortion using probe beams that have wavelengths different to that of the IFO beam and without introducing additional optics within the IFO beam [29].

The absorption-induced distortion and actuation for the mirrors at the end of the FP arms is measured using 532 nm Light Emitting Diode (LED) sources that pass through the substrate and retro-reflect from the High-Reflectivity (HR) surfaces. A numerical model is used to estimate the thermo-elastic distortion of the HR surfaces. The HWS for the FP input-couplers use probe beams from Super Luminescent Diode (SLD) sources to minimize stray interference fringes that would degrade the sensitivity of the HWS. The wavelength is chosen so that the probe beams can

be transmitted through or reflected from existing IFO optics. An example of the evolution of the uncompensated quadratic component of the wavefront distortion in a FP input coupler as power is stored in the FP cavity is plotted in Figure 1.17. AO are used to mode-match the beams from the two arms at the beam-splitter. The HWS can also reveal non-quadratic distortion, as shown in Figure 1.18. This distortion could not be compensated and is believed responsible for the reduced sensitivity of LIGO Hanford during Observing Run 2 (O2).

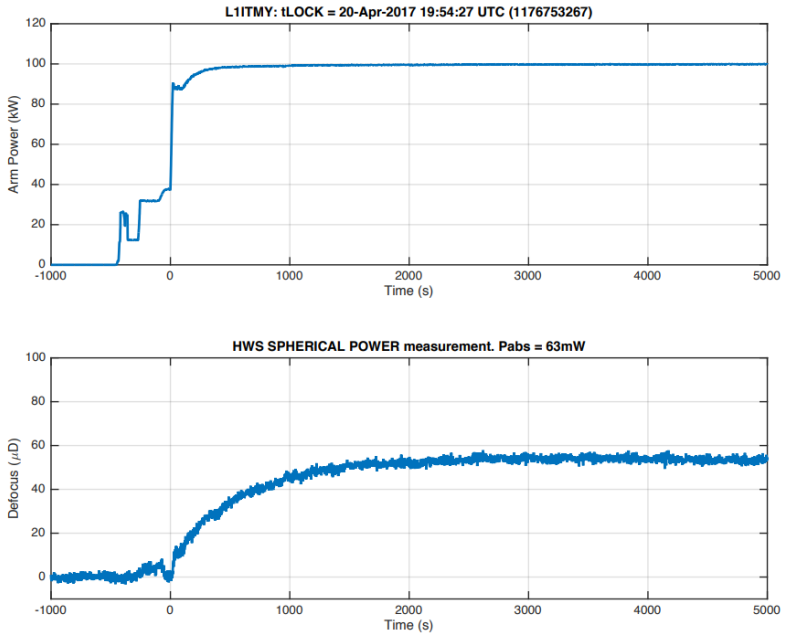

Figure 1.17: Evolution of the uncompensated thermal lens within a FP input coupler [34]).

1.6 Voyager Upgrade

LIGO Voyager is a proposed upgrade to the current aLIGO detector operating in the existing LIGO facilities. It would include silicon mirrors cooled to 120 K and a high power laser of wavelength 1.5 µm-2 µm (see Table 1.2). A further factor of 3 increase in BNS range (to 1100 Mpc) is envisaged with a low frequency cut-off down to 10 Hz. A suggested noise budget for this upgrade is shown in Figure 1.19.

LIGO Voyager will improve sensitivity across the entire LIGO frequency band, 10 Hz to 10 kHz. However, substantial research is required to make the system design for Voyager a success because the subsystem improvements are tightly coupled: decisions made about one subsystem likely place requirements on other subsystems. For example, high frequency improvements achieved using increased laser power

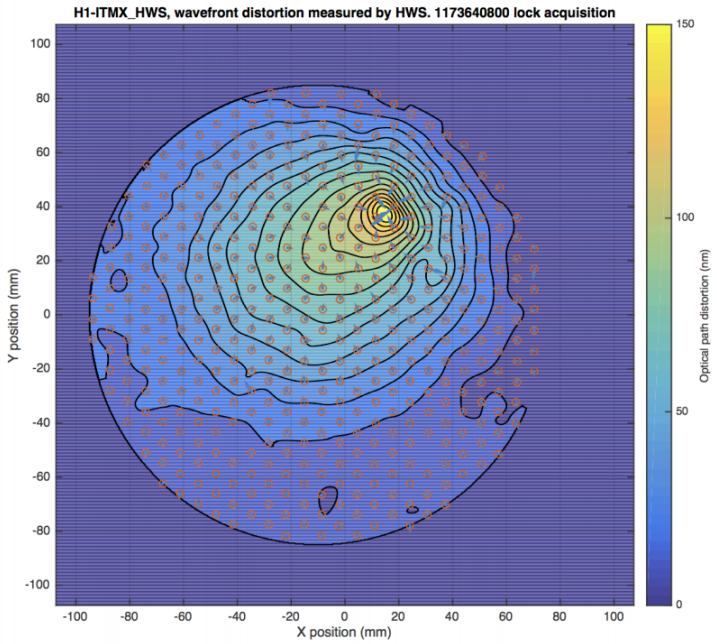

Figure 1.18: Non-quadratic wavefront distortion due to a point absorber on the surface of an FP input coupler. The red circles represent the apparent location of the HP apertures [34].

and low frequency improvements from reduced thermal noise drive the need for low temperature operation. Low temperature will both reduce thermal distortions (optimize thermal conductivity) and lower the thermal noise of the mirrors. It also necessitates a change of the mirror substrate material to silicon and may also drive a change to the suspension material. The use of silicon optics drives a change to laser wavelengths greater than 1300 nm. The need to reduce scatter loss to maximize the effectiveness of squeezing across the spectrum may also be a driver for longer wavelength operation. In addition to new high-power lasers, the change in wavelength also drives a need for new optical components such as detectors, modulators, and Faraday isolators, all of which must meet LIGO requirements. The development of new optical coatings for low temperature with ultra-low optical and mechanical loss is also required. To achieve the broadband, low-temperature performance shown in Figure 1.19 R&D is needed in many areas.

The change of the test mass optics from silica to silicon is central to the Voyager upgrade. Silicon has high thermal conductivity at cryogenic temperatures leading to a reduction in temperature gradients that are generated by laser beam absorption. The thermal expansion coefficient of silicon has a zero crossing at 123 K. Near this temperature, thermo-elastic distortions of the mirror surface are drastically reduced, as is thermo-elastic noise due to temperature fluctuations.

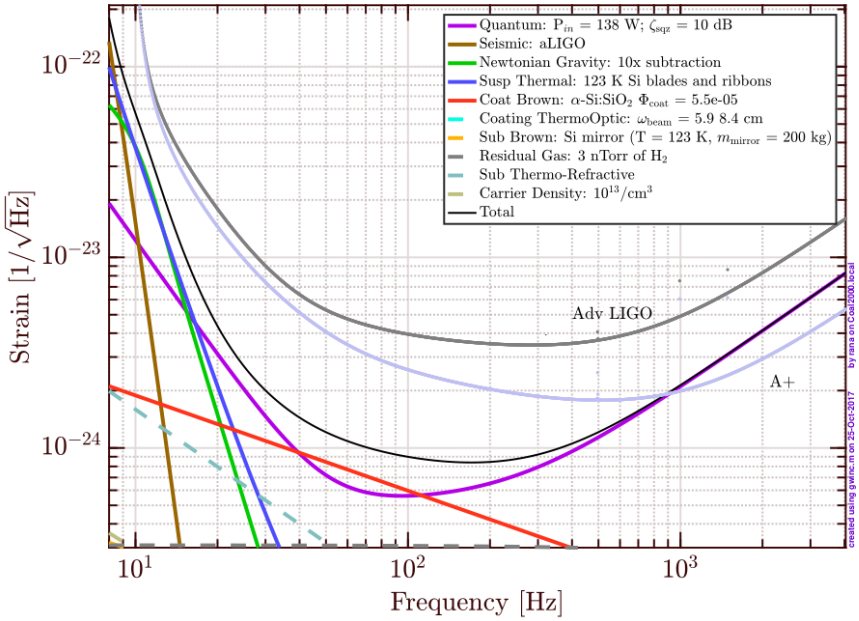

Figure 1.19: Proposed strain sensitivity of LIGO Voyager with 200 kg silicon test masses at 123 K, and 3 MW of arm cavity power [35].

Table 1.2: Baseline parameters for present (aLIGO) and Voyager upgrade configurations [35]

Parameter	aLIGO	Voyager
Mirror substrate	FS	silicon
Arm cavity length	4000 m	4000 m
Arm cavity finesse	450	450
Laser type and wavelength	Nd:YAG, $\lambda = 1064$ nm	$\lambda = 2\mu$m
Input power at PRM	125 W	140 W
Arm power [kW]	750	3000
Test mass size [cm]	34 diam. x 20	45 diam. x 55
Test mass mass [kg]	40	204
Beam radius ($1/e^2$), ITM / ETM	5.3 cm / 6.2 cm	5.9 cm / 8.4 cm
Radius of curvature, ITM / ETM	1934 m / 2245 m	1801 m / 2596 m

Silicon can be produced in large sizes. Boules of up to 45 cm are within the capabilities of current manufacturing processes leading to mirrors with masses in the region of 200 kg with high purity levels consistent with low absorption in the substrates in the $1550 - 2200$ nm wavelength range. A shift to large mass silicon test masses will reduce thermal and seismic noise when compared with current detectors as well as reducing radiation pressure noise. Nevertheless, much of the technology for the Voyager upgrade remains to be demonstrated, including precision measurements of optical loss in the Si substrates and coatings, high power stable lasers, squeezed

light sources, high quantum efficiency photodiodes, and low loss auxiliary optics, for example.

Implications of absorption in the beamsplitter and auxiliary optics must be considered. The absorption coefficient due to multi-phonon absorption in FS at 2000 nm is estimated to be approximately 25 ppm/cm [35]. Multiphonon absorption is a process where multiple phonons are created in conjunction with the absorption of a single photon. This governs the long-wavelength limit of transparency range, often called the InfraRed (IR) absorption edge and is the theoretical lower limit of absorption. This yields a lower limit of approximately 160 mW of absorbed power in a 6 cm thick beam splitter. FS is used in a wide range of optical applications due to its high transmission and low thermo-elastic properties but it is not well characterized at 2 µm. With the proposed power level of 27 kW of circulating power in the PRC, accurate measurement of the absorption in proposed beam-splitter materials is critical before moving forward.

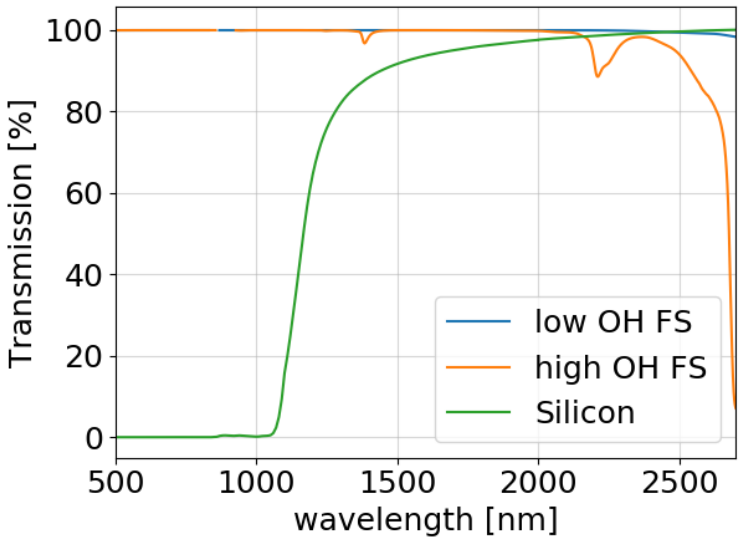

Figure 1.20: Typical transmission including Fresnel reflection losses $(1\text{-}R)^2$ for low OH (3002) and high OH (311/312) Fused Silica [36] and Silicon [1]

Low hydroxyl (OH) FS is currently used in aLIGO for the ITMs, Beam Splitter (BS) and CPs. This is manufactured by Heraeus Quartz under the name Suprasil 3002. Typical transmission compared with Si is shown in Figure 1.20 . Hereaus states that 3002 FS is better than class zero inclusions [36]. Inclusions are bubbles or particles in the material > 0.01 mm and are a source of scatter and point absorption in the optic (see Section 2.1.4). A material is considered 'Zero Class' when there is less than 1.0 inclusions per 100 m^3. Inclusions are defined to total less than $0.01mm^2/100cm^3$ of glass within the clear aperture. Extinction coefficient as measured by Heraeus is shown on Figure 1.21.

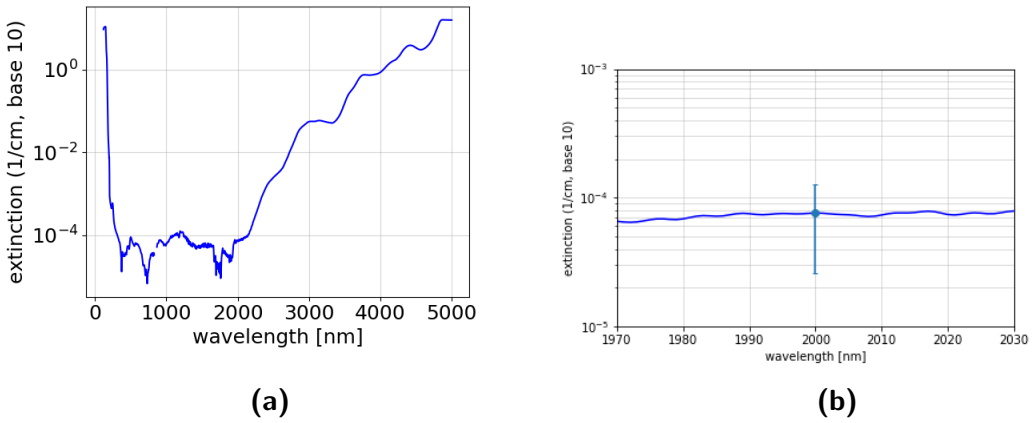

(a) **(b)**

Figure 1.21: Absorption coefficient of Suprasil 3002 as determined by Heraeus Quartz [36] (left) Detail at 2 µm showing error bars of 5×10^{-5}/cm (right).

Current methods for determining the absorption in fused silica use the cut-back method involving the comparison of optical power transmitted through differing lengths of optical fiber as well as standard spectroscopic techniques. Heraeus' current published data [36] states the measured absorption coefficient at 2 µm as 7.592×10^{-5} cm^{-1} see Figure 1.21. This measurement was conducted using standard photo spectrometer techniques and includes bulk scatter and as such results in 50% uncertainty in the calculated value [1].

Other methods rely on photothermal effects to determine the absorption and will be discussed in more detail in Chapter 2. The main drawbacks of current techniques include accuracy and resolution in extremely weakly absorbing materials.

1.7 Project aims

The aim of this project is to develop and demonstrate a sensitive and accurate technique for measuring optical absorption coefficient in weakly absorbing materials, particularly Heraeus 3002 fused silica. The approach is to use the photothermal effect and exploit the demonstrated high precision and accuracy of a differential Hartmann Wavefront Sensor [32] to measure the wavefront distortion caused by the temperature gradient resulting from the absorption. The absorption coefficient will be determined by comparing the prediction of a finite-element numerical model with the measured distortion.

1.8 Thesis structure

Chapter 2 describes optical loss in transparent media and reviews techniques used to measure attenuation in a variety of optical materials. Chapter 3 presents the absorption measurement system, detailing experimental layout, reproducibility and uncertainty in the system. Chapter 4 describes the finite-element model, investigates the sensitivity of the model to measurement system parameters and validation of the model using a BK7 window for which the absorption is known. Chapter 5 reports the measurement of the optical absorption coefficient of Heraeus 3002 fused silica at 1994 nm. This thesis concludes with Chapter 6, which includes a discussion of future improvements.

Chapter 2

Optical Loss in Transparent Media

Optical losses in a material occur due to light-matter interactions such as scatter and absorption as shown in Figure 2.1 and results in a power loss upon transmission through a transparent material.

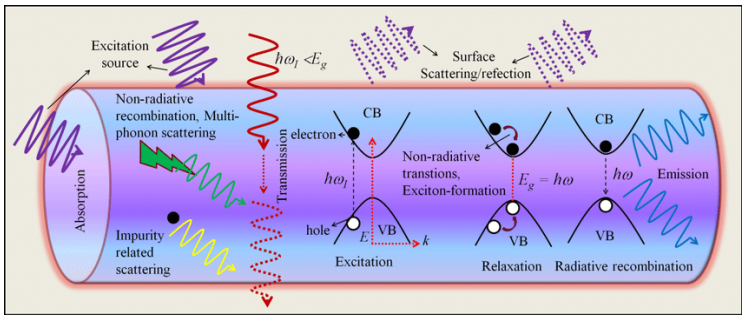

Figure 2.1: Schematic sketch depicting the multitude processes involved in light–matter interaction [37].

A laser beam incident on an uncoated transparent optic will be attenuated due to:

- Fresnel reflection at the entry and exit surfaces.
- Elastic scattering due to surface roughness, Rayleigh and Mie scattering within the material.
- Brillouin and Raman inelastic scattering.
- Intrinsic absorption of the substrate.
- Extrinsic absorption due to impurities.

Additionally, if a multi-layer dielectric interference coating is applied to the optic to decrease or increase the surface reflectance, then scatter and absorption within the coating must also be considered.

The magnitude of these processes depend on the wavelength of the light and the nature of the material. In Section 2.1, the scattering and absorption mechanisms listed above are reviewed. While many of these processes are important for the development of Gravitational-Wave (GW) detectors, the focus of this thesis is the

measurement of optical absorption in materials to be used for core optics in 3G detectors, the main candidate of which is Fused Silica (FS) due to its excellent mechanical properties at room temperature. Optical absorption losses are almost always less than scattering losses but can lead to thermal distortions which can have more significant effects. Thus, in section 2.2, we review techniques for measuring low-level absorption in candidate materials.

2.1 Loss Mechanisms

2.1.1 Fresnel Reflections

Light incident on an interface between two transparent media with differing refractive indices will be partially transmitted and partially reflected [38].

The reflectance and transmittance at the interface can be calculated using the Fresnel equations (Equations (2.1) and (2.2)), and depend on the refractive indices, angle of incidence and polarisation of the incident beam as shown in Figure 2.2. For small angles of incidence the reflectance of s and p polarisation is approximately equal. For an unpolarised beam the reflectance can be considered as the average of s and p polarisations. The reflectance for s-polarised light is given by:

$$R_S = \left| \frac{n_1 \cos\theta_i - n_2 \sqrt{1 - \left(\frac{n_1}{n_2}\sin\theta_i\right)^2}}{n_1 \cos\theta_i + n_2 \sqrt{1 - \left(\frac{n_1}{n_2}\sin\theta_i\right)^2}} \right|^2 \tag{2.1}$$

while the reflection for p-polarised light is:

$$R_P = \left| \frac{-n_2 \cos\theta_i + n_1 \sqrt{1 - \left(\frac{n_1}{n_2}\sin\theta_i\right)^2}}{n_1 \cos\theta_i + n_1 \sqrt{1 - \left(\frac{n_1}{n_2}\sin\theta_i\right)^2}} \right|^2 \tag{2.2}$$

Where θ_i is the angle of incidence from the normal to the interface and n_1, n_2 are refractive indices of the two mediums.

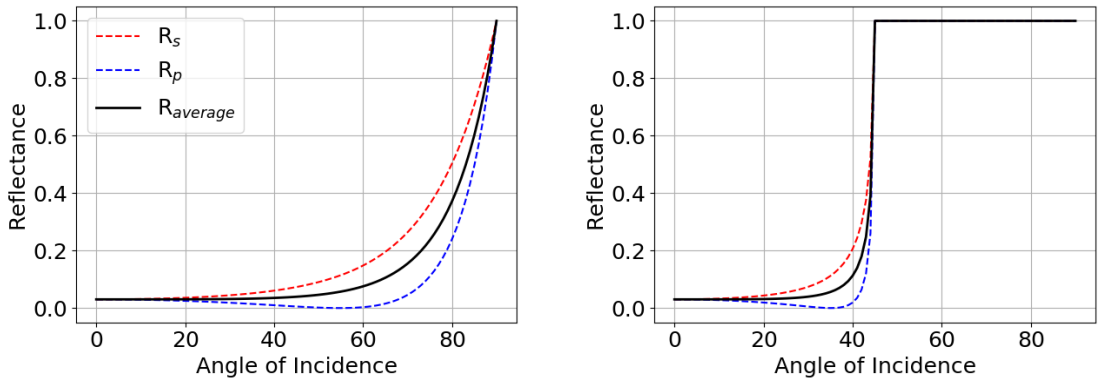

Figure 2.2: Reflectance of an (a) air/FS and (b) FS/air interface for s and p polarizations.

The reflection at the first surface will attenuate the beam passing through the optic while the reflectance at the exit face will travel back through the optic causing additional absorption. Both of these processes need to be considered when calculating the power deposited in the test optic.

2.1.2 Diffraction losses due to surface roughness

An incident beam will be scattered by surface microirregularities, particularly residual scratches and pits or "digs". Thus, all aLIGO optics are super-polished to reduce scatter loss to ≤ 10 ppm and thus minimize the degradation of detector sensitivity due to "stray light". The optics used for this thesis, however, have a conventional 20-10 scratch-dig [39] surface polish for which 0.1 % loss is expected [40]. This loss will have negligible effect on the power of the beam passing through the test optic and as such will not result in significant thermal distortions.

2.1.3 Rayleigh scattering

Rayleigh scattering is the elastic scattering of light from inhomogeneity or small defects in the material. In high quality materials, the scattering is mainly due to variations in the density of the material. The theoretical value of the scattering

is described by the scattering coefficient, α_{sca}, the attenuation coefficient per unit length, in the ppm/cm regime when $\alpha_{sca} \ll 1$ [41].

$$\alpha_{sca} = \frac{8\pi^3}{3\lambda^4} \left(n^4 p\right)^2 kT\beta_T \tag{2.3}$$

Where λ is wavelength, n is the index of refraction, p is the photoelastic constant, k is the Boltzmann constant, T is absolute temperature and β_T is the isothermal compressibility of the material.

Rayleigh scattering is a significant loss process at shorter wavelengths, as shown in Figure 2.4. For wavelengths around 2 µm, the total loss in FS is expected to be 0.6 dB/km which is approximately 1.5 ppm/cm and thus will have negligible effect on the power of the beam passing through the test sample in this measurement.

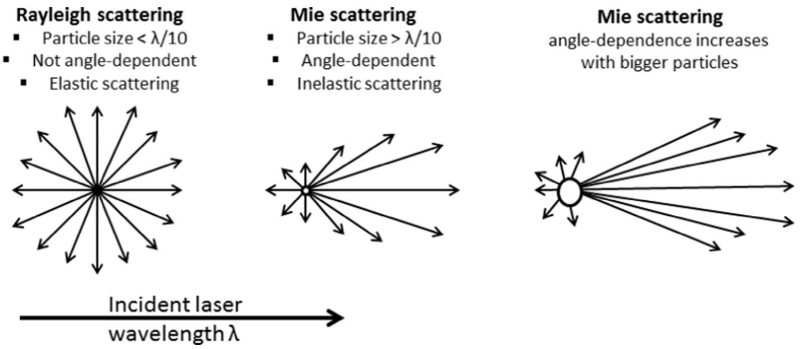

Figure 2.3: Schematic showing the differences between Rayleigh and Mie scattering in relation to particle size [42].

2.1.4 Mie Scattering

Mie elastic scattering in solids is due to inclusions, imperfections and bubbles within the substrate or optical coatings with sizes similar to or larger than the wavelength of light, as indicated in Figure 2.3. As for surface roughness scattering, optics used in aLIGO are required to have extremely low levels of Mie scattering, particularly as the scattering is largely forward directed and thus may have a greater impact on detector sensitivity.

In low hydroxyl (OH) high-homogeneity FS, such as Suprasil 3002, the total scattering cross-section of all bubbles is ≤ 0.015 mm^2 per 100 cm^3 [43]. The attenuation due to Mie scattering is much less than that due to Rayleigh scattering at 2 µm, and thus can be ignored for calculation of the absorption coefficient at 2 µm.

2.1.5 Brillouin Scattering

Spontaneous Brillouin scattering is a Stokes process in which a photon is scattered by a thermally generated sound wave, creating a phonon and thus losing energy. Brillouin scattering, α_{Bril}, contributes a loss as [41]:

$$\alpha_{Bril} = 5 \times 10^{-5} n_0^8 p^2 K(T) \frac{T}{\lambda^4} \; [dB/km] \tag{2.4}$$

As indicated in Figure 2.4, the attenuation due to Brillouin scattering in FS is estimated to be about an order of magnitude less than that for Rayleigh scattering at 2 µm [44], and thus will have negligible effect on the power of the beam passing through the test sample.

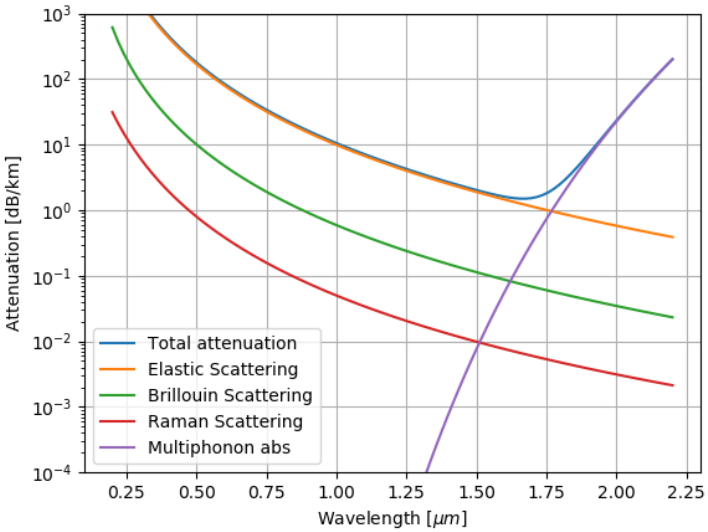

Figure 2.4: Contribution of scattering and absorption processes in 'pure' (no inclusions or impurities) FS [44] showing an increase in multiphonon absorption at wavelengths greater than 1.6µm.

2.1.6 Raman Scattering

Spontaneous Raman scattering is another Stokes process, in which high frequency phonons, often referred to as optical phonons, are created in the material. This process is responsible for the generally monotonic decrease in absorption as the InfraRed (IR) wavelength increases [38].

Direct measurement reveals total integrated losses from Raman Scattering are quite small in SiO_2, namely, $\alpha_{Ram} \approx 0.05/\lambda^4$ dB/Km or at $\lambda = 2$µm, $\alpha_{Ram}(2\ \mu m) \approx 2.5 \times 10^{-5}$ dB/Km which is approximately 5×10^{-5} ppm/cm, significantly lower than other scattering processes.

2.1.7 Intrinsic Absorption

Intrinsic absorption in the Ultraviolet (UV) region is caused by electronic absorption. Absorption occurs when a photon interacts with an electron and excites it to a higher energy level. The main cause of intrinsic absorption in the IR region is due to the characteristic vibration frequency of atomic bonds in the material.

Multi-phonon absorption

The long-wavelength limit of the transparency range is called the infrared absorption edge and it is often determined by the onset of strong multi-phonon absorption. Multi-phonon absorption occurs when two or more phonons simultaneously interact to produce an electric dipole moment with which the incident radiation may couple [45]. These dipoles can absorb energy from the incident radiation, reaching a maximum coupling with the radiation when the frequency is equal to the vibrational mode of the dipole in the far-infrared. The vibration modes are complex, comprising several different types of vibrations. There are two modes of vibrations of atoms in solids, longitudinal and transverse. In the longitudinal mode the displacement of atoms from their positions of equilibrium coincides with the propagation direction of the wave. For transverse modes, atoms move perpendicular to the propagation of the wave.

The observed IR absorption edge for FS is related to the stretching mode of Si–O bonds, which has a wavenumber of ≈ 1000 cm^{-1}. Single-phonon absorption would thus require an optical wavelength of ≈ 9 µm [46]. However, due to multi-phonon processes, significant absorption occurs at wavelengths below 2 µm as shown in Figure 2.4.

In low OH FS, these phonons correspond to excitation of Si-O bond vibrational modes, and result in significant attenuation of the laser beam and heating for wavelengths longer than about 2 µm, as shown in Figure 2.4. If the OH contamination in the FS is not negligible, the fundamental IR absorption due to Si-OH bonds occurs

at 2.75 µm, with overtones due to anharmonicity at 1.37 µm and 0.94 µm, and an absorption band near 2.22 µm due to scattering into a Si-O phonon [47].

Multiphonon absorption generally determines the infrared absorption edge of optical materials. In order to achieve good transmission at longer wavelengths, one has to use optical materials with particularly low phonon energies. The intrinsic multi-phonon absorption related to the Si-O bond is the major contributor to absorption at wavelengths > 1.6 µm and can limit the applicability of FS for infrared applications especially in the mid-IR due to rising multiphonon absorption with increasing wavelength.

2.1.8 Extrinsic Absorption

Extrinsic absorption is caused by interaction with impurities introduced into the material during fabrication such as metals and hydroxyl OH [47]. Photons interact with the electronic transition of these impurities leading to localised absorption. Low loss FS is often manufactured using a modified chemical vapour deposition process minimizing impurities during fabrication. Typical trace impurities found in Suprasil 3002 are less than 0.01 ppm [43].

Depending on the fabrication process, the silica glass can be more or less contaminated with water, which leads to OH groups. The fundamental resonance of the OH groups corresponds to wavelengths of approximately 2.75 µm, and the second overtone at approximately 1.38 µm falls into the intrinsic low-loss window of silica, forming an absorption peak that can be detrimental for optical fibre communications in the 1.5 µm spectral region. The third harmonic yields a peak at approximately 0.95 µm. These "OH overtone absorption peaks" constitute extrinsic losses, which can be minimized by resorting to fabrication techniques which lead to a minimum hydroxyl content of the material [48].

2.2 Review of Measurement Techniques

Optical absorption has been measured using a variety of techniques:

- Transmission, which uses the observed transmittance through the test sample. These are reviewed in Section 2.2.1

- "Thermal lensing", which uses the change in the shape of the TEM_{00} eigenmode of on optical system due to the absorption induced wavefront distortion. These techniques are reviewed in Section 2.3.
- Photothermal deflection, which uses the change in the propagation direction of a probe beam due to the absorption-induced wavefront distortion. This is detected using a segmented photodiode or interferometry. These techniques are reviewed in section 2.4
- Wavefront sensor, which detects the change in the probe beam using a pixelated sensor. These are discussed in Section 2.4.3

The last three techniques are well suited to measurement of low absorpitive materials as they are largely insensitive to non-absorption losses, such as elastic scattering.

2.2.1 Transmission Measurements

Spectrophotometry

In spectrophotometry, a narrowband probe beam is passed through a sample and transmitted power is measured. Most modern spectrophotometers are double beam systems, which compare the intensity of a reference beam transmitted through free space and that of the beam transmitted through a sample. Thus, they determine the total attenuation of the beam though the test sample due to absorption, scatter loss and Fresnel reflections.

An example of this is the Cary 5000 UV-Vis-NIR spectrophotometer which was used to determine the loss in BK7 (Section 4.2). The standard deviation for the UV-Visible range is < 0.005 and for Near Infra-Red (NIR) is 0.02. The accuracy tolerance for UV-Vis is +/- 0.08 nm and NIR is +/- 0.4 nm. As such current spectrophotometry methods are of limited use in weakly absorbing materials.

Fourier-Transform Infra-Red Spectroscopy

An alternative technique that allows simultaneous measurement of the entire spectral range is Fourier-Transform Infra-Red spectroscopy (FTIR) spectroscopy. Light from a broadband source that covers the required spectrum is passed through a Michelson interferometer to generate the probe beam. The Michelson interferom-

eter is adjusted during the measurement process to modify the spectrum of the incident light, yielding a set of transmission measurements – each for a different incident spectrum. The transmission data is analysed using Fourier transforms to yield the absorption spectrum for the sample [49]. FTIR achieves a higher sensitivity than conventional spectrophotometry and has better wavelength accuracy since the wavelength is calibrated using a laser beam of known wavelength that passes through the interferometer. This is much more stable and accurate than in dispersive instruments where the scale depends on the mechanical movement of diffraction gratings [50].

Advantages of FTIR techniques include speed and broad wavelength range but current high resolution FTIR spectrometers are limited to $\alpha \geq 1000$ ppm/cm [49] and as such are not suitable for materials with absorption coefficients in the ppm/cm range.

Cut Back Techniques

The cut-back technique is useful for optical systems in which the propogation length can be varied, such as optical fibres, as indicated in Figure 2.5.

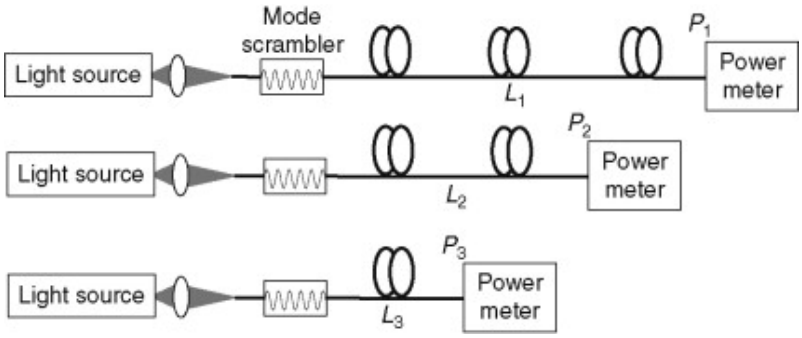

Figure 2.5: Illustration of the cutback technique to measure fibre loss. The mode scrambler is be used to stabilize the power distribution of the guided modes and strip out cladding modes [51].

Assuming a power P_0 is incident on the optical system, the power at a distance z from the input of the fibre is given by $P(z) = P_0 e^{\alpha z}$. With the same optical power incident onto optics of differing lengths, the average absorption (and scatter) coefficient is determined using

$$\alpha = \frac{\left[\ln\left(\frac{P_2}{P_1}\right)\right]}{(L_1 - L_2)} \tag{2.5}$$

The accuracy of the cut-back technique is dependent on the accuracy and resolution of the power measurements, and while cut-back measurements scale well with length and as such are excellent for measuring loss in fibre, they do not separate scatter from absorption are of little use for measurement of bulk optics of weakly absorbing material.

2.3 Thermal lensing techniques

Thermal lensing occurs when there is a transverse gradient in the temperature profile across an optic. The optic is hotter on the beam axis, compared with the outer regions, typically causing some transverse gradient of the refractive index called the thermooptic or thermorefractive effect and quantified with the coefficient, dn/dT. Further index changes can be caused by thermally induced mechanical stress (photoelastic effect, quantified with photoelastic coefficients and the thermal expansion coefficient, α_{CTE}). Mechanical stress can also lead to bulging of the end faces of the optic, so that these also cause lensing. This effect can be important for long optics.

In these techniques the wavefront distortion is assumed to be quadratic, thus producing an additional "thermal lens" that modifies the optical system. An early application of the thermal lens approach was reported by Leite et al [52]. In this demonstration, a weakly absorbing test sample was placed within a laser cavity and the change in the eigenmode due to the thermally-induced lens was used to determine the absorption coefficient. The sensitivity of the measurement was estimated to be 100 ppm/cm. The thermal lens can also be estimated by measuring the change in the location of the waist of a separate probe beam [53, 54].

2.3.1 GEO600

GEO600 is a gravitational-wave detector located near Sarstedt in Germany. It is designed and operated by scientists from the Max Planck Institute for Gravitational Physics, Max Planck Institute of Quantum Optics and the Leibniz Universität Hannover, along with University of Glasgow, University of Birmingham and Cardiff University in the United Kingdom, and is funded by the Max Planck Society and the Science and Technology Facilities Council.

Hild et. al. [3] developed a technique to measure the absorption inside the beam splitter of the GEO 600 interferometer. Using the GEO 600 parameters and assum-

ing no absorption, a FINESSE[1] model of the interferometer was created. Additional lenses were placed in the simulation and their focal lengths varied until the TEM_{00} eigenmode of the system matched the observed beam shape. (Figure 2.6). The absorption, assumed to be due only to the substrate was then calculated using a thermorefractive model of the beam splitter and the power of the transmitted beam. Estimated bulk absorption was less than 0.25 ± 0.1 ppm/cm for a piece of Suprasil 311 SV at a wavelength of 1064 nm.

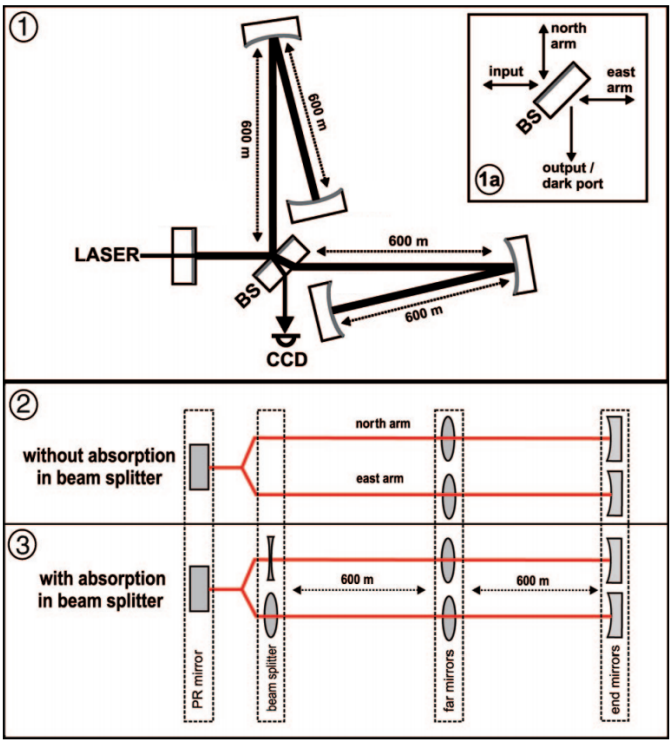

Figure 2.6: (1) Simplified optical layout of the GEO 600 interferometer.(2) Optical system for the case of no absorption within the beam-splitter substrate. (3) Absorption in the beam splitter was modelled by an additional negative lens inside the east arm (dominant effect) and a positive lens in the north arm. [3]

This method relies on accurate measurement of input power and does not take into account scattering losses and hence can only detect an upper limit of absorption while being limited to measuring the materials in the current GEO600 Interferometer (IFO).

This is one of the highest resolution measurements of absorption in FS but is not feasible for measurement of new materials or different wavelengths.

[1]Frequency domain INterferomEter Simulation SoftwarE is a tool developed at GEO600 for designing and debugging interferometers.

2.4 Photothermal Deflection Techniques

Photothermal Deflection Spectroscopy (PDS) is a pump/probe technique in which the temperature gradient resulting from pump absorption in the test material causes a refractive index gradient that deflects a probe beam. The probe beam can travel through the test material or through an adjacent material that is in good thermal contact. Additionally, the probe beam can travel transverse to the pump beam [55], which would enable movement of the absorption along the pump beam propagation direction but limits the sensitivity for weak absorbers, or colinear with the pump beam.

2.4.1 Colinear Mirage Bench

A colinear photothermal detection bench, known as a colinear 'mirage' PDS, makes use of a position-modulated heating source instead of the classic power-modulated source. A schematic of the colinear 'mirage' PDS system is shown in Figures 2.7 and 2.8.

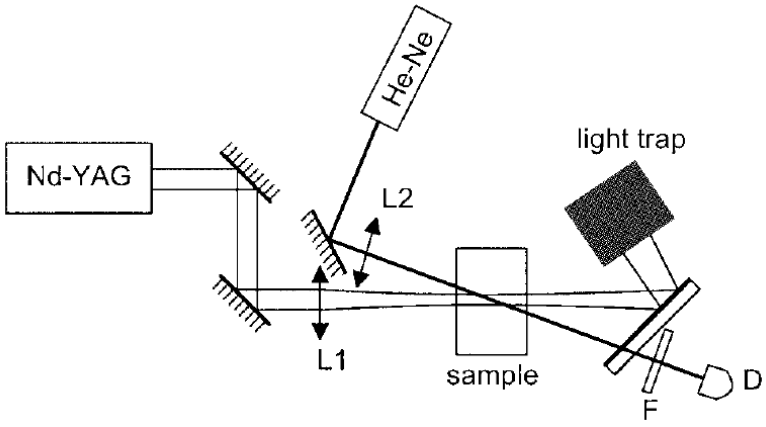

Figure 2.7: Schematic of the colinear mirage setup. To modulate the pump beam, either a mechanical chopper is inserted between the two mirrors of the periscope or the second periscope mirror is tilted by use of a piezo-motorized mirror holder. The 24-W Nd:YAG pump beam is focused inside the sample by an f = 200 mm lens (L1). The 1-mW He–Ne probe beam is focused by an f = 80 mm lens (L2). An interference filter (F) and a mirror protect the two-quadrant detector (D) from spurious light [56].

In this schematic, the Nd:YAG pump beam is focussed by lens L1 into the test material. The HeNe laser probe beam, which has a diameter much less than that of the pump beam, passes through the test material displaced a distance, ω_{pump}, from

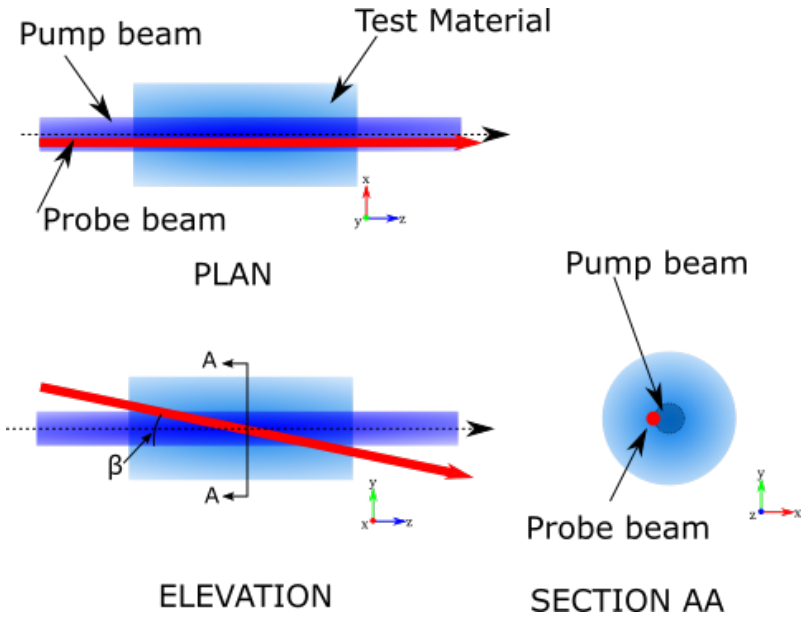

Figure 2.8: Schematic showing the alignment of the probe and pump beams in the colinear mirage setup.

the centre of the pump beam and at an angle, β, as shown in Figure 2.8 [56]. A 2-segment photodiode is used to measure the lateral deflection of the probe beam by the pump absorption.

The sensitivity of the mirage technique can be improved by chopping the pump beam or modulating the position of the pump beam [56]. Its accuracy is affected by uncertainties in the geometrical parameters such as angle, β, pump beam $1/e^2$ radius, ω, the location of the probe beam, the alignment of the probe beam axis relative top the pump beam axis, the non-negligible width of the probe beam and changes in the shape of the probe beam during the deflection. The accuracy has been estimated to be 10%.

2.4.2 Photothermal Common-path Interferometry

Photothermal Common-path Interferometry (PCI) [57] is the current standard for measuring absorption in low absorption materials. It is based on a pump/probe beam technique similar to the mirage bench above. The distortion of the probe beam profile in the central area results in an alteration of the total beam profile from Gaussian due to interference of the distorted and undistorted parts of the probe.

The probe distortion starts as a small perturbation of the wavefront caused by effects such as refractive index change with temperature (dn/dT), thermal expansion and or photo-elastic refractive index change as a result of local stresses around the heated area. Over distance, the phase perturbation transforms into amplitude contrast. The interference maximum, which depends besides other parameters, on the absorption coefficient, is then detected by a photodetector and is processed by a lock-in amplifier.

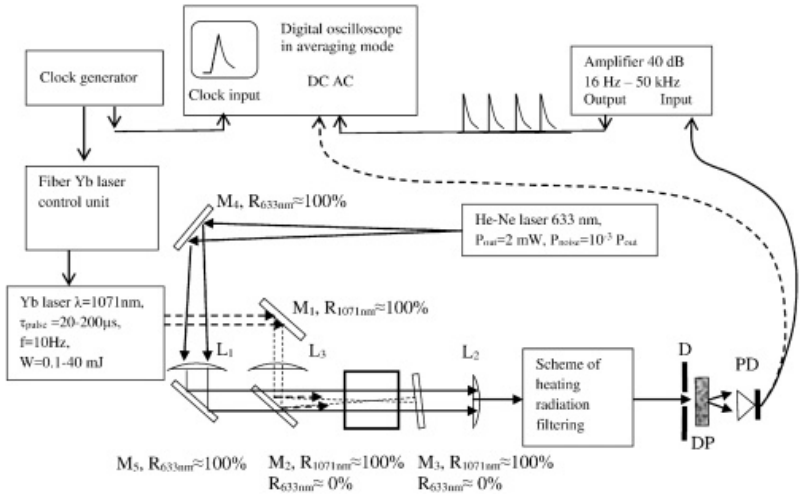

Figure 2.9: Schematic diagram of optical layout and measurement scheme for Photothermal Common-Path Interferometery. [4].

Vlasova et.al. [4] measured absorption in Suprasil 311 silica glass to be $\alpha = 2.8$ ppm/cm at a wavelength of 1071 nm with a signal-to-noise ratio of 20 dB. To calibrate this scheme, a theory of diffraction on deformations was developed taking into account the stresses arising in an inhomogeneous temperature field.

2.4.3 Shack-Hartmann wavefront detector

Shack-Hartmann sensors use micro-lens arrays to sample the wavefront and thus optimize the light collection efficiency, but they are susceptible to imperfections in the micro-lens array [58]. While the effect of these imperfections can be partially reduced by calibration of the system, they can not be fully removed as the resulting aberration of the calibrating wavefront by the imperfection is, in general, different from that imposed on an unknown wavefront.

Utilizing a Shack-Hartmann wavefront detector, Sanichiro Yoshida et al. [2] used the thermal lensing to determine the absorption in FS. The absorption coefficient was estimated by fitting the observed deformation to a thermal lensing model based on the temperature dependencies of the refractive index and the thermal expansion

coefficient of the material. For a particular sample of FS, the absorption coefficient was determined to be 180 ± 40 ppm/cm @ 1064 nm.

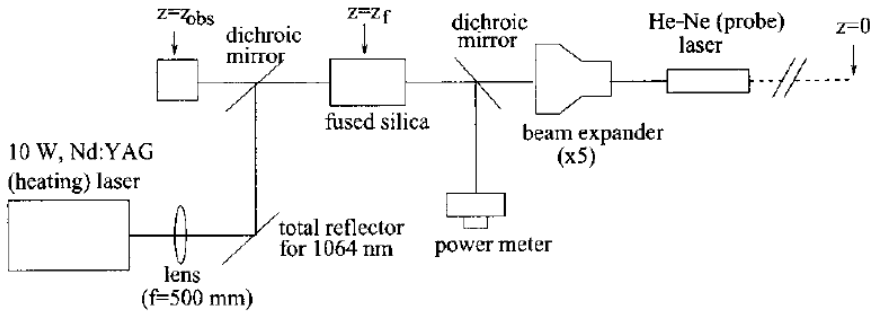

Figure 2.10: Experimental setup as used by Yoshida et. al. using Shack-Hartmann wavefront detector with alignment similar to that described in Section 3.1. [2].

2.5 Summary

As was discussed in Section 2.1, there are many processes that can result in attenuation of light as it passes through a transparent material. We are concerned with those that deposit energy within the material, however, and thus it is important that the measurement system directly probes these effects.

The photothermal technique described in Section 2.4 appears well-suited to our needs. The wavefront measurement technique would appear superior as it can increase the wavefront distortion signal by increasing the length of the sample and it can in principle measure the complete wavefront distortion of the probe beam.

A Shack-Hartmann wavefront sensor has been used for such a measurement but reported an uncertainty of 40 ppm/cm, which is inadequate for investigating the absorption in low-OH FS at 2 µm.

We shall demonstrate in this thesis a process that improves precision from previous measurements by utilising a differential Hartmann Wavefront Sensor (HWS). Improvements are due to averaging multiple images to reduce noise, utilising a long test sample to increace optical path length and avoiding the use of dichroic mirrors which may add to the uncertainty.

Chapter 3

Absorption Measurement System

This chapter discusses the development of a system to measure absorption in weakly absorbing materials with increased sensitivity and reproducibility compared with methods discussed in Chapter 2. The system measures the distortion of a probe beam due to absorption of the heating beam at the wavelength under investigation, using a differential Hartmann Wavefront Sensor (HWS). This chapter is laid out as follows:

Section 3.1 describes the initial on-axis measurement system in which the probe and pump beams propagate colinear within the test sample. This approach was developed to simplify data analysis and hence minimise uncertainty in the calculation of the absorption coefficient (α).

We then describe various aspects of the system that impact the system performance, including the heating beam in Section 3.5, the operation of the differential HWS in section Section 3.2 and spot centroiding in Section 3.3.

The sensitivity of the HWS is reported in Section 3.2 followed by a discussion in Section 3.6 of the properties of the probe beam required to maximise the sensitivity of the HWS.

Unfortunately, the dichroic mirrors used to guide the heating beam through the test sample were found to produce significant Wave Front Deformation (WFD) due to their own absorption. Additionally, the test sample appears to have significant internal refractive index inhomogeneity, which aberrates the probe wavefront.

Thus an off-axis measurement system is described in Section 3.8

3.1 Coaxial photothermal HWS measurement system

A coaxial photothermal measurement system where the probe and heating beams run colinearly along the test optic was developed to simplify the process of calculation the absorption coefficient. A schematic of the coaxial photothermal measurement system is shown in Figure 3.1.

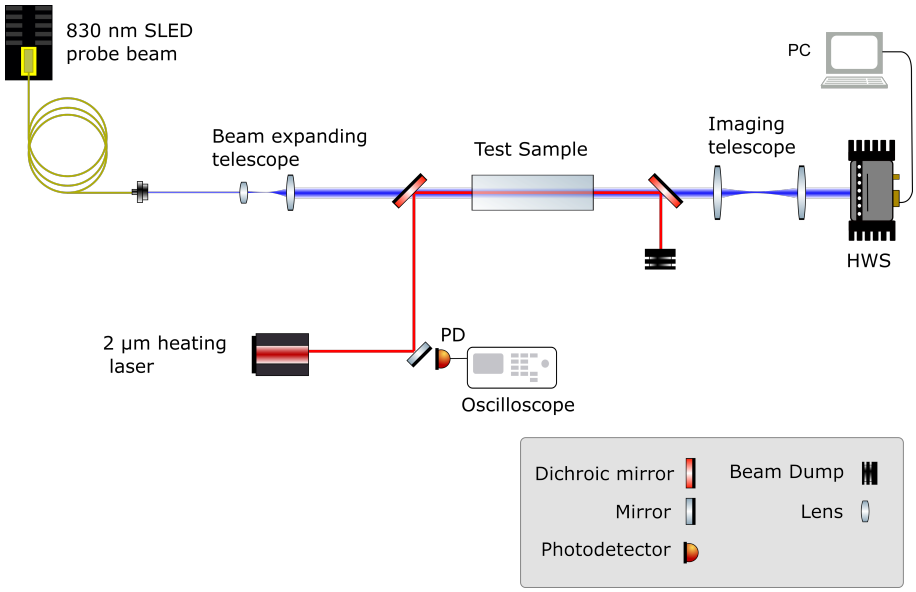

Figure 3.1: Schematic of on-axis measurement system showing colinear probe and heating beams.

The 2 µm heating laser beam is directed into the test sample via a front-surface dichroic mirror, propagating along the cylindrical axis of the sample producing a mostly radial temperature gradient. Once the heating beam has exited the test sample it is directed by a second dichroic mirror into a beam dump. The photodiode (PD) is used to monitor the power of the heating beam.

The dichroics were custom-made by Rocky Mountain Instrument Co. and had nominal Reflection >99.5% at 2.0 µm and Transmission >95% at 830 nm (Figure 3.2).

The test sample was supported using two translation stages separated by 20 cm such that each face of the sample could be independently translated (Figure 3.3). This was to ensure the probe beam propagated along the axis. The sample rested

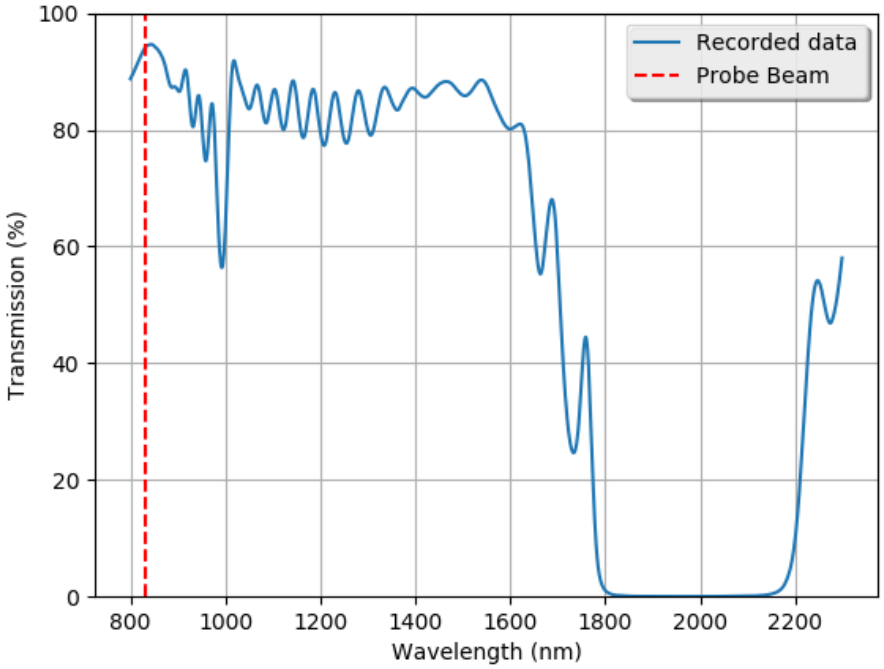

Figure 3.2: Transmission of dichroics at 45° angle of incidence measured using a Carry NIR UV VIS spectrophotometer.

on two pins attached to each stage to minimise thermal contact and reduce stress in the optic due to expansion.

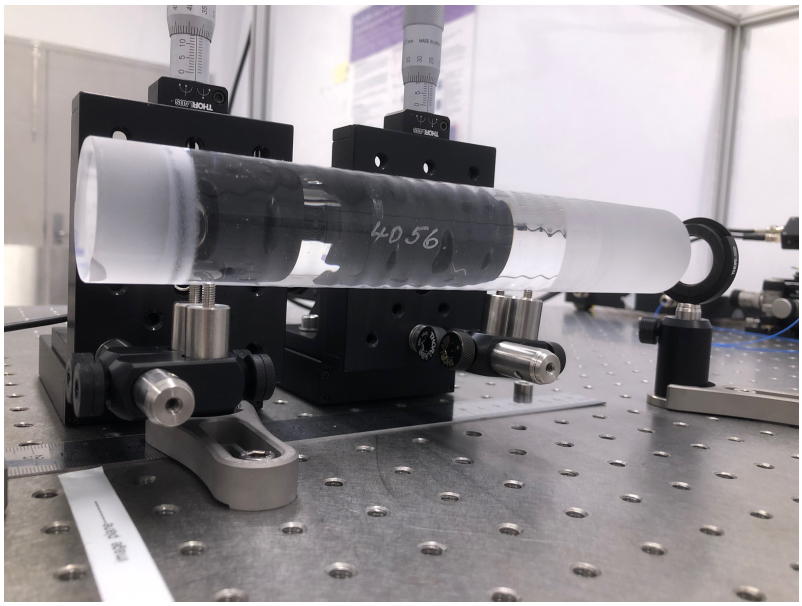

Figure 3.3: Dual x, y translation stages used to align the test optic to ensure that it is normal to the probe beam while pins are used to support the optic while minimising thermal conduction. Low transmission at 830 nm due to Fresnel reflection which is not accounted for in Spectrometer measurement.

A single-mode fibre-coupled 830 nm Super Luminescent Diode (SLD) was used to produce a probe beam with good spatial coherence but low temporal coherence to prevent interference fringes due to stray reflections. The probe beam was expanded to 8.5 mm in diameter using a Fibre Collimator (F220APC-850) and an AR-Coated Galilean Beam Expander (Thorlabs), then transmitted through the dichroics and the test sample.

To maximize resolution in the area of interest a 4x magnification image-relay telescope consisting of 50.8 mm diameter lenses with $f_1 = 250$ mm and $f_2 = 1000$ mm, was used to image the probe beam wavefront at the exit face of the sample onto the HWS.

3.2 Differential Hartmann Wavefront Sensor

Hartmann Wavefront Sensors (HWSs), in their simplest form, consist of an array of apertures within an opaque plate, often referred to as a Hartmann Plate (HP), which samples an incident Wave Front (WF), as shown in Figure 3.4. The ray produced by each aperture propagates perpendicular to the local wavefront and creates a spot when it reaches the sensor. The positions of these spots are used to determine the wavefront or properties of the optical system that created the wavefront.

First reported in 1904 [59,60], they were used to examine the shape of spherical astronomical mirrors. They have since been used to test and align a variety of optical systems [61]. More recently, differential HWS are being used for real-time ultra-high sensitivity and accurate measurements of absorption-induced wavefront distortion in advanced Gravitational-Wave (GW) detectors [29].

Shack-Hartmann sensors, in which the HP consists of an array of micro-lenses are used for adaptive optics in large ground based optical telescopes [62]. In this application, light from a guide star is measured to enable removal of atmospheric aberrations and thus improve the "seeing" of the telescope. They have also been used for corneal topographic measurements in ophthalmology [63].

In a differential HWS, illustrated in Figure 3.4, the locations of the spots produced when the probe beam passes through the unaberrated optical system are recorded, yielding a set of reference positions. Changes in the optical system lead to changes in these positions. If the change is small then the effect of aberration due to the other elements are common mode.

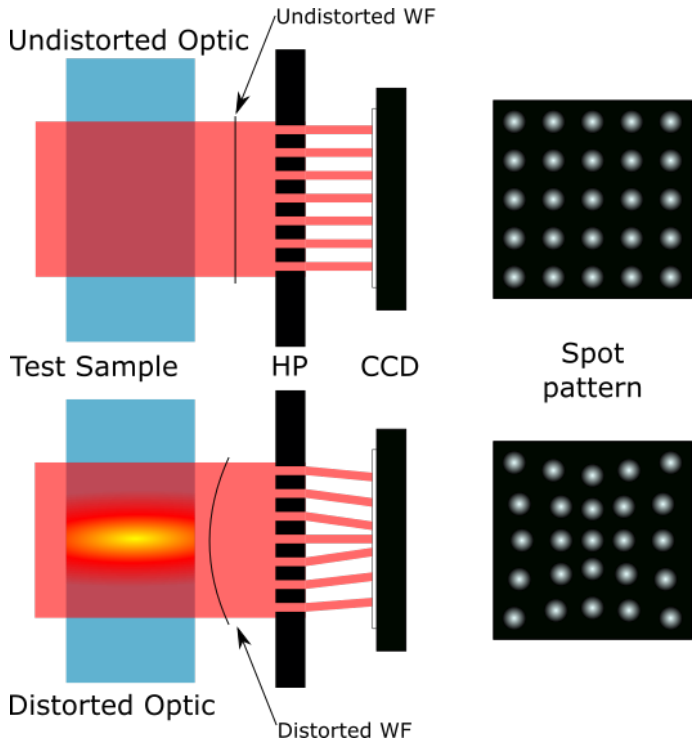

Figure 3.4: The Hartman Wavefront Sensor images the probe beam projected through the test sample onto the HP. The holes in the HP illuminate the CCD and images are recorded. The undistorted images are recorded (top) and used as a reference when compared with the distorted "live" images (lower). In this case the distortion is caused by heating of the test sample via absorption of the heating beam. The movement of the centroids on the CCD are calculated as a gradient field and numerically integrated to create the wavefront map.

There are a variety of commonly used arrangements of apertures: radial patterns, square arrays, or hexagonally closed-packed arrays. Brooks [64] determined that the optimal arrangement for measuring thermally-induced wavefront distortion in GW interferometers is a hexagonal closed-packed array.

The basic operation of a differential HWS can be described as follows:

1. The wavefronts, W_{ref} and $W_{aberrated}$, are incident sequentially on the Hartmann plate, each creating a set of rays.

2. The rays propagate normal to the wavefront a known distance L, referred to as the lever arm, and are incident on the Charged Coupled Device (CCD).

   The HWS used has an invar HP that had 850 holes, each of 150 µm diameter, in a hexagonal-closed-packed array with a pitch of 430 µm. The plate is mounted

on Dalsa 1M60 CCD camera using invar spacers, and has a nominal lever arm of 10 mm.

3. The spot pattern is recorded by the CCD as a digital image. Typical CCD frames are shown in Figure 3.5.

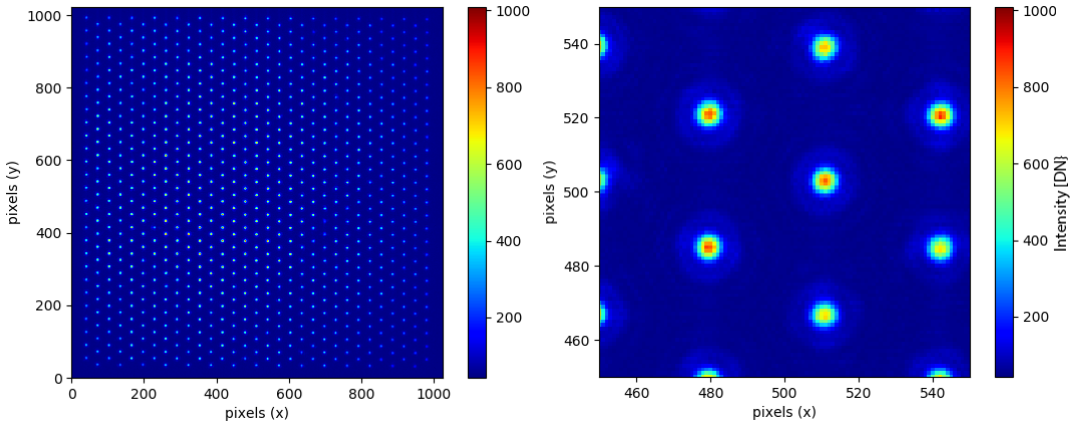

(a) Hartmann spots on CCD **(b)** Close up of Hartmann spots

Figure 3.5: False colour image example of a Hartmann spot pattern.

4. The position of the i^{th} spot, x_i, is determined by a centroiding algorithm.

5. The lateral displacement of each spot as the incident wavefront changes from W_{ref} to $W_{aberrated}$, Δx_i is calculated.

6. The angle between the i^{th} ray from the aberrated WF and its reference ray is equal to the displacement, Δx_i divided by the lever arm, $\Delta x_i/L$. The lever arm needs to be accurately known in order to prevent systematic errors.

   Rayces [66] showed that this angle is approximately proportional to the gradient of the wavefront change. Figure 3.6 shows an aberrated wavefront, PC, and a spherical reference wavefront, SC, of radius R centred at Q. The wavefront change (aberration), ΔW, is defined as the distance PS. Rayces determined the following relation:

$$\frac{\partial \Delta W}{\partial x} = \frac{|QT|}{|QS| - \Delta W} \tag{3.1}$$

   which can be simplified to

$$\frac{\partial \Delta W}{\partial x} \approx \frac{\Delta x}{L} \tag{3.2}$$

   if $L \ll R$ and $\Delta W \ll L$.

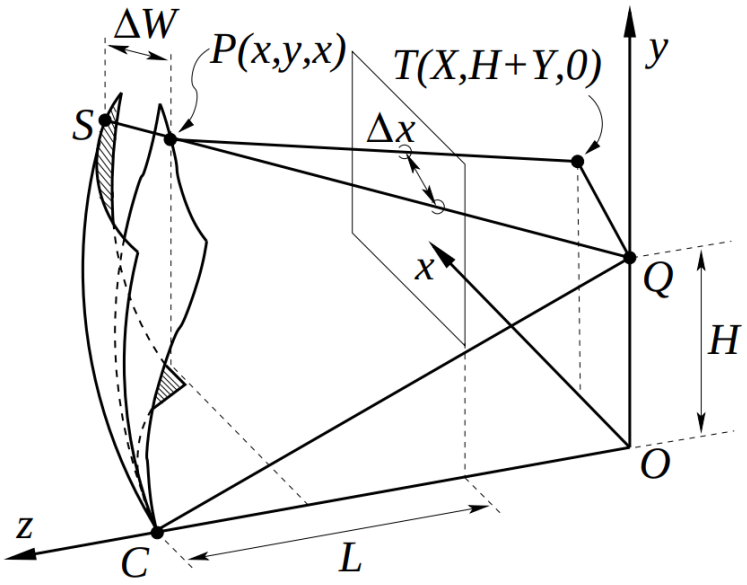

Figure 3.6: Reference wavefront SC and aberrated wavefront PC (propagating to the right), QS = QC = R, PS = ΔW. Reproduced and revised version of the Figure from Rayces [65].

For absorption-induced wavefront distortion, $\Delta W \approx 10^{-7}$ m, $L \approx 10^{-2}$ m and the collimated reference wavefront is approximately flat (R ≈ inf) and as such these assumptions and approximation are therefore valid.

In general, of course, the spots on the CCD are displaced in two dimensions, x and y, and thus:

$$\frac{\partial \Delta W}{\partial x} \approx \frac{\Delta x}{L} \text{ and } \frac{\partial \Delta W}{\partial y} \approx \frac{\Delta y}{L} \tag{3.3}$$

These gradients can be represented as a 2D 'quiver plot', as shown in Figure 3.7.

7. The wavefront change, ΔW , is calculated by integrating the gradient field, giving Figure 3.8 in this case.

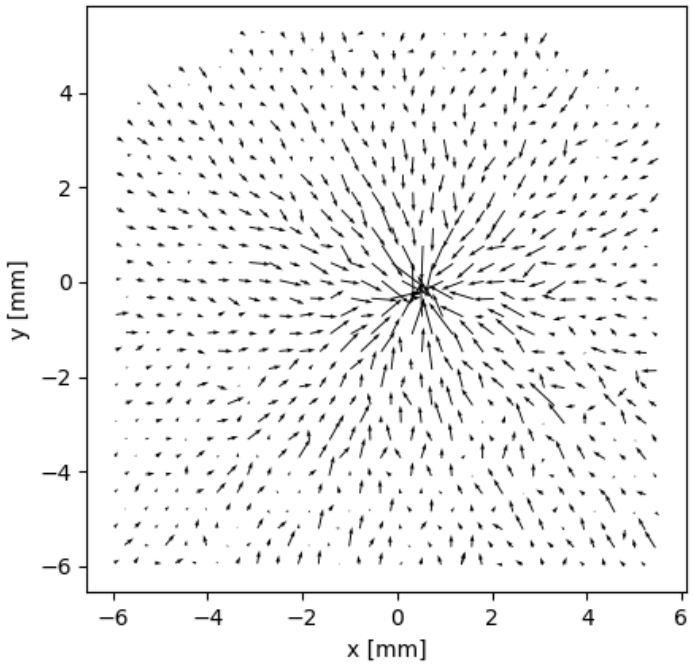

Figure 3.7: Example quiver plot showing discrete gradient field calculated.

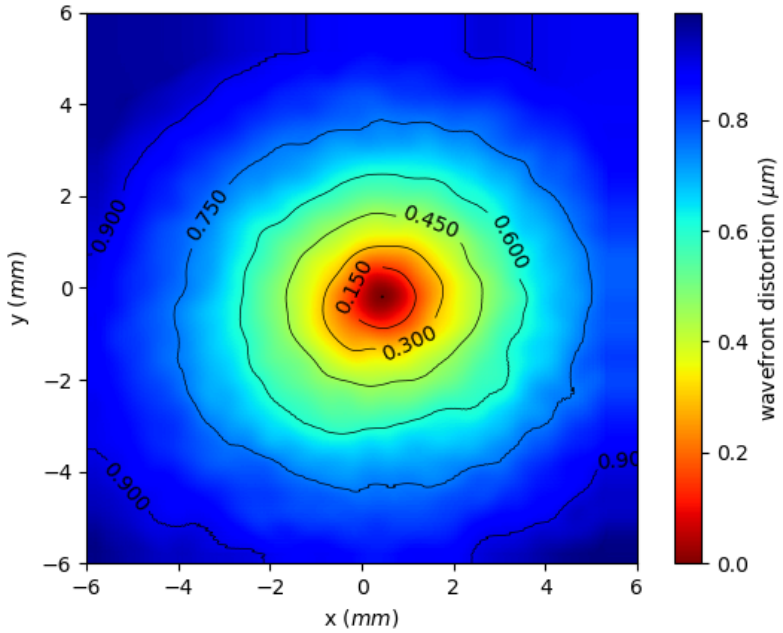

Figure 3.8: Integrated wavefront change

The techniques used to integrate the field and the propagation of errors in the integration are based largely on the work of Southwell [67] and Brooks [64].

The recording of the frames from the CCD, the spot centroiding, calculation of the wavefront gradients, numerical integration to determine the wavefront change, and least-square fitting of a set of polynomials to the wavefront data were done using the HWS code written by Won Kim. The analysis code is used by both the LIGO and Virgo collaborations to measure absorption-induced wavefront distortion in their core optics [29].

It has been shown that the differential HWS can measure changes in wavefront with a single frame RMS sensitivity of 0.44 nm that can be improved to 40 $\mathrm{pm_{RMS}}$ by averaging using multiple spot images [32]. It is thus suitable for measuring absorption induced wavefront distortion in weakly absorbing materials such as low hydroxyl (OH) fused silica. Additionally, the operation of the HWS is simple and largely immune to aberrations in the imaging telescope.

3.3 Centroiding

As discussed in Section 3.2, a centroiding algorithm is used to locate the centres of the spots in the Hartmann image. The conventional form of this algorithm is

$$(x_c, y_c)_m = p_s \left(\frac{\sum_{i=N_m^{min}}^{i=N_m^{max}} \sum_{j=N_m^{min}}^{j=N_m^{max}} iI_{ij}}{\sum_{i=N_m^{min}}^{i=N_m^{max}} \sum_{j=M_m^{min}}^{j=M_m^{max}} I_{ij}}, \frac{\sum_{i=N_m^{min}}^{i=N_m^{max}} \sum_{j=M_m^{min}}^{j=M_m^{max}} jI_{ij}}{\sum_{i=N_m^{min}}^{i=N_m^{max}} \sum_{j=M_m^{min}}^{j=M_m^{max}} I_{ij}} \right) \tag{3.4}$$

where p_s is the pixel size, i and j are the CCD pixel indices in the horizontal and vertical directions, respectively, and I_{ij} is the intensity of the ij^{th} pixel.

This algorithm can give rise to systematic errors depending on the limits of summations, especially if the centroid of the spot is not at the centre of the detection area [68]. The centroid algorithm used here is based on the work of Southwell and Brooks [64, 67] and uses a weighted centre of gravity.

The algorithm applies a mask to the intensity distribution by using a weighting, $(F_w)_i$, that depends on the pixel Digital Number (DN). The basic 1-D form is:

$$x_{WCoG} = p_s \frac{\sum_{i=i_{min}}^{i_{max}} iI_i(F_w)_i}{\sum_{i=i_{min}}^{i_{max}} I_i(F_w)_i} \tag{3.5}$$

The weighting function is quite often chosen to be a Gaussian centred at the estimated spot centre. Using the weighting shown in Equations (3.6) and (3.7): preferentially weights pixels with higher intensities, reducing the effect of shot noise and reducing the overall noise in the centroid calculation [68].

$$(F_w)_i = I_i^{P-1} \tag{3.6}$$

and thus

$$x_{WCoG} = p_s \frac{\sum_{i=i_{min}}^{i_{max}} i I_i^P}{\sum_{i=i_{min}}^{i_{max}} I_i^P} \tag{3.7}$$

An example of a single spot and centroid location is shown in Figure 3.9

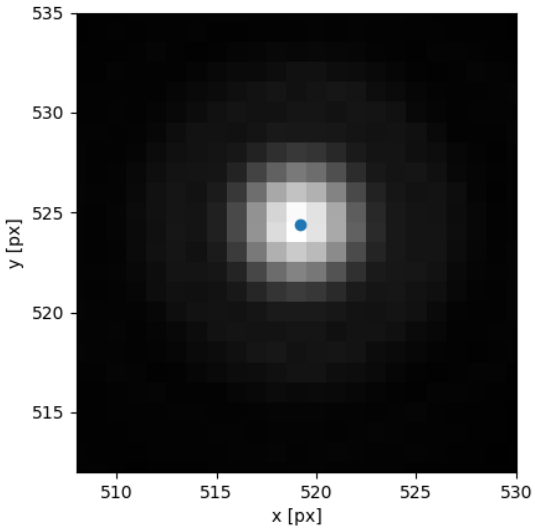

Figure 3.9: Example of spot and centroiding using WCoG algorithm.

The summation range $i_{min} \leq i \leq i_{max}$ is chosen such that the central pixel is the pixel with the maximum intensity. The range is symmetric about the central pixel, and thus includes an odd number of pixels.

Dark noise is subtracted to increase contrast, reducing fluctuations in centroid location. To determine the value used for the dark noise subtraction, a series of images were taken without illuminating the sensor. Pixel values were recorded for each frame and the mean value of dark noise calculated (Figure 3.10). A value of

55 DN was thus subtracted from live and reference images to ensure all dark noise was subtracted from the image.

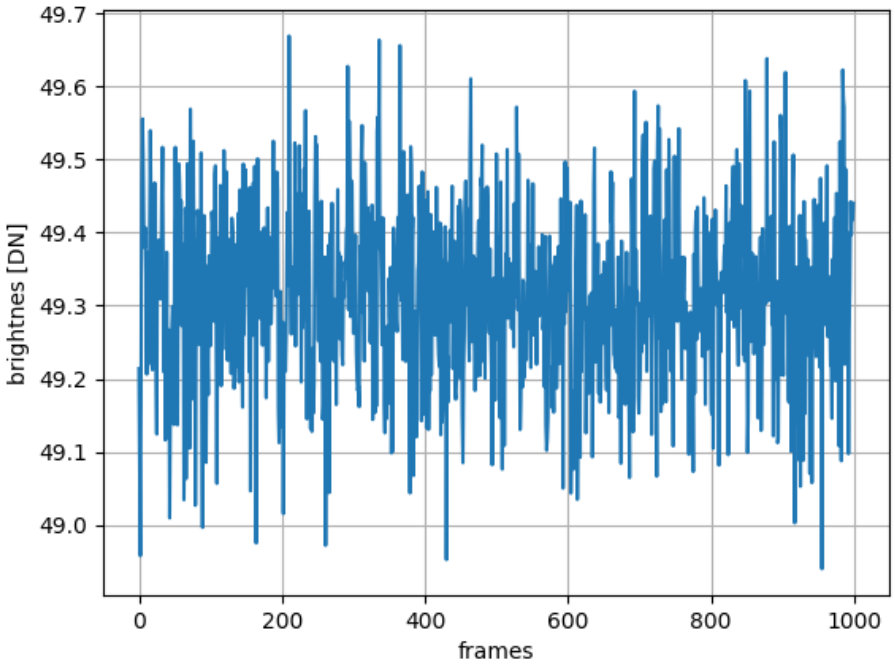

Figure 3.10: Average DN of each frame, for 1000 frames used to evaluate the amount of dark noise. A threshold level of 55 DN is thus subtracted from all frames.

The effect of *Hot Pixels*, which are blemishes on the CCD for which the DN is larger than expected and are generally unstable is also removed from the centroiding process. These hot pixels can introduce error in the centroid locations if they fall into the centroiding locations.

The location of the hot pixels were determined by recording 5000 frames without illuminating the sensor and looking for excessive or unstable DN values. The number of hot pixels remained constant while recording and hot pixels were located only in regions blocked by the Hartmann plate as seen in Figure 3.11 and hence can be ignored.

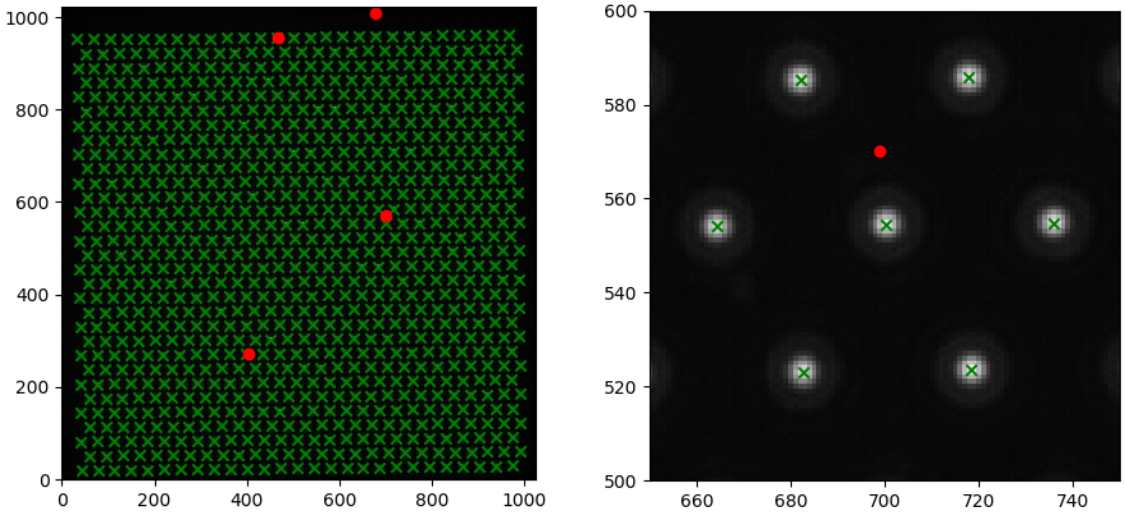

(a) Location of hot pixels above threshold value (red) compared to location of centroids (green).

(b) Close up of hot pixels (red) compared with respect to illuminated pixels and centroids location (green).

Figure 3.11: Location of 'hot' pixels on CCD compared with centroid locations.

3.4 Sensitivity of the HWS

3.4.1 Characterisation of CCD camera

A Charged Coupled Device (CCD) is an array of light-sensitive potential wells, formed by applying positive voltages to an array of metal electrodes on a metal-oxide-semiconductor, creating a 2D array of pixels. The potential well in each pixel collects photoelectrons produced in the semiconductor depletion region. The electrons are then sequentially transferred to a charge-to-voltage converter and the resulting voltages are digitized by an Anologue to Digital Converter to yield a DN output. A two-dimensional map of the incident light field is thus created.

Over exposure of a pixel can, however, result in leakage of charge into an adjacent pixel. This effect is known as blooming and it will reduce the quality of a digital image. Fortunately, modern scientific grade CCDs have antiblooming features that use an overflow drain below each pixel to prevent blooming for reasonable exposure levels. Charge flows into the drain before it is able to flow into adjacent pixels and is removed [69, 70]. The magnitude of the anti-blooming in a CCD refers to the multiple of the saturation level that can be applied to a pixel before any charge leaks into a neighbouring pixel. Ultimately, this feature allows the CCD to be used close to saturation level, improving its sensitivity.

The recording, transfer and digitization processes can introduce noise which degrades image fidelity and reduces the ability of Hartmann sensor to accurately locate the centroids of each spot in the image.

A Dalsa 1M60 CCD camera [71], the relevant parameters of which are listed in Table 3.1, was used. The technical information [64] indicates that it should be shot-noise limited (see below). A measurement that verified this conclusion is described in this section after a brief discussion of the various noise sources in the CCD. The magnitudes of these noise sources are collated in Table 3.2 for convenience.

Table 3.1: Specifications of Dalsa 1M60 CCD camera which utilizes an FTT 1010-M image sensor [71, 72].

Parameter	Value
Array Size	1024 x 1024 pixels
Pixel Size	12µm
Digitization	12 bits
Quantum efficiency @ 820 nm	$\approx 6\%$
Full Well capacity	350,000 electrons
Dark current @ 45°C	1.3×10^{-16}A per pixel
Random Readout noise (RMS)	1.2 DN
Fixed pattern noise	3.8 % RMS
Random non-uniformity	0.3 % RMS
Antiblooming	$\leq 100\times$ saturation level

CCD Noise

Noise sources that result in fluctuations in the DN are:

- Photon Shot Noise is caused by non-uniform arrival of the photons at the sensor. It can be calculated by dividing the number of electrons per pixel, N_e, by the Quantum Efficiency (QE)(@ 830 nm $\approx 6\%$) to determine the approximate number of photons, N_p, required to produce N_e electrons [73]. For the Dalsa 1M60, $N_p \approx 5.8 \times 10^6$ when N_e is equal to the maximum full well capacity value of 350,000 electrons. The RMS noise in the number of photons is $\sqrt{N_p}$. This can be expressed in electrons by multiplying by the QE. The maximum RMS fluctuation due to photon shot noise here is thus 145 electrons.
- Photoelectron Shot Noise arises because of the random nature of the photoelectric conversion process and is given by $\sqrt{N_e}$ [74]. For the maximum number of electrons in each pixel ($N_e = 350,000$) the RMS fluctuation due to photo electronshot noise is 592 electrons.

- Readout noise is due to noise sources within the sensor, including dark current and amplifier noise. Dark current refers to electrons that are thermally generated, rather than photo-generated. The HWS typically uses a short integration time ($\leq$ 50 ms) and thus dark current can be ignored. Amplifier noise is simply the noise introduced by the sensor electronics. The specified value in Table 3.1 [71] is 1.2 DN. This can be converted into electrons assuming a gain of 4096 DN per 350,000 electrons. The readout noise is thus 103 electrons

- Digitization noise is the uncertainty in the number of electrons in a pixel because of quantization into an n-bit scale. This is calculated using the following (See Appendix D)

$$\sigma_{digital} = \frac{1}{\sqrt{3}} \frac{N_{e_{max}}}{2^n}$$

  which gives a value of 49.3 electrons when $N_e = 350,000$ electrons and $n = 12$.

  The remaining noise sources specified by the camera manufacturer: fixed pattern noise and photoresponse non-uniformity, were small enough to be ignored as shown in Table 3.2.

Table 3.2: CCD Noise from each source expressed in electrons(el).

Noise Type	RMS value (el)	% of total variance
Photon shot noise	145	5.40%
Photoelectron shot noise	592	91.2%
Random readout noise	103	2.76%
Digitization noise @ 12-bits	49.3	0.63%
Fixed Pattern noise	3.9	0.004%
Random non-uniformity	0.3	2×10^{-5}%

3.4.2 Sensitivity of HWS

The wavefront error due to noise in the CCD sensor was measured using the system shown in Figure 3.12. Spot centroids were calculated for consecutive Hartmann images and the average prism in each image was removed by setting the average of all centroids in an image to be the same for all images. These centroids were used to investigate the fluctuations in the gradient field and the subsequent wavefront change.

A typical gradient field and map of the wavefront distortion are shown in Figures 3.13a and 3.13b. The RMS error for these maps varied between 0.82 nm and 0.41 nm which is consistent with the shot noise limit [64].

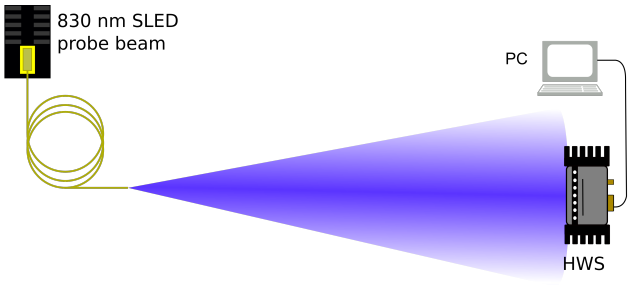

Figure 3.12: Experimental setup to test the precision of the Hartmann sensor using a single-mode fibre-coupled SLED that directly illuminates the sensor.

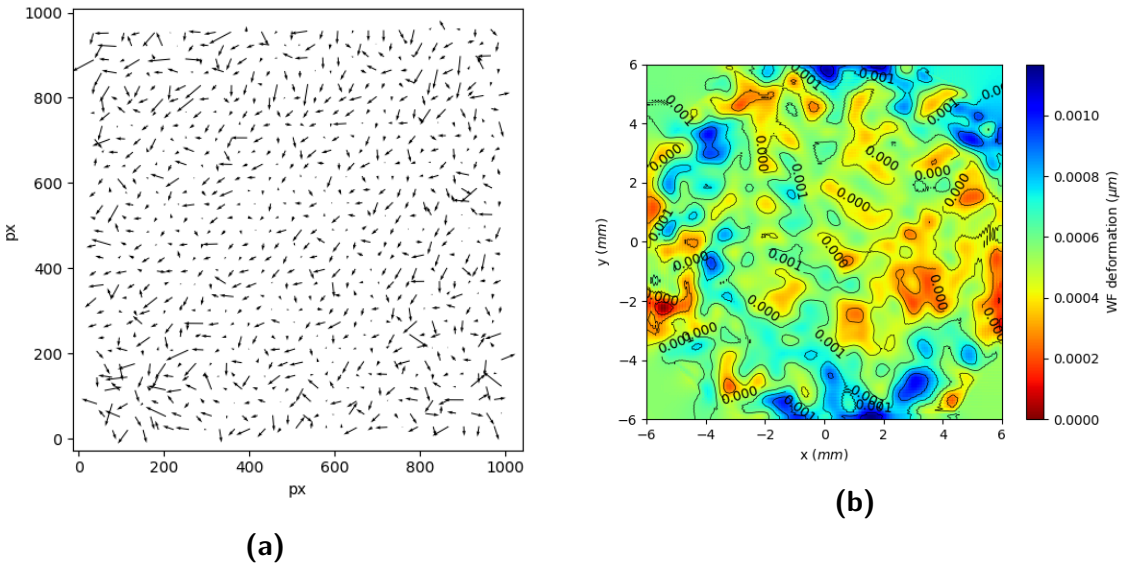

(a) **(b)**

Figure 3.13: Hartmann sensor measurement of the background shot-noise level made by comparing two Hartmann images separated in time by approximately 10 seconds. Shown are a) the gradient field of the apparent wavefront change and b) a numerical reconstruction of the apparent wavefront change.

Variations of the apparent wavefront change as a function of radial distance from the centre of Figure 3.13b are plotted in Figure 3.14 for several horizontal slices through the wavefront map.

The mean square error (variance) in the reconstructed wavefront, σ_W^2, depends on the variance in the wavefront difference between adjacent holes, $\sigma_{\Delta W}^2$. It can be calculated using

$$\sigma_W^2 = C_{\Delta W} \sigma_{\Delta W}^2 \tag{3.8}$$

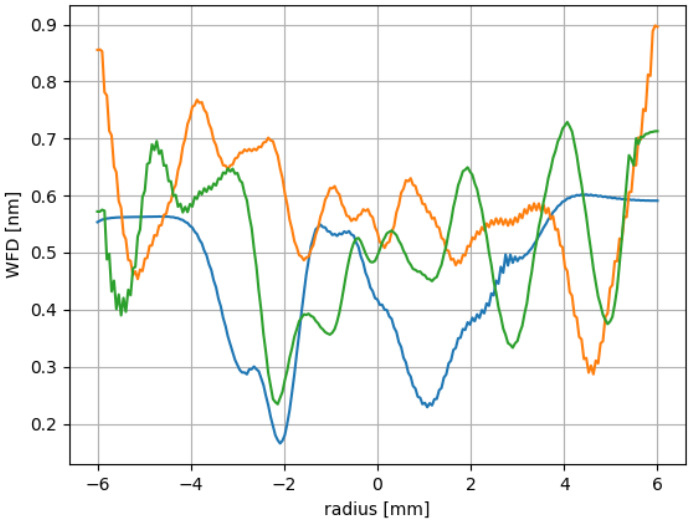

Figure 3.14: Wavefront slices showing noise floor

where $C_{\Delta W}$ is the Southwell noise coefficient [67], and the variance in the wavefront difference between adjacent holes, $\sigma^2_{\Delta W}$, is given by

$$\sigma^2_{\Delta W} = \left[\frac{h_p}{L}\left(\frac{\sigma_{x_c} + \sigma_{y_c}}{2}\right)\right]^2 \tag{3.9}$$

where σ_{x_c} and σ_{y_c} are the RMS errors in the x and y centroids, respectively, h_p is the distance between the holes in the Hartmann plate and L is the lever arm of the Hartmann sensor.

If the noise in the gradient field is stationary (i.e. the statistical characteristics of the noise does not vary with time) then the wavefront error should be reduced by averaging over multiple Hartmann images such that

$$\sigma_{\Delta W} \propto N_{avg}^{-1/2} \tag{3.10}$$

A sequence of 5000 Hartmann images were recorded at 58 images/second and the average prism removed from each image, to minimise the effect of drift in the alignment of the probe beam onto the Hartmann Plate. A set of reference centroids was then calculated by averaging 1000 images, consisting of the first and last 500 images, $\text{ref}_1 + \text{ref}_2$ as shown in Figure 3.15.

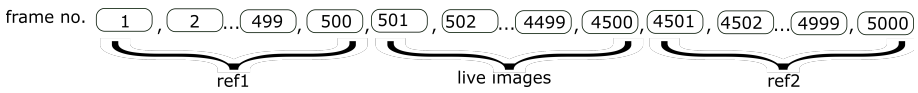

Figure 3.15: Graphic showing selection of frames for investigating noise reduction due to averaging. Reference centroids were created by averaging the first and last 500 images.

The remaining images were used to calculate sets of centroids averaged over N_{avg} images where $N_{avg} = 1-4000$. This approach ensured the reference and live centroids were statistically independent. The dependence of $\sigma_{\Delta W}$, on N_{avg} is plotted in Figure 3.16.

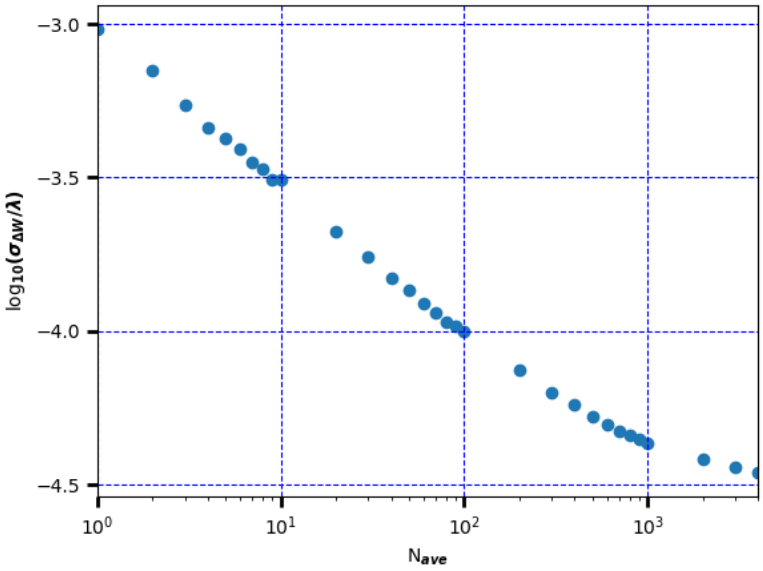

Figure 3.16: The improvement in HWS sensitivity due to averaging over N_{avg} Hartmann images.

For $N_{avg} < 100$, $\sigma_{\Delta W} \propto N_{avg}^{-1/2}$ as expected. At larger values of N_{avg}, slow changes in the temperature of the HWS introduce non-stationary noise as shown in Figure 3.17 and $\sigma_{\Delta W}$ decreases more slowly than $N_{avg}^{-1/2}$

The temperature dependence of the HWS is due to:

- thermal expansion of the CCD.
- thermal expansion of the plate spacers causes a increase in lever arm length
- thermal expansion of the HP itself causeing an increase in hole spacing.
- increase in CCD noise as discussed in Section 3.4.1

Thermal effects in the HWS are dominated by the thermal expansion of the HP and leads to systematic error equivalent to defocus, S, (See Appendix C).

Thus, the HP and spacers are made from Invar to minimise thermal expansion as it has a low coefficient of thermal expansion ($\alpha_{CTE} = 1.2 \times 10^{-6}$ K^{-1}). For an Invar HP and lever arm length, $L = 10$ mm, the temperature dependent defocus error can be determined using the following:

$$\frac{S_{thermal}}{\Delta T} = 120\,\mu\text{D/K}$$

where $S_{thermal}$ is the spherical defocus and ΔT the change in temperature.

From this it one can specify the maximum permissible temperature fluctuation, ΔT_{max}, such that the error from this source is not greater than the wavefront error $W_{\epsilon_{max}} = \lambda/467@830$ nm $= 1.35$ nm.

$$\begin{aligned}\Delta T_{max} &= W_{\epsilon_{max}} \left(\frac{2}{d^2 \frac{S_{thermal}}{\Delta T}} \right) \\ &\approx 0.04K\end{aligned}$$

To further reduce uncertainties caused by thermal fluctuations, a TEC cooling system was developed to stabilize the temperature of the camera whilst minimising air currents. This was constructed using thermoelectric coolers sandwiched between a copper plate (cold side) and aluminium heat sinks (hot side) fixed to each side of the camera. This was designed to be able to remove ≥ 20 Watts and is controlled using a Laird PR-59 PID Temperature Controller to produce a temperature stability of $\pm$ 0.02 K as shown in Figure 3.18. The resulting change in ΔW is shown in Figure 3.17b.

To determine the maximum allowable operating temperature of the camera, camera frames were recorded with no illumination and the number of hot pixels counted as the set-point of the temperature controller was changed. It can be seen from Figure 3.19 that the number of hot pixels rapidly increases at temperatures above 35 °C. A set point temperature of 28 °C was thus chosen.

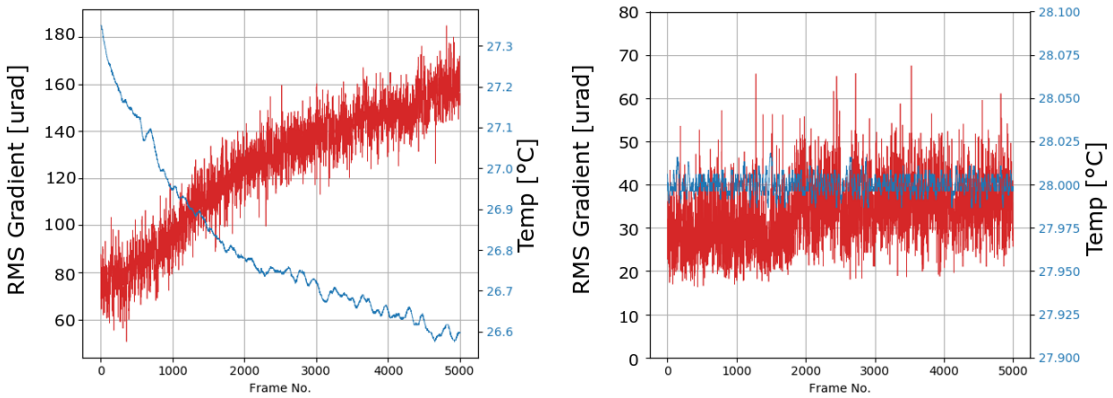

Figure 3.17: Plots showing temperature dependence of the HWS gradient fields, (a) before and (b) after temperature stabilisation of the HWS camera.

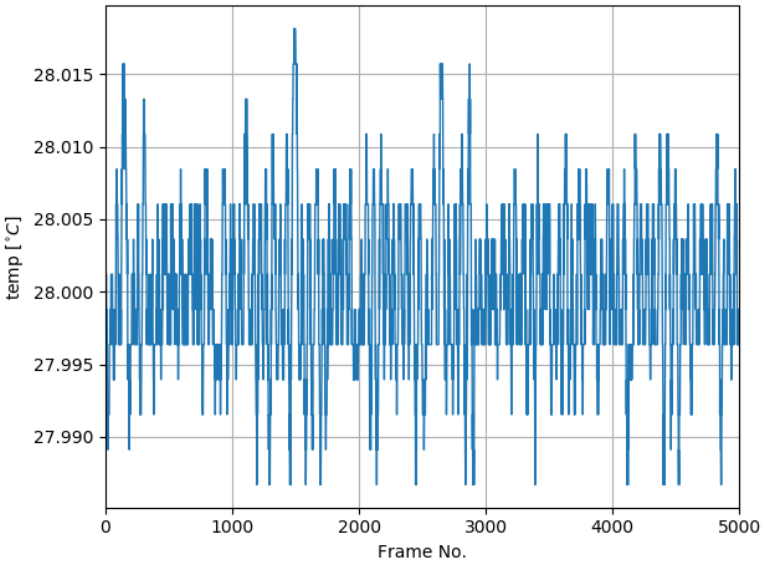

Figure 3.18: Variation of camera temperature after stabilization, recorded using the PID temperature controller probe.

The largest source or error in the sensor is expected to be random noise in the CCD (shot noise, readout noise and digitization uncertainty). This will contribute an error of approximately 0.6 nm to a wavefront measurement of thermal lensing. This is substantially better than the sensitivity required for absorption induced wavefront distortion measurement proposed.

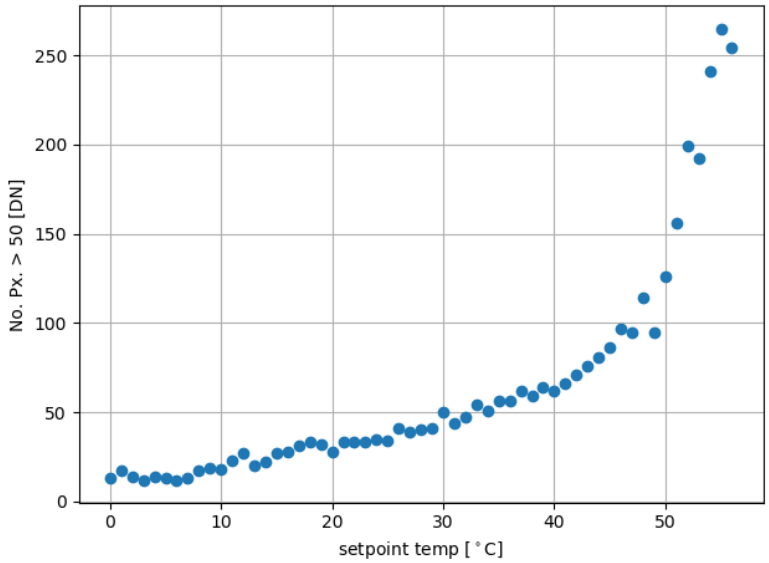

Figure 3.19: Number of hot pixels above threshold value (50 DN) in a 100-frame average as camera temperature was increased.

3.5 Heating Beam

The WFD induced in the sample will depend on the absorption coefficient (α) and the parameters of the heating beam such as power, beam size and shape. This section details the characterization of the heating beam.

The heating beam used was from a Tm:fibre-laser developed and assembled by Alexander Hemming of the Defence Science and Technology Group and had a maximum output power of 8 W with a spectrum shown in Figure 3.20 with wavelength centred at 1994 nm. The maximum absorption coefficient due to atmospheric water vapour at wavelengths near this value is about 2 ppm/cm for a relative humidity of 12 % at 23 °C [75] and thus heating of the air by the 1994 nm beam is negligible.

The fibre-laser is pumped by a 793 nm Dilas diode laser. Pump light transmitted through the fibre-laser may be absorbed in the test sample causing additional WFD leading to uncertainty in the calculation of α. However, absorption in Fused Silica (FS) at 793 nm is an order of magnitude less than at 2 µm [43] and thus only pump power of similar magnitude to the heating beam would effect the measurement.

To determine if pump light was present, a shortpass filter was placed in the collimated laser output and a high-sensitivity silicon photodiode was used to measure the transmitted power. No measurable pump light was observed.

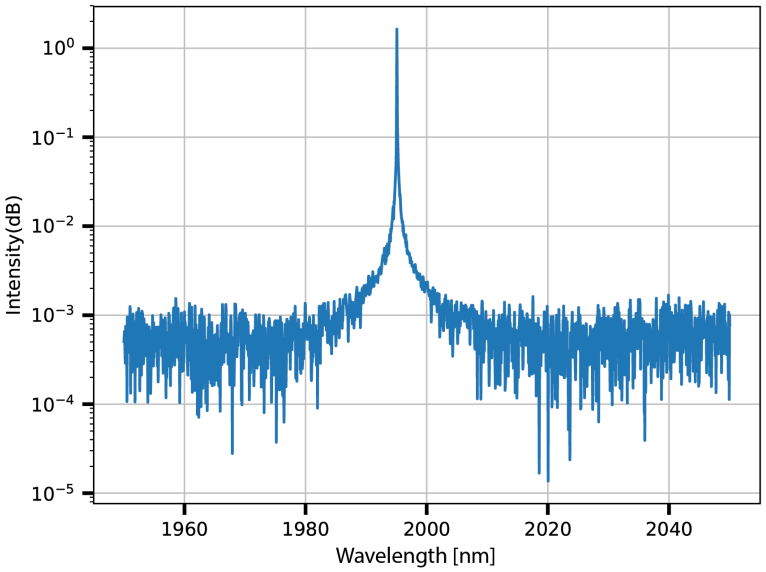

Figure 3.20: Spectrum of 2 µm heating beam.

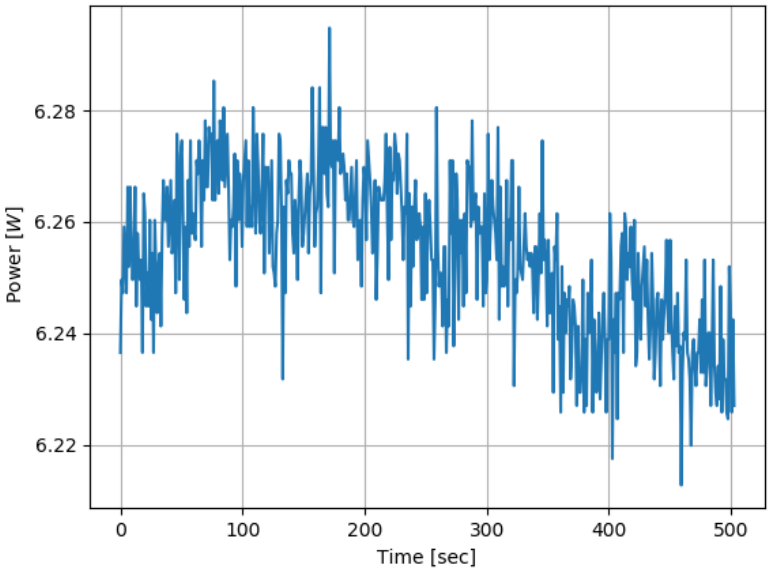

Figure 3.21: Power stability of 2 µm heating beam recorded using thermal power head showing the stability of the heating laser will not affect the measurement.

As shown in Figure 3.21 the power of the 2 µm laser varied over time. Significant power fluctuation during image capture would add to uncertainty in the calculated absorption coefficient hence the stability was compared with the thermal time constant of the test sample. The thermal time constant, τ, of the FS was determined by recording the change in spherical WFD when turning off the heating laser. Figure 3.22 shows the response for a 4 W heating beam and the 3002 FS rod. The data was averaged and compared to a best-fit exponential function (Figure 3.23) to

determine the $1/e$ decay time, giving $\tau = 1.08$ s. However, after the initial warm up period, the power in the heating beam was stable to within about 0.3% for periods > 200 s.

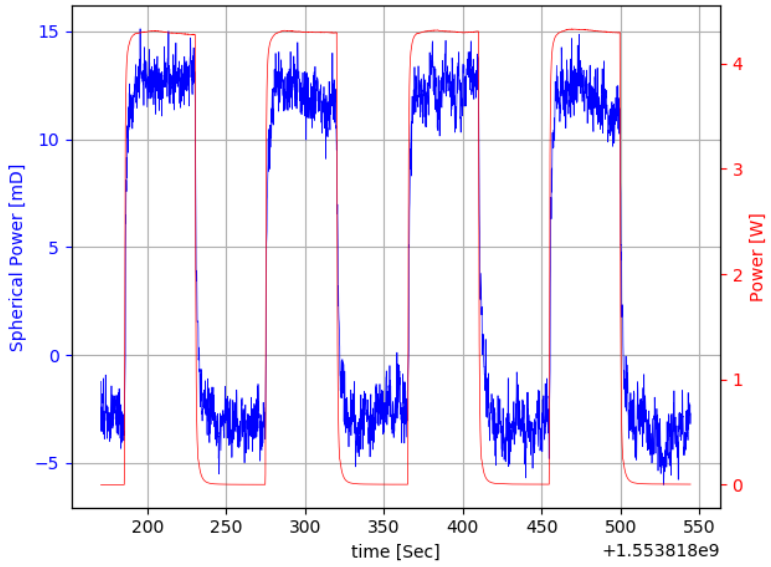

Figure 3.22: Data used to determine the thermal time constant of the 3002 FS rod. The plot shows spherical power response, (blue) and power incident on the front face of the test sample (red).

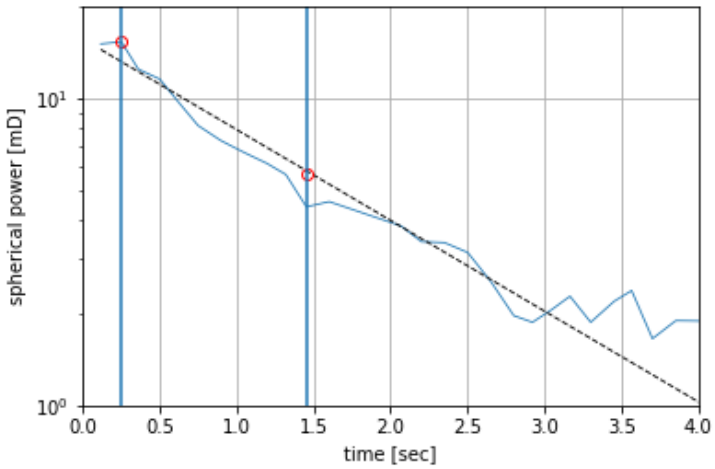

Figure 3.23: Estimating the thermal time constant of the 3002 FS by comparing the data from Figure 3.22 with an exponential decay

The incident power was monitored using an InGaAs PhotoDiode that measured either (a) power from the heating beam transmitted through a steering mirror as shown in Figure 3.1, or (b) scattered from a lens used to collimate the heating beam as shown in Figure 3.24. The detectors were calibrated using the system shown in Figure 3.24, by simultaneously recording the power that would be incident on

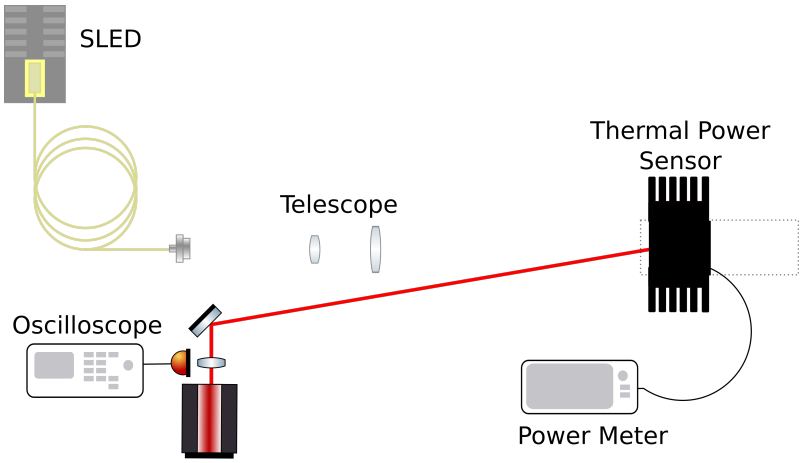

Figure 3.24: Simplified schematic showing experimental setup used to calibrate photodiode for continuous monitoring of power incident on test sample.

the input face of the test sample using a Thorlabs S322C power meter, which has a calibration uncertainty of ±3%, and the output of the PhotoDiode. A typical calibration curve is shown in Figure 3.25.

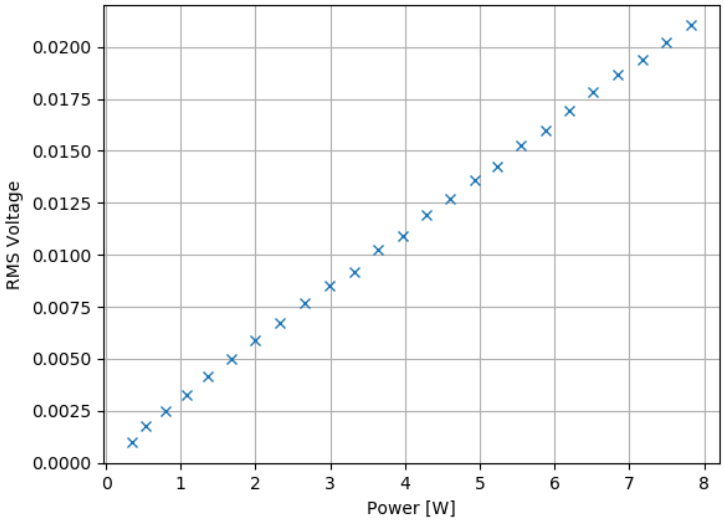

Figure 3.25: Power recoded at input face of test sample used to calibrate Photodiode such that constant monitoring of power was possible.

The size of the heating beam was measured using a thermopile array that had a pixel pitch of 90 µm. Multiple images were taken along the length of the test sample as shown in Figure 3.26 and the $1/e^2$ values were used to determine the beam diameter, giving 0.8 mm. The heating beam is approximately collimated within the

test sample but is slightly astigmatic. The $1/e^2$ diamater varied ± 0.05 mm along the region of interest.

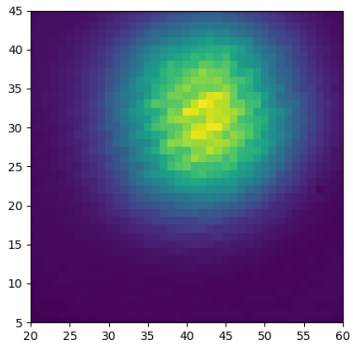

(a) Thermopile image of heating beam

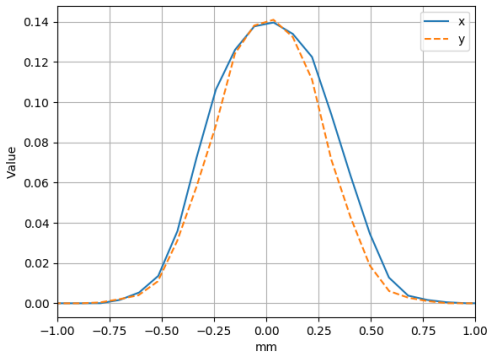

(b) front aperture

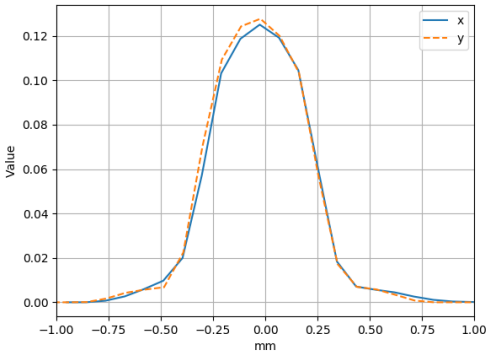

(c) centre of test sample

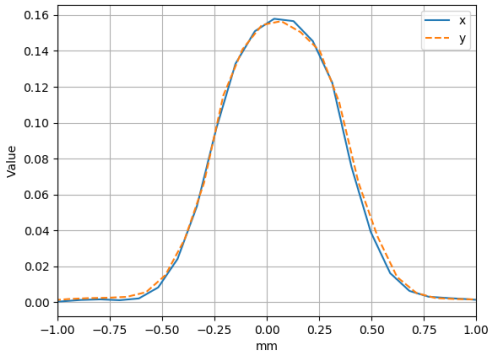

(d) rear aperture

Figure 3.26: Image of heating beam at origin (a) and intensity profiles in x and y along test path. These images were used to determine beam size and collimation of the heating beam.

The heating laser is stable enough to use for shot integration times while the slight astigmatism in the beam shape may lead to issues when calculating the absorption coefficent as discussed in Chapter 5.

3.6 HWS Probe Beam

The probe beam is a integral part of the HWS. Maximizing the sensitivity and accuracy of the measurement process requires that it does not add uncertainty additional to the shot noise discussed in Section 3.4.1. In particular, it must be stable as described below in Sections 3.6.1 and 3.6.2.

Additionally, the probe beam exiting the test sample must be imaged onto the HP as discussed in Section 3.6.3, and be coaxial with the heating beam as discussed in Section 3.6.4

3.6.1 Removing sensitivity to intensity changes

The differential HWS assumes that the intensity of the probe beam at each hole in the HP is constant or changes uniformly. If the intensity distribution changes non uniformly then the centroid of the Hartmann spot would change, implying a change in the wavefront.

Table 3.3: Properties for Thorlabs SLED

Property	Value
Model	Thorlabs SLD830S-A20
Output Power (mW)	22
Centre Wavelength	830 nm
Fibre Size	4.4/125 µm
Coherence Length (FWHM)	13.7 um

Such intensity changes could be created by probe beam jitter if the diameter of the probe beam is too small compared to the HP. Interference fringes due to spurious reflections of the probe beam are particularly problematic as small changes in the path of the probe beam can lead to large changes in the apparent centroid position. The SLD used was a single-mode fibre-coupled to ensure spatial coherence of the wavefront described in Table 3.3. The broad linewidth and short coherence length prevents interference fringes [76] and also reduces the effect of interference between light diffracted by the holes in the HP [64].

3.6.2 Minimising sensitivity to air currents

Air currents in the probe beam path could introduce time varying changes in the spatial coherence of the probe beam and degrade the sensitivity of the HWS.

The effect of air currents was investigated by measured the time evolution of prism and spherical power. A set of reference centroids were recorded and compared with centroids of consecutive single-frame images recorded at one second intervals.

Initially, air currents in the laboratory were reduced by disabling the air conditioner but this resulted in a thermal drift in the HWS signal as the temperature increased. Thus, a perspex enclosure was used to block air currents while minimising the drift in temperature.

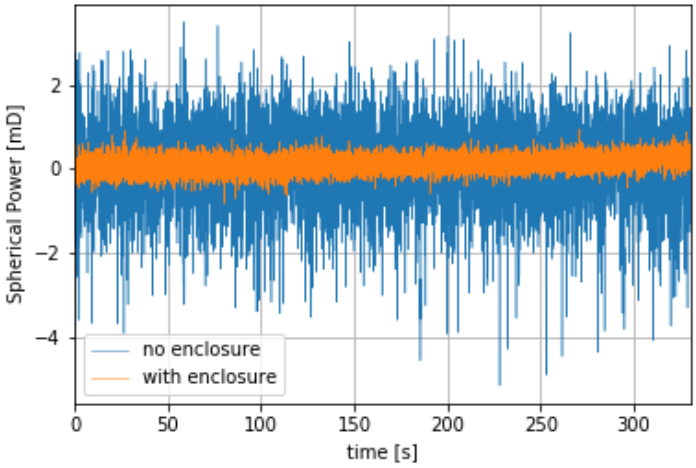

Figure 3.27: Spherical Power from consecutive Hartman images when experimental setup was open to the lab environment (blue) and enclosed (orange) showing an approximately 10x decrease in noise in the system.

The plots in Figures 3.27 and 3.28 show that the enclosure has significantly reduced the effect of the air currents, and reveal an unknown source at about 3 Hz .

3.6.3 Probe beam collimation

The analysis in Section 3.2 assumes that the radius of curvature of the reference wavefront is much larger than the lever arm of the HWS. It is also convenient if the probe beam is approximately collimated as it simplifies the alignment of the measurement system.

Collimation at normal incidence onto the HP was achieved using Delaunay triangulation [77], which finds the triangular meshing of a set of points - spot centroids here - that maximizes the minimum angle of all interior angles in each triangle and thus minimises the circumradius of each triangle. A typical mesh of the central region is shown in Figure 3.29.

The spacing of the imaging telescope lenses and the angular orientation of the CCD relative to the probe beam were adjusted to minimise the average side-length

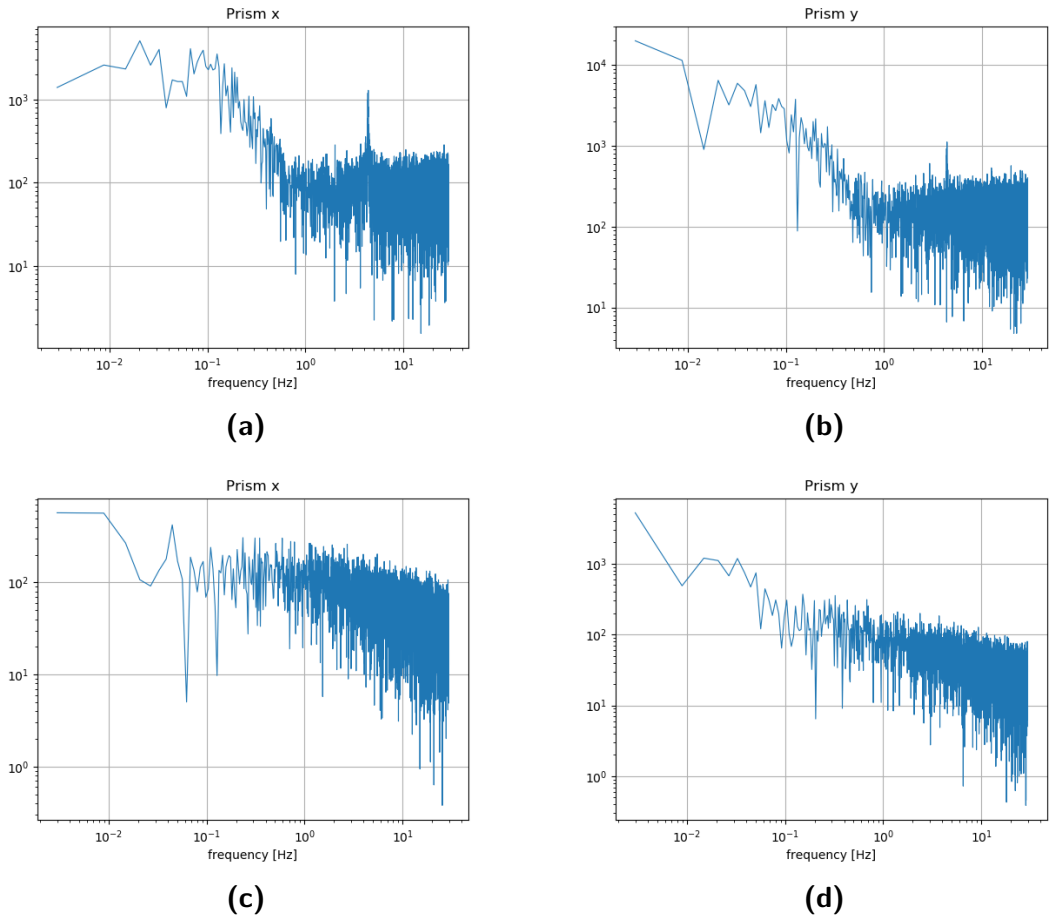

Figure 3.28: Power Spectral Density of prism in x and y showing noise before (a,b) and after enclosing beam path (c,d) to reduce temperature fluctuations and air currents.

of the triangles. A frequency histogram of triangle side-lengths in the central region is plotted in Figure 3.30, for which the mean is 35.841 ± 0.003 pixels $= 430.092 \pm 0.004$ µm. Recall that the nominal pitch of the holes in the HP is 430 µm.

This procedure was also used to confirm the correct spacing between the lenses used to construct the imaging telescope and hence confirm the magnification of the telescope. Accurate knowledge of the magnification is critical for calculating the gradients of the deformed wavefront. By confirming that the Hartmann Rays are perpendicular before and after the input and output lenses respectively, we can ensure that the probe beam is collimated upon exit of the telescope. This procedure minimised the error in the known magnification of the telescope reducing uncertainties when calculating gradients. Using long focal length lenses, 1000mm, in construction of the imaging telescope also reduced errors in magnification.

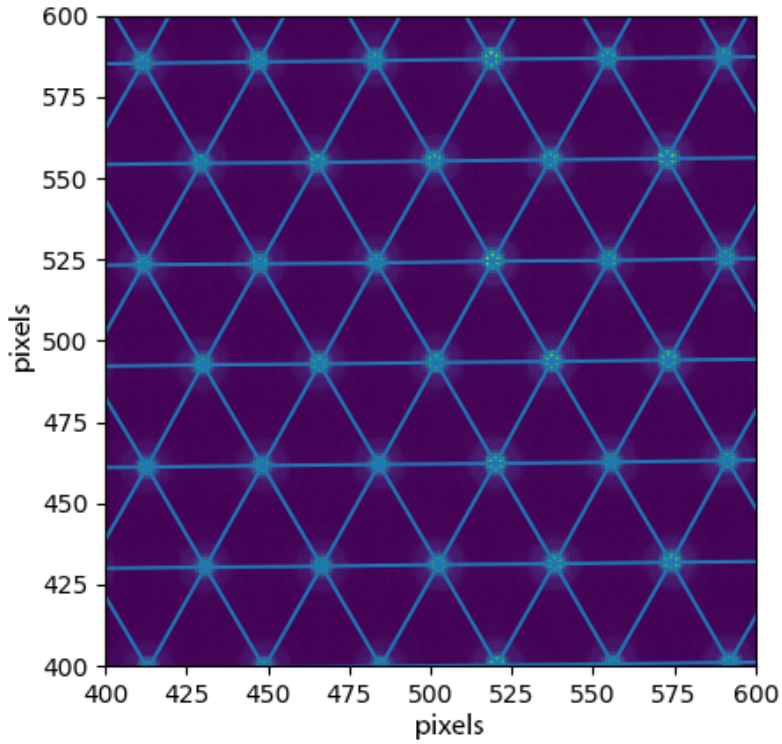

Figure 3.29: By minimising the variation in spacing between simplices centres it can be confirmed that the Hartmann Rays are collimated and hence perpendicular to the CCD.

It is necessary for the probe beam to be perpendicular to the test sample such that the optical path length of the unheated sample matches the physical length. To ensure the probe beam was incident normal to the optic, the centre of mass of the probe beam was calculated from the centroids, and centred on the Hartmann Plate before the test sample was placed into the experimental setup. Once the probe beam was aligned the optic was inserted on the mount and the x y stage was used to realign the probe beam such that the centre of mass was again centred on the sensor.

3.6.4 colinearity of heating and probe beams

The measurement system described in Section 3.1 assumes that the heating and probe beams are colinear. This was achieved by placing apertures at either end of sample, with their centres aligned to the centre or the rod. Each beam was then aligned to the centre of the apertures.

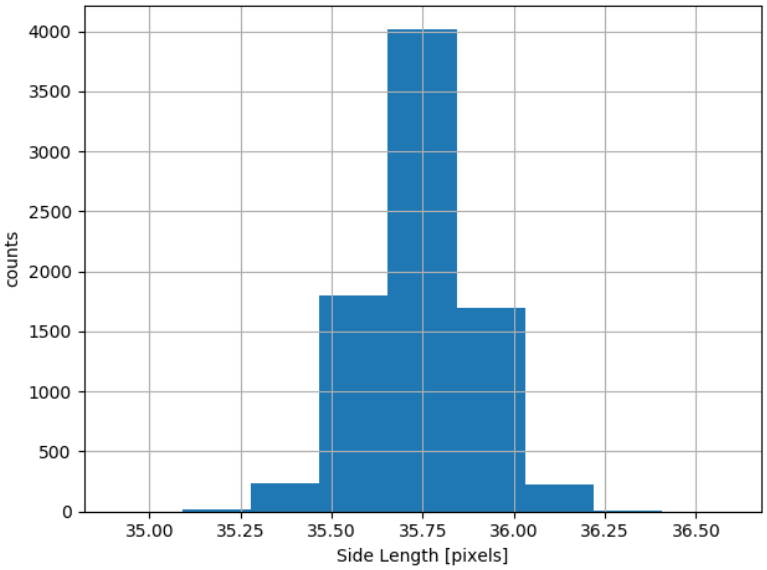

Figure 3.30: Frequency histogram of triangle side lengths determined using Delauny triangulation.

To confirm the alignment, thin highly-absorbing glass slides were positioned at either end of the test bed. Hartmann images were recorded with 8 W of heating beam power. When the heating and probe beams are poorly aligned two heating spots are visible as shown in Figure 3.31. When the beams are aligned the absorption on the two slides overlap and only one heating spot is recorded.

3.7 Absorption in auxiliary optics

Absorption of the 2 µm heating beam in auxiliary optics would result in unwanted WFD, introducing a systematic error into the calculated absorption coefficient.

To determine if absorption in auxiliary optics was significant, Hartmann images were made with 8 W of power injected into the system without the test sample in place. As can be seen in Figure 3.32, approximately 40 nm of WFD was observed, which was expected to be similar to that due to absorption in the 247 mm long test sample.

To determine where in the system the absorption was occurring a third dichroic was placed after the output dichroic (Figure 3.33) and Hartmann images were again recorded. A decrease in WFD would indicate that the heating beam was being transmitted through the dichroic mirrors and being absorbed in the imaging telescope

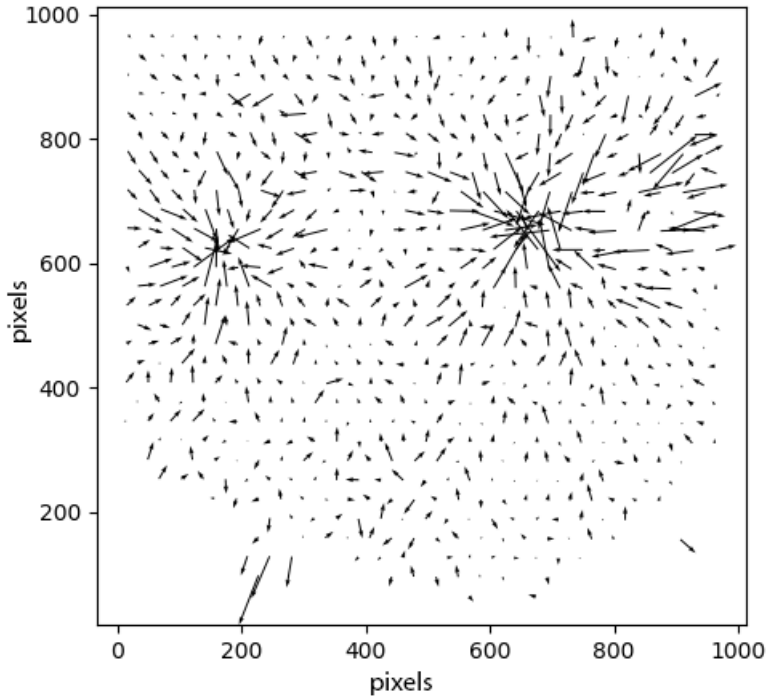

Figure 3.31: A gradient field due to the heating in two thin highly-absorbing glass slides when the probe beam is not colinear with the heating beam.

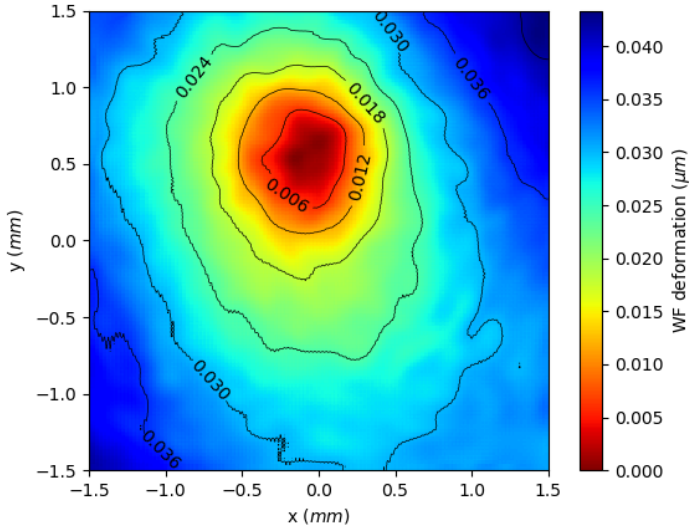

Figure 3.32: WFD recorded with no test sample, showing absorption in auxiliary optics.

or steering mirrors located downstream of the test sample. The resultant images showed the same deformation indicating that transmitted 2 µm laser was minimal

and the WFD was not due to absorption in the downstream optics but absorption in the dichroic mirrors.

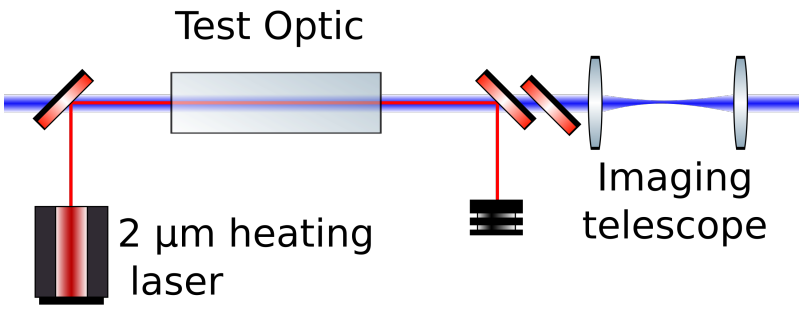

Figure 3.33: A third dichroic was placed between the output dichroic and the beam expanding telescope to investigate if 2 µm light was being absorbed in the optics of the beam expanding telescope and causing unwanted wavefront distortion.

To determine the amount of absorption in the dichroic mirrors the heating beam was adjusted such that it was incident only on the first mirror (Figure 3.34). Hartmann images were taken with 8 W of heating beam power. Figure 3.35 shows the resultant Wave Front Deformation, which is approximately half that shown in Figure 3.32 and thus the distortion was consistent with absorption in the dichroic mirrors.

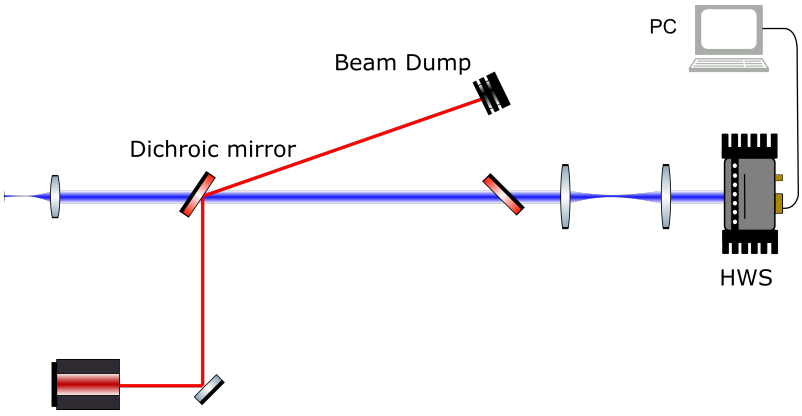

Figure 3.34: The heating beam was misaligned such that it was incident only on the input dichroic to test effect on resulting WFD.

While the amount of absorption in the dichroic mirrors was unexpected, the measurement process described in Section 3.1 could still probably be used but with less accuracy by recording the reference wavefront with the heating beam on but

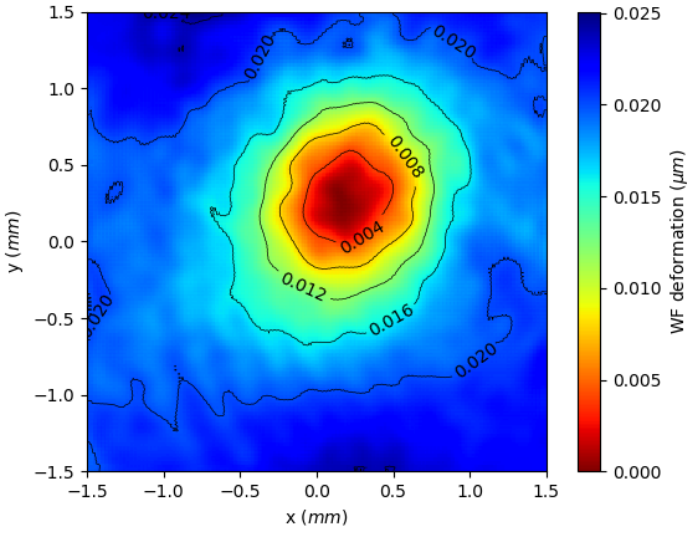

Figure 3.35: Hartmann image taken with 8 W incident power with heating beam misaligned to investigate absorption in a single dichroic mirror.

the test sample removed and then inserting the test sample into the system. This approach assumes, however, that the WFD from the first dichroic is unaffected by the test sample.

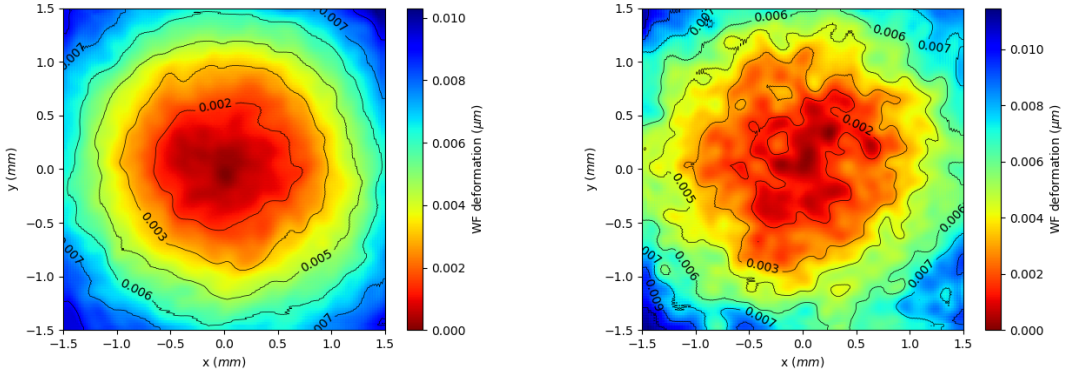

(a) Distortion due to single off-axis dichroic mirror

(b) Distortion due to dichroic mirror with 24 cm test sample in place.

Figure 3.36: Numerical wavefront maps investigating the effect of absorption in (a) the dichroic mirror showing the absorption in a single dichroic mirror without the test sample in place and (b) with the test sample in place (heating beam is not incident on the sample) using experimental setup shown in Figure 3.34 used to investigate the dichroic absorption.

To examine the reproducibility of the probe beam wavefront additional Hartmann images were recorded using the setup shown in Figure 3.34 with the probe beam transmitted through the unheated test sample. The resulting WFD showed

an increased in aberration as shown in Figures 3.36a and 3.36b. The additional aberration could be due to surface roughness or refractive inhomogeneity in the test sample.

To investigate the cause of this aberration we recorded additional Hartmann images separated by 60 seconds and 180 seconds, yielding the wavefront maps shown in Figures 3.37 and 3.38. When comparing Hartman images taken with a smaller separation in time a similar structure was seen. It is apparent from these results that the additional aberrations do not change over short periods but slow drifts in the measurement system result in changes over long periods.

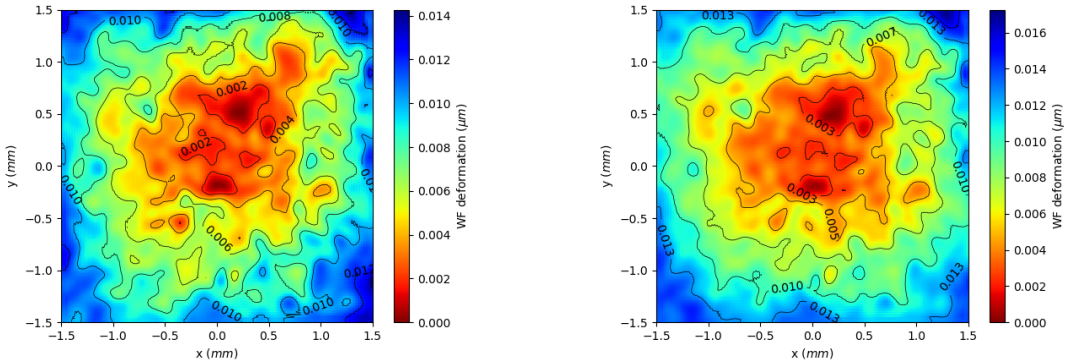

Figure 3.37: Aberration showing similar structure in 24 cm test sample when images were separated in time by 60 seconds.

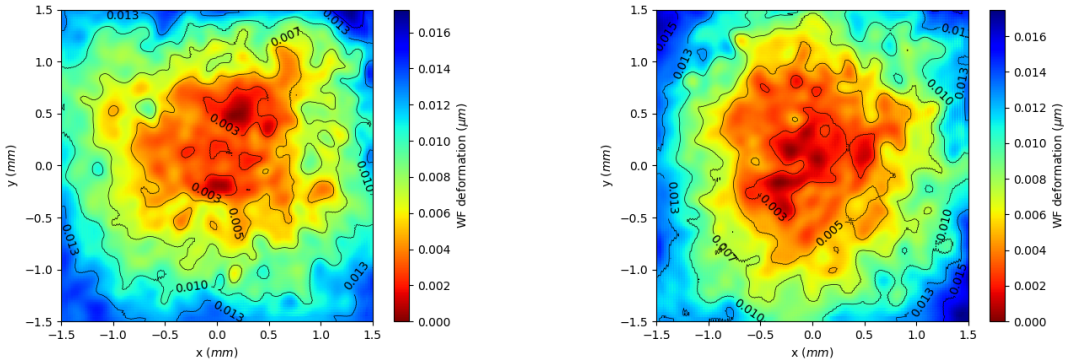

Figure 3.38: Wavefront map showing no matching structure in 24 cm test sample when images were separated by 180 seconds.

In another test Hartmann images were recorded before and after rotating the rod by 5° with a time separation of approximately 60 seconds. As shown in Figure 3.39, the structure of the aberration did not rotate with the test sample, suggesting that the additional is due to inhomogeneity in refractive index within the test sample. Small changes in the input field, due for example to a slight change in the pointing of the probe beam could result in significant speckle like patterns.

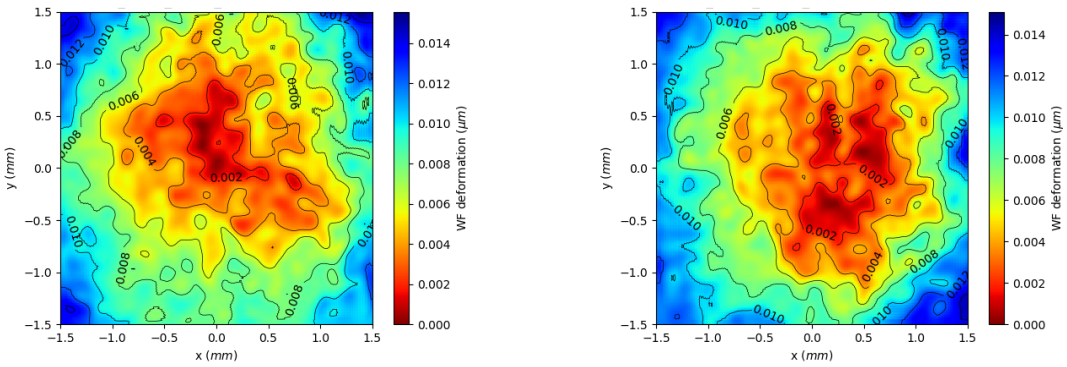

Figure 3.39: WFD maps before and after rotating the test sample by 5° for a time separation of about 60 seconds.

As the absorption in the dichroic mirrors lead to wavefront distortion of similar magnitude to that predicted of the fused silica test sample an alternative method to inject the heating beam into the sample is required.

3.8 Off-Axis Measurement

The measurement system was changed, as shown in Figure 3.40, to use an off-axis heating beam to avoid the issues discussed in the previous section.

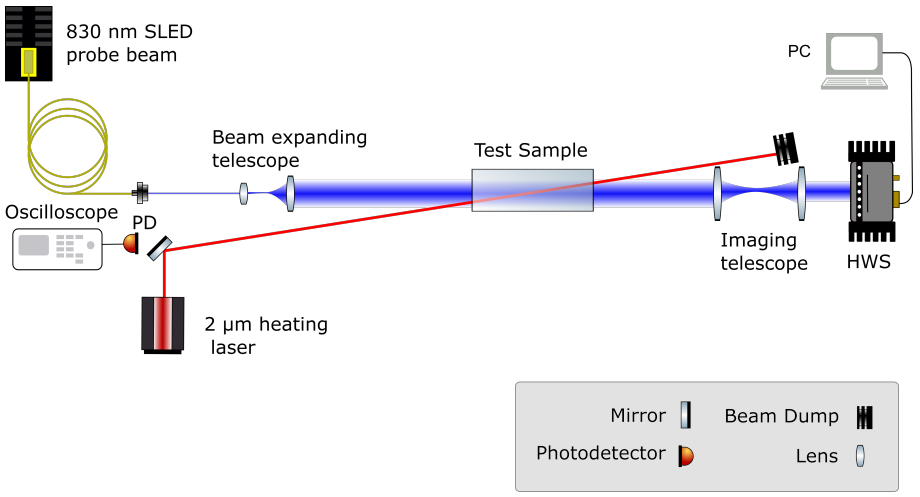

Figure 3.40: Schematic of off-axis photothermal measurement system.

This setup used a 1:1 imaging telescope, to allow for the increased width of the WFD in the horizontal direction. The telescope consisted of two 1000 mm biconvex lenses to ensure imaging condition is met. Long focal length lenses were used to

minimise error in the placement of the lenses which was typically 0.5 mm, and allows a small crossing angle.

3.8.1 Angle of incidence of heating beam

The heating beam is positioned such that it crosses the probe beam in the centre of the test sample as shown in Figure 3.41.

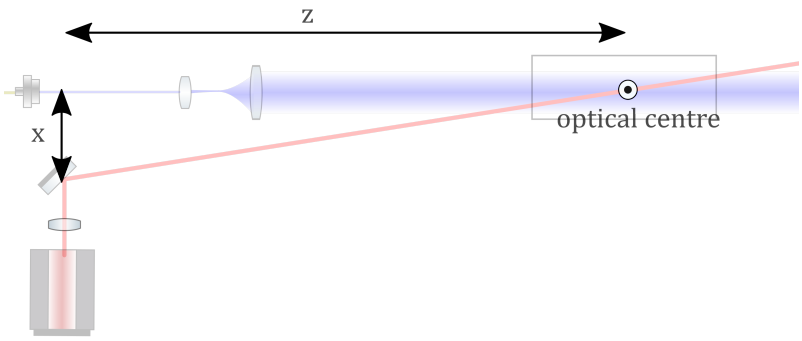

Figure 3.41: To determine the angle of incidence the distance between the probe and heating beams and the distance to the centre of the optic were measured. The Angle Of Incidence, θ_i was determined to be 2.3°.

The angle of incidence, θ_i of the heating beam on the test sample was determined by measuring the distance between the centre of the probe and heating beams at a location near the input steering mirrors (x) and the distance from this point to cross over point of the two beams at the centre of the optic (z), with the test sample removed as shown in Figure 3.41. Thus, $\theta_i = 2.3°$, giving an internal crossing angle of 1.6°.

The maximum uncertainty in θ, $\Delta\theta$, is determined using

$$\tan(\theta + \Delta\theta) = \frac{x + \Delta x}{z - \Delta z} \tag{3.11}$$

For $\Delta x = \Delta z = 0.5$ mm, the corresponding uncertainty in Angle Of Incidence (AOI) was determined to be less than 0.05 degrees.

3.8.2 Improving SNR in WFD maps

The fluctuation in the WFD recorded by the off-axis measurement system were investigated with and without the test optic, using the procedure described in Section 3.4.2. As before, 5000 Hartmann frames were recorded; the first and last 500 frames were used to calculate reference centroids; The remaining 4000 were used to calculate averaged centroids. The resulting $\sigma_{\Delta W}$ as a function of N_{avg} is shown in Figure 3.42.

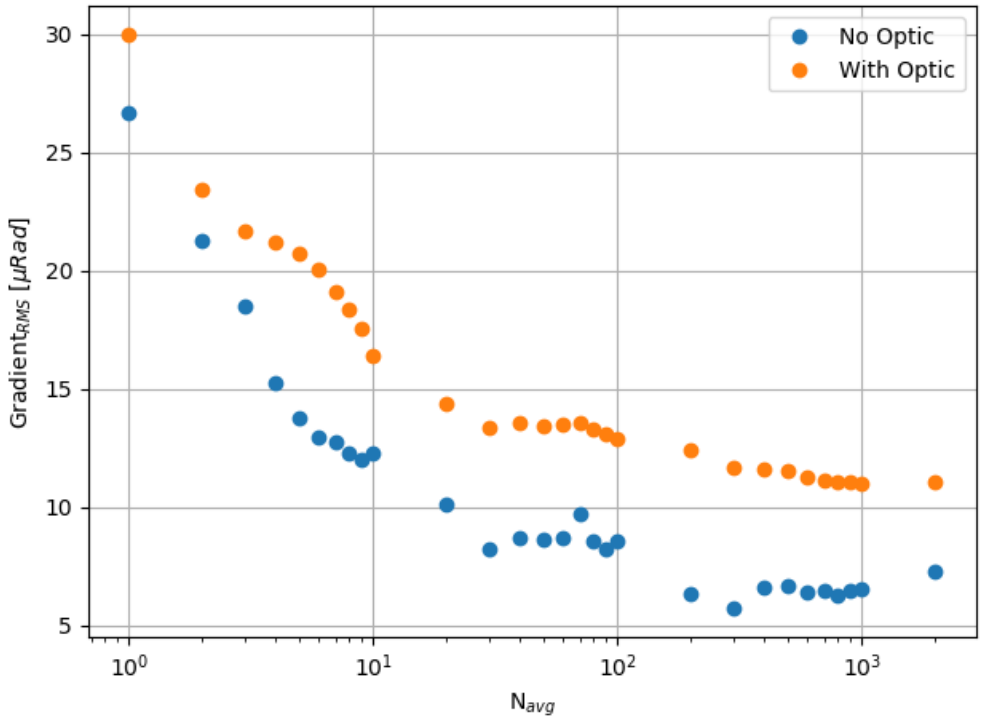

Figure 3.42: RMS Gradient vs number of frames averaged (N_{avg}) with and without test sample in place (no heating beam). For small (<100) frames averaged the noise is reduced as expected. This is not so for $N_{avg} > 100$. The most likely cause of this is fluctuations in heating beam power and environmental noise during image capture.

The noise decreases for $N_{avg} < 100$ if the test sample is removed, as described in Figure 3.16. The reproducibility is degraded by transmitting the probe beam through the unheated test sample however, perhaps due to the refractive index inhomogeneity within the test sample.

Typical WFD, recorded using the off-axis system shown in Figure 3.40, for a 6.4 W heating beam are plotted in Figure 3.43. The maps were generated using $N_{avg} = 100$ reference wavefront and two sets of $N_{avg} = 100$ frames recorded 60 seconds apart after the rod had reached thermal equilibrium. These maps have

significantly larger high-spatial-frequency noise than that for the dichroic (see Figure 3.35), presumably due to the refractive inhomogeneity within the test sample.

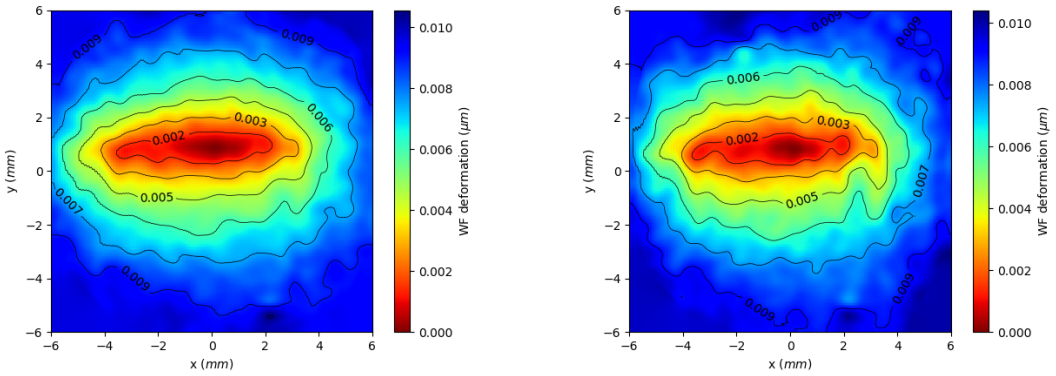

Figure 3.43: Wavefront maps from two Hartmann image where $N_{avg} = 100$ taken 60 seconds apart showing random fluctuation in wavefront deformation.

3.9 Summary

In this chapter we have described a system that uses photothermal distortion of a probe beam to determine the absorption in the test sample. The absorption of the laser wavelength of interest, in this case 2 µm, causes localized heating which results in wavefront distortion which is imaged onto a differential Hartmann Sensor.

The differential HWS uses an opaque plate and a CCD to record the location of spots before and after the heating beam is injected into the test sample. These spots are used to recreate the wavefront distortion of the probe beam. Advantages of this method over previous methods discussed in Section 2.2 include resolution and the ability to image the entire wavefront resolving more information about the test sample.

Unfortunately, the initial coaxial method revealed absorption in the dichroic mirrors of similar magnitude as that predicted for the fused silica test sample and as such an alternative off-axis method was developed. While this simplified the experimental setup, it introduced an elliptical heating profile that results in a greater uncertainty when calculating the absorption coefficient as discussed in the next chapter.

Chapter 4

Quantifying Thermal Absorption

As discussed in previous chapters, we propose to measure the optical absorption in low-OH Fused Silica (FS) using a photothermal approach in which the temperature gradient resulting from absorption causes a change in the wavefront of a probe beam. The absorption is then determined by comparing the measured change with that predicted by a finite element model.

The design of the measurement system was discussed in Chapter 3. Unfortunately, excessive absorption in the dichroic mirrors used to overlap the heating and probe beams necessitated the use of an off-axis system, which significantly complicates the finite element analysis.

In this chapter, we describe the Finite Element Analysis (FEA) model developed to predict the wavefront change expected for a given absorption coefficient. FEA is widely used in physics and engineering to verify designs and model complex systems. The finite element method is an approach to approximate the solutions of partial differential equationss (PDEs) with boundary conditions. It can therefore only be used where the physical properties can be expressed in terms of PDE making it suitable for thermal and optical problems using known PDEs. In this case thermal effects can be described by the following heat-transfer equation [78]

$$\rho\left(T\right) C_p\left(T\right) \frac{\partial T}{\partial t} = \nabla\left[k_{th}\left(T\right) \nabla T\right] + Q \tag{4.1}$$

where $\rho\left(T\right)$ is the material density, $C_p\left(T\right)$ the specific heat capacity, T the temperature, t the time, k_{th} the thermal conductivity, and Q is the heat source due to the absorbed laser power.

The FEA model is defined in Section 4.1. It is validated in Section 4.2 by demonstrating that the wavefront change predicted for a BK7 window using known absorption coefficient agreed with that measured. Section 4.3 discusses in more detail the process of determining the absorption coefficient using FEA before we

present analysis of the sensitivity of the FEA to parameters used in the model in Section 4.4.

The process was validated by demonstrating that the modelled prediction agrees with the observed distortion in a glass for which the absorption coefficient is known and can be measured using traditional techniques. This validation is described in Section 4.2.

In Section 4.4 we perform a sensitivity analysis of the Finite Element Model (FEM) to systematic uncertainties in model parameters such as power and alignment to determine the precision of the measurement system.

4.1 Description of Finite Element Analysis Model

To predict the absorption in the off-axis measurement described in Section 3.8 an FEA model was produced using COMSOL Multiphysics ® [79]. A schematic of the model layout is shown in Figure 4.1.

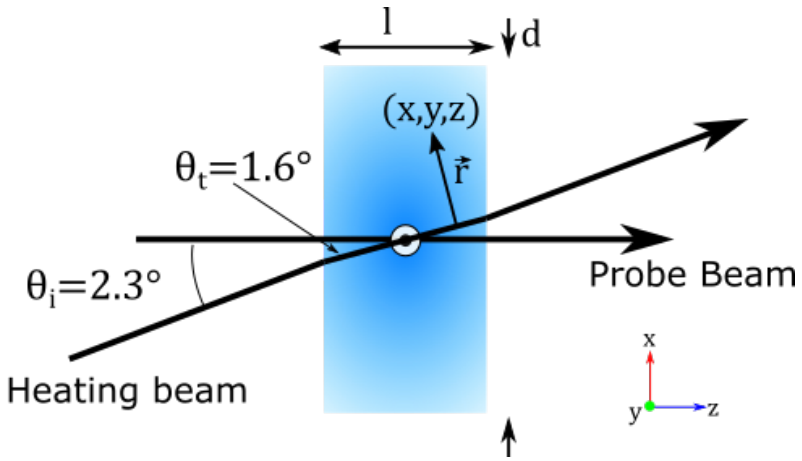

Figure 4.1: Schematic of FEA model where l and d are the thickness and diameter of the test optic respectively. The z-axisis parallel to the cylindrical axis of the test sample and the origin of the (x, y, z) coordinate system is located at the centre of the optic. The internal crossing angle, θ_t, between the heating and probe beams in the optic is 1.6°.

The model assumes that

- The test sample is cylindrical with diameter d and length l.

- The physical parameters of the sample are as shown in Table 4.1.
- The sample is allowed to expand freely and cools radiatively.
- The heating beam is Gaussian and collimated throughout the sample with a radius ω_0.
- The absorption is small and thus the powers, P_1 and P_2 of the heating beam within the sample, as shown in Figure 4.2 are constant (See Appendix A.) and P_1 and P_2 are given by:

$$P_1 \approx \left[\frac{4n}{(n+1)^2}\right] P_0 \text{ and } P_2 \approx \left[\frac{n-1}{n+1}\right]^2 P_1 \tag{4.2}$$

where n is the refractive index of the sample.

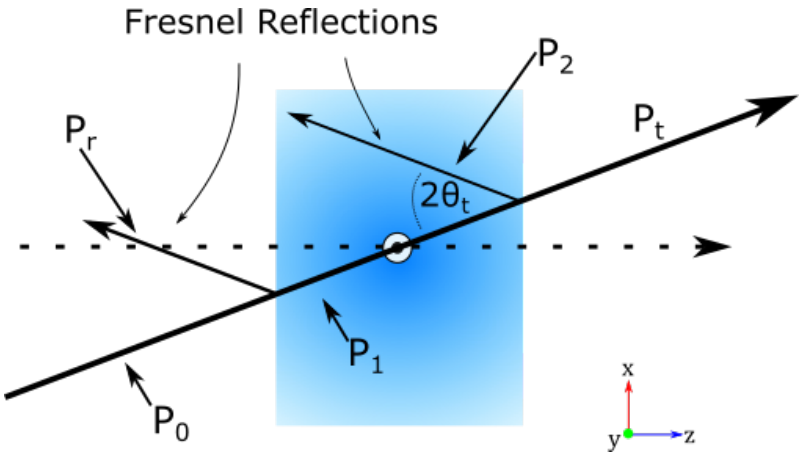

Figure 4.2: Schematic of Fresnel reflection at entrance and exit faces in $(x, 0, z)$ plane.

- The probe beam is not absorbed by the sample.
- The distortion of the probe beam wavefront is small and thus a set of rays propagating parallel to the z axis was used to determine the wavefront distortion. More generally, one should take into account the bending of the rays as they pass through the index gradient using [80].

The absorbed power density $Q(x, y, z)$ is given by:

$$Q(x,y,z) = \frac{2P_1\alpha}{\pi\omega_0^2} \exp\left[\frac{-2r_1^2}{\omega_0^2}\right] + \frac{2P_2\alpha}{\pi\omega_0^2} \exp\left[\frac{-2r_2^2}{\omega_0^2}\right] \tag{4.3}$$

Table 4.1: Parameters used for modelling of FS and BK7

	FS	**BK7**	
Refractive index : n (@1994nm)	1.438834	1.4860	
Coeff. of thermal expansion	0.51e-6	7.1e-6	[1/K]
Heat Capacity (const. Pressure)	964	858	[J/(kg*K)]
thermo-optic parameter (dn/dT)	8.89e-6	1.3e-6	[1/K]
Thermal conductivity	1.38	1.114	[W/(m*K)]
Density	2203	2510	[kg/m^3]
Young's modulus	73.1	82	[GPa]
Poisson's ratio	0.17	0.206	
Emissivity	0.93	0.93	
Radius	40	50.8	[mm]
Length	247	10	[mm]

where P_1 the transmitted power in the optic, P_2 is the Fresnel reflection at the rear surface and α is the absorption coefficient. The radial distances from the heating beam, r_1 and r_2 are given by:

$$r_1 = \sqrt{(x\cos\theta_t - z\sin\theta_t)^2 + y^2} \tag{4.4}$$

$$r_2 = \sqrt{(x\cos\theta_t - (l+z)\sin\theta_t)^2 + y^2} \tag{4.5}$$

as shown in Appendix B.

The heat load deposited in the sample is modelled using the *Heat Transfer in Solids* interface in COMSOL as shown Appendix B. A stationary (steady state) model was used to determine the temperature profile due to the absorbed laser power. The *Solid Mechanics* and *Heat Transfer in Solids* modules are used to calculate the thermal expansion and thermo-optic change due to the heating.

The model was meshed with a variable density mesh, as shown in Figure 4.3, such that the area adjacent to and along the z axis was finely resolved. The cross-sectional area of the finely meshed region was calculated taking into account the heating beam size, angle between the pump and probe beam and the length of the test sample. Typical temperature profiles are shown in Figures 4.4 and 4.5a.

The change in optical path length of a probe ray propagating parallel to the z axis, Δl_{opt}, was determined using [81]

$$\Delta l_{opt}(x,y) = \int_0^l \left[\frac{dn}{dT} + \Delta n(1+\nu)\alpha_{CTE}\right] \Delta T\,(x,y,z)\,dz \tag{4.6}$$

$$= \left[\frac{dn}{dT} + \Delta n\,(1+\nu)\,\alpha_{CTE}\right] \int_0^l \Delta T\,(x,y,z)\,dz \tag{4.7}$$

where dn/dT is the thermo optic coefficient, ν is Poisson's ratio, α_{CTE} is the coefficient of thermal expansion and Δn the change in refractive index between the test sample and the surrounding index, in this case air.

The Wave Front Deformation (WFD) was calculated by examining the variation of Δl_{opt} across the exit face of the test sample.

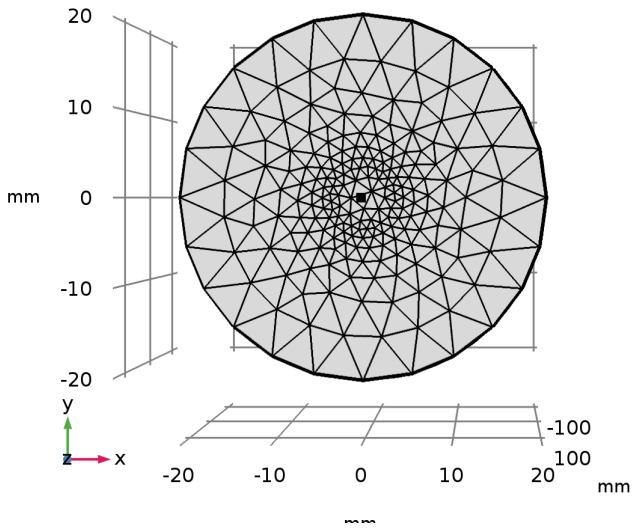

Figure 4.3: COMSOL model of test optic in XY plane showing higher density mesh in the region adjacent to the z axis. This meshing extends along the z axis of the model.

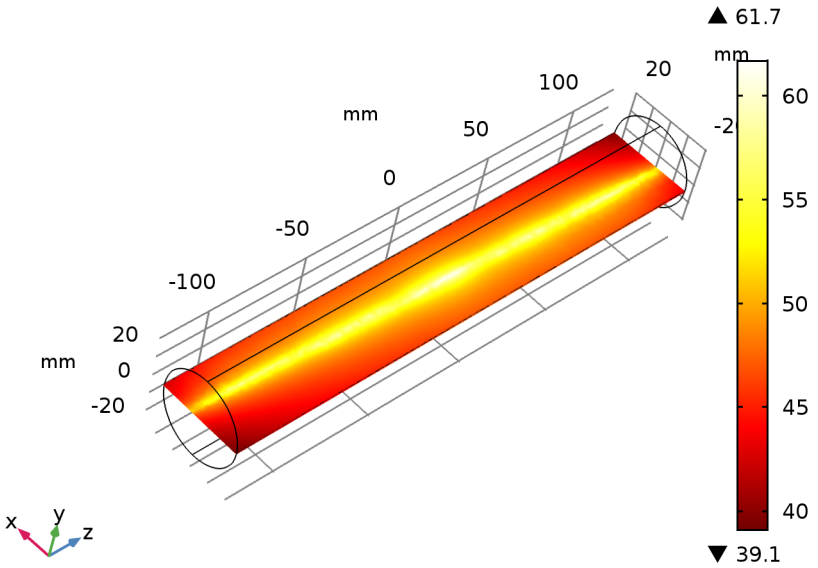

Figure 4.4: Typical temperature increase, in mK, relative to ambient predicted by the Finite Element Analysis model of 24 cm long FS rod with $\alpha = 30$ ppm/cm and $P_0 = 6.5$ W.

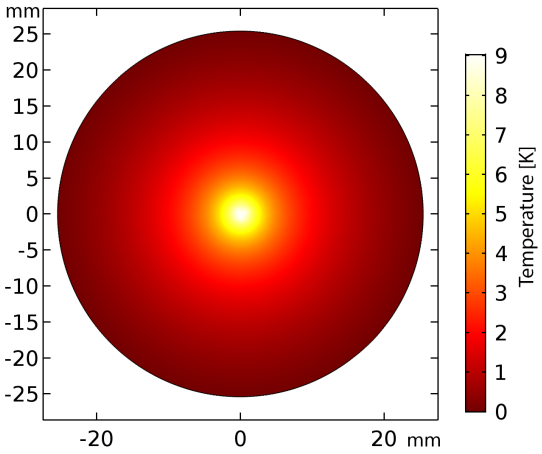

(a)

Figure 4.5: False colour plot at front face of test optic showing temperature rise above ambient [K] for a 10 mm thick BK7 FEA model.

4.2 Validation of FEA model

The FEA model was validated by comparing the measured Wave Front Deformation (WFD) of a borosilicate glass (BK7) cylindrical window that had the properties listed in Table 4.1, with that predicted by the model. The measurement used the

layout shown in Section 3.8, and the FEA prediction assumed $\alpha = 0.04$ cm^{-1}at 2.0 µm [82], $P_0 = 5.2$ W and $\theta_i = 1.6°$.

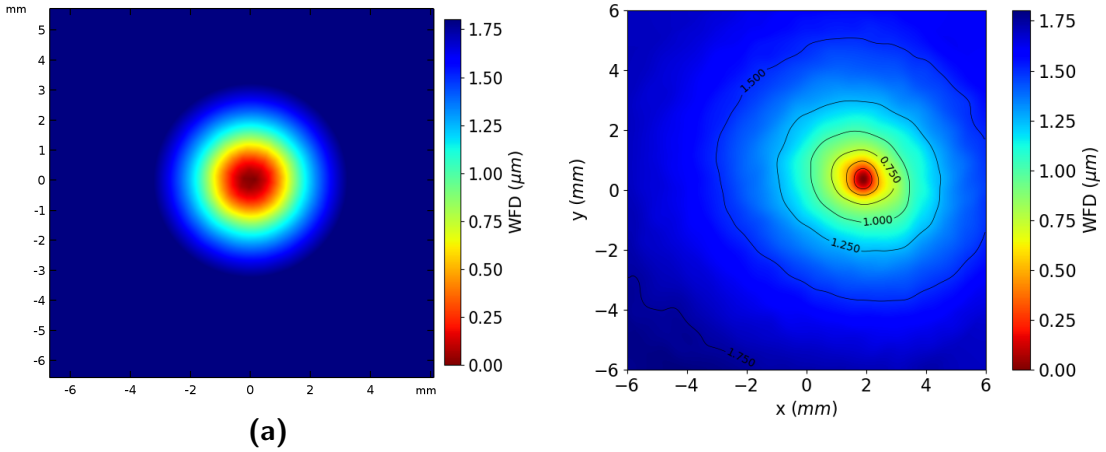

Figure 4.6: False colour plot of (a) front face of test optic showing temperature rise above ambient [K] and (b) Wave Front Deformation for 5.2 W incident on a 10 mm thick BK7 FEA model.

A false-colour plot of the predicted temperature increase at the front face of the BK7 window is shown in Figure 4.5a. This temperature profile is intgrated along the model to determine optical path length and thus determine the predicted Wave Front Deformation of the probe beam. The predicted and measure WFD is shown in Figure 4.6a and section 4.2. The WFD along a typical transect through the peak are plotted in Figure 4.7. Note that the lateral and maximum position WFD of the measured data have been adjusted to approximately overlap the measured curve with that predicted, as the Hartmann Wavefront Sensor (HWS) does not measure the piston WFD.

The agreement between the predicted and measured WFD implies that the FEA model is valid and that the absorption value assumed is appropriate.

4.3 Calculation of absorption coefficient using FEA

The absorption coefficient of the sample is determined by comparing the predicted and measured WFD for various values of absorption coefficient (α). The predicted variation of the WFD with α for the 247 mm long, FS rod and assuming $P_0 = 6.45$ W is plotted in Figure 4.8.

A rise in the average temperature of the test sample above ambient will lead to a DC offset of the wavefront known as piston. The differential HWS does not

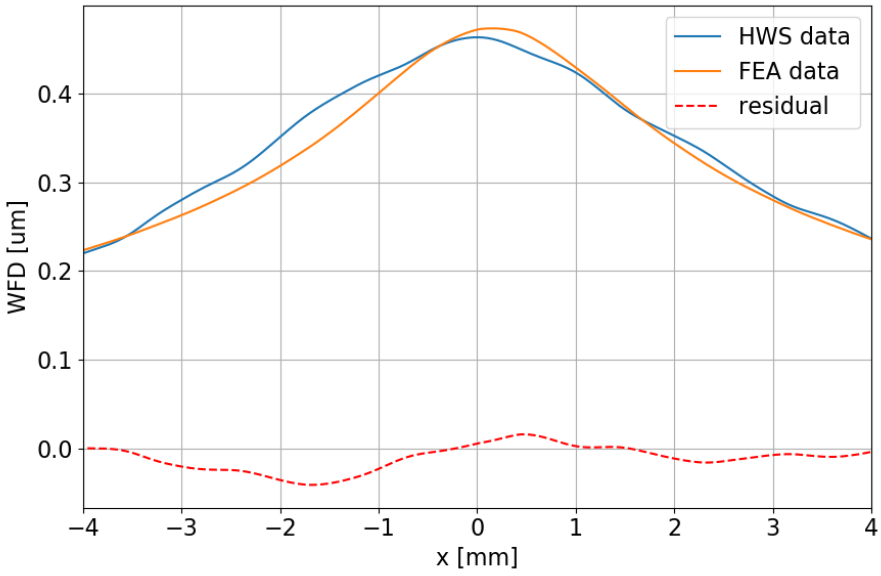

(a)

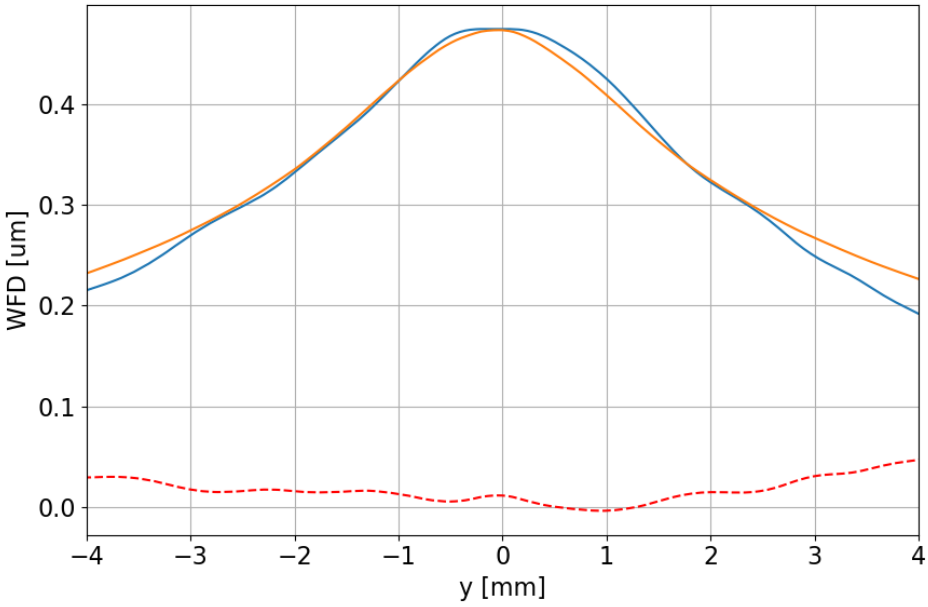

(b)

Figure 4.7: The residuals from the FEA predicted (orange) and measured WFD data (blue) provide and RMS value of less than 0.05 nm indicating the validity of the measurement process.

measure wavefront piston, and as such the comparison is achieved by matching the maximum values of the predicted WFD as shown in Figure 4.9 and minimising the RMS difference. The absorption coefficient can thus be determined by comparing the prediction with the measured WFD.

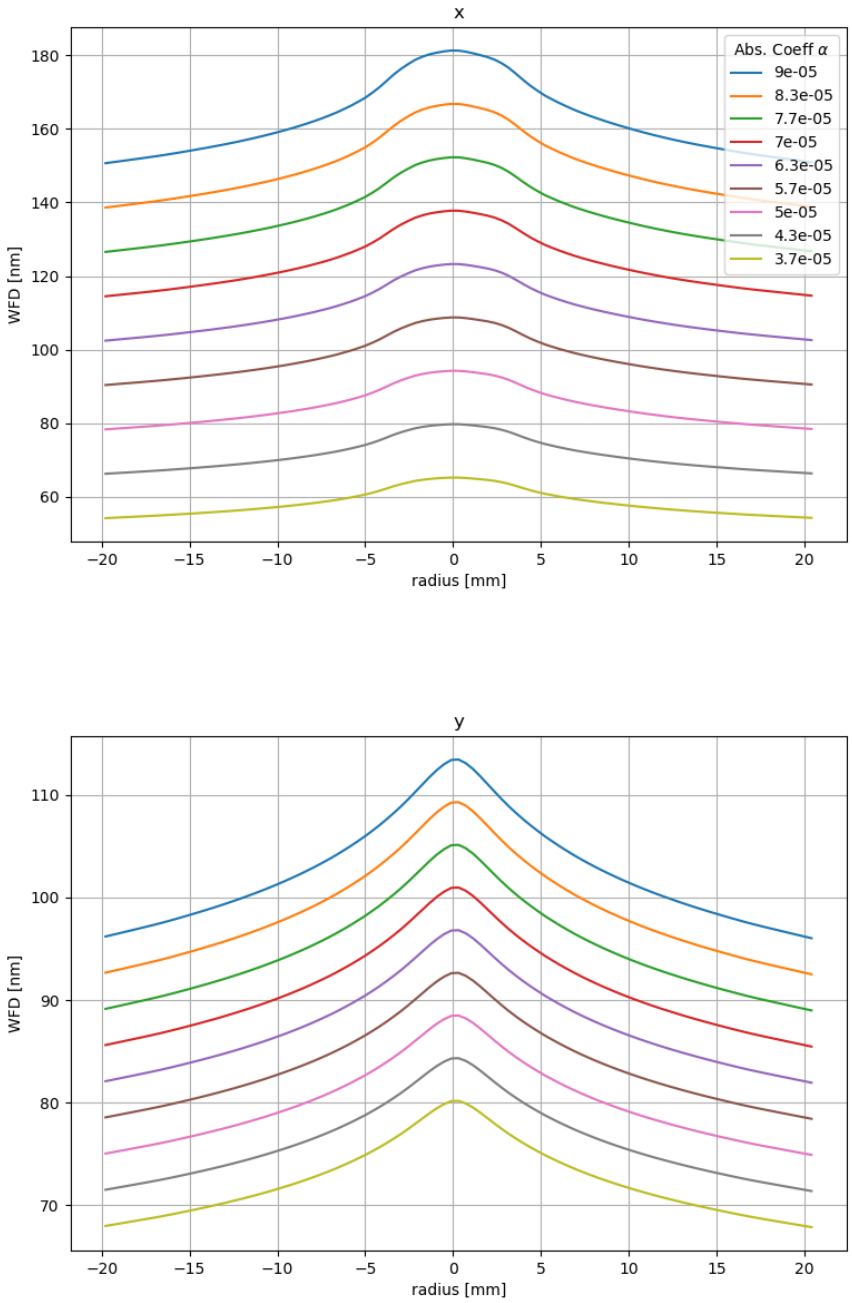

Figure 4.8: Predicted WFD from FEA for the FS 3002 rod and different value absorption coefficients, including piston due to the increase in temperature above ambient.

Note, however, that Equation (4.3) shows that the predicted WFD depends only on αP_0. Thus, the accuracy of α estimated from the model will be affected by systematic uncertainty in the power meter, which is 3% here.

The shape of the predicted WFD also depends on the system parameters assumed in the FEA. This sensitivity of the predicted WFD is discussed in following section.

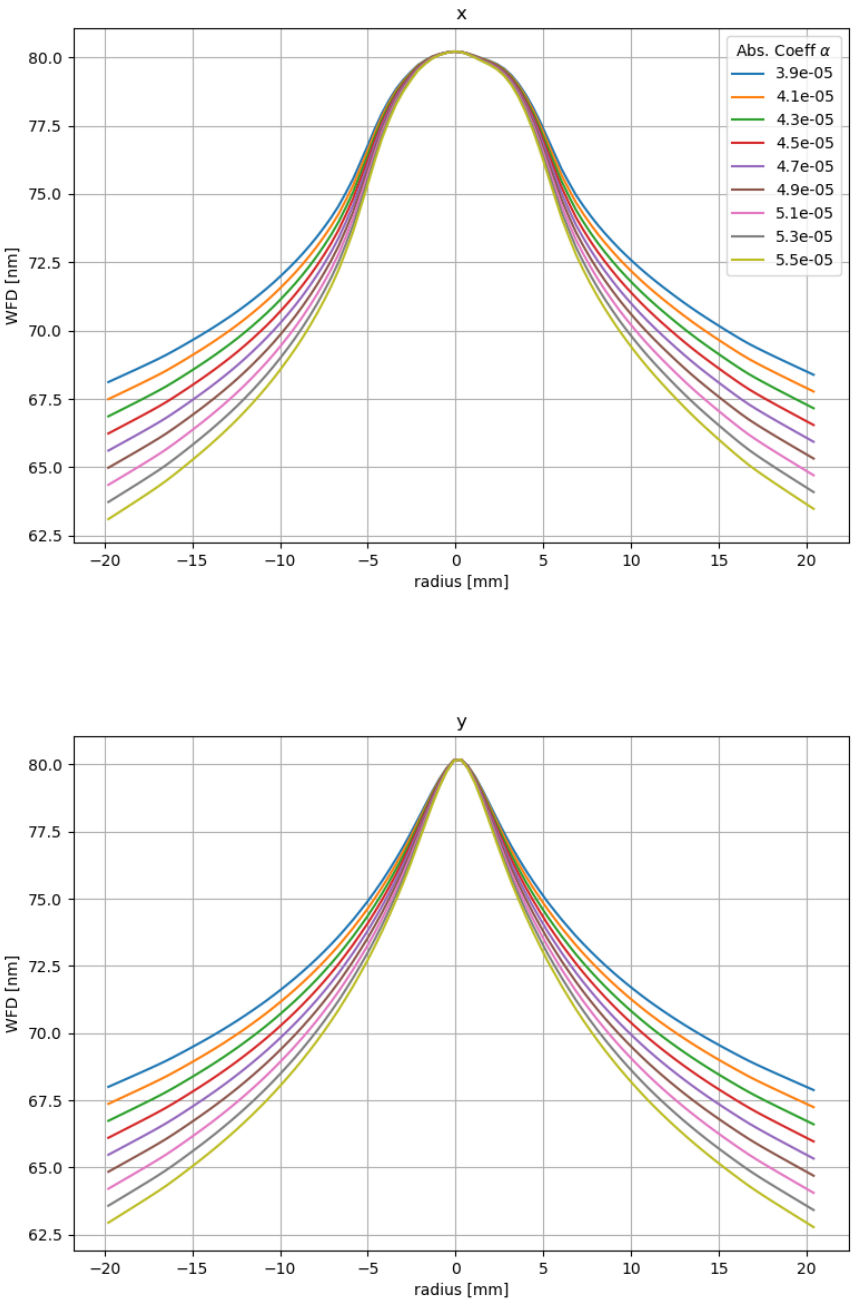

Figure 4.9: Wave front deformation for the FS 3002 rod with maximum WFD values matched.

4.4 Sensitivity analysis for FEA model

The sensitivity of the FEA model to the input parameters was investigated by examining the change in predicted WFD while varying the parameter under investigation and holding other parameters constant. This analysis was done for the 247 mm long, low-hydroxyl (OH) FS rod used in Chapter 5.

4.4.1 Angle between heating and probe beams

As discussed in Section 3.8.1, the angle between the heating and probe beams, θ_i, was determined by measuring the distance between the centres of the probe and heating beams and the distance to their crossover point at the centre of the optic. The uncertainty in θ_i was determined to be less than 0.05 degrees using Equation (3.11).

The effect of a change in θ_i on the predicted WFD for $P_0 = 6.45$ W is plotted in Figure 4.10. The WFD near the edge of the probe beam would change by less than 0.1 nm for a change in angle of incidence of 0.05 degrees, the estimated uncertainty in θ_i.

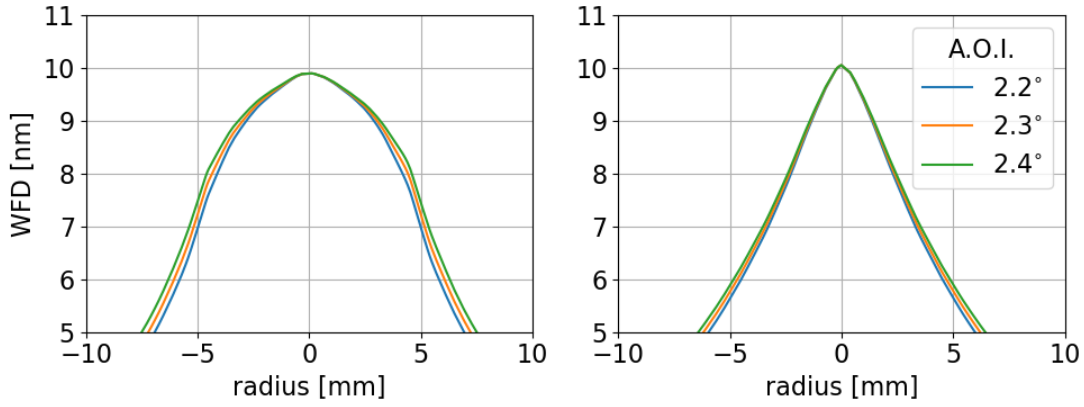

Figure 4.10: Predicted change in WFD near $\theta_i = 2.3°$.

4.4.2 Heating Beam Size

As discussed in Section 3.5, the $1/e^2$ diameter of the heating beam was 0.8±0.05 mm. The dependence of WFD on beam size is shown in Figure 4.11.

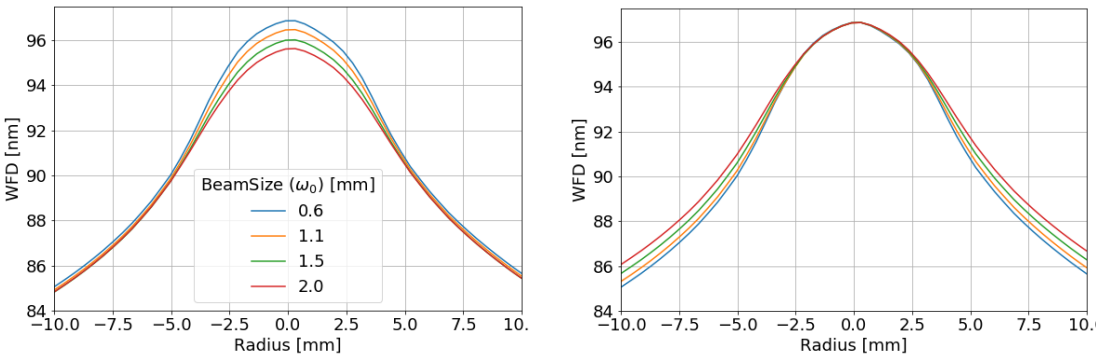

Figure 4.11: Change in predicted WFD due to heating beam size (a) including piston (b) and with matched maximum values.

4.4.3 Sensitivity to length

The length of the optic was measured using a Vernier Calipers with a stated accuracy of 0.07 mm. As can be seen in Figure 4.12 small variations in length does not couple strongly into WFD for weakly absorbing materials. For $\Delta l = 0.1$ mm the uncertainty in WFD is $\pm$ 0.05 nm and hence error in length measurement can be ignored when calculating uncertainty in the calculated absorption coefficient.

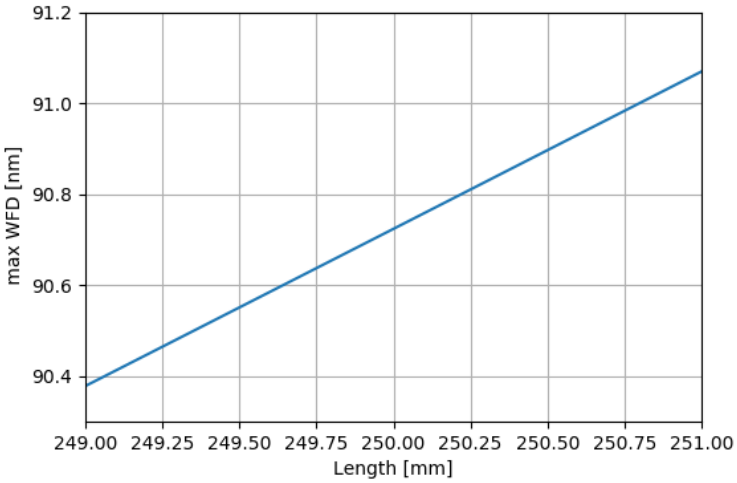

Figure 4.12: Predicted maximum value of WFD as a function of length of the FS rod.

4.4.4 Summary

This chapter described a FEA model that can be used to determine α of the test sample by comparing the predicted WFD with that measured. It was validated by showing that the predicted and measured WFD for a BK7 window were the same.

The sensitivity of the predicted WFD to uncertainties in the angle between the heating and probe beams, heating beam size and length of the FS 3002 rod is 2 nm at the edges of the predicted WFD and are thus negligible.

However, the comparison yields only the αP product and so the accuracy of the estimate value of α is the same as that of the power measurement, which is 3% here.

Additionally, since the WFD in FS is dominated by the thermo-optic effect, the estimated value of α also relies on an accurate value for the thermo-optic coefficient.

Chapter 5

Results

The off-axis photothermal measurement system discussed in Chapter 3 and the Finite Element Analysis (FEA) discussed in Chapter 4 were used to determine the absorption coefficient of the Heraeus 3002 Fused Silica (FS) rod detailed in Table 4.1.

The data in Figure 3.39 shows that while refractive index inhomogeneity within the FS rod introduces speckle-like noise into the transmitted wavefront, its effect can be reduced by averaging. The development of a sampling scheme to effect thus reduction for absorption-induced wavefront change is described in Section 5.1. The scheme used to collect the final data is described in Section 5.2, and the data analysis to determine the absorption coefficient is described in Section 5.3. The chapter concludes with a discussion of the results.

5.1 Reducing noise in HWS measurement

The measured Wave Front Deformation (WFD) for a heating power of 6.45 W with a 100 frame average ($N_{avg} = 100$) for each of the reference and 'live' wavefronts is plotted in Figure 5.1. The noise evident in this map is due to refractive index inhomogeneity within the FS rod as discussed in Chapter 3.

To confirm that the WFD data can be further averaged to reduce the effect of random noise as suggested by Figure 3.39 600 sets of $N_{avg} = 100$ were recorded as described below:

- Record reference frame with $N_{avg} = 100$.
- Turn on heating beam allowing for system to come into thermal equilibrium.
- Record live frame with $N_{avg} = 100$.
- Record voltage from power-monitor photodiode.

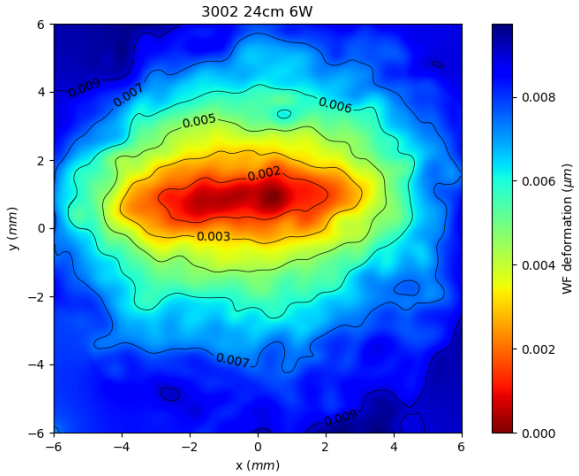

Figure 5.1: Single Hartmann image showing wavefront deformation from 6.45 W where $N_{avg} = 100$.

- Turn off heating laser.
- Calculate gradient map and remove global prism.

The RMS average of each gradient field, normalised by the incident power in that map, is plotted as a frequency histogram in Figure 5.2

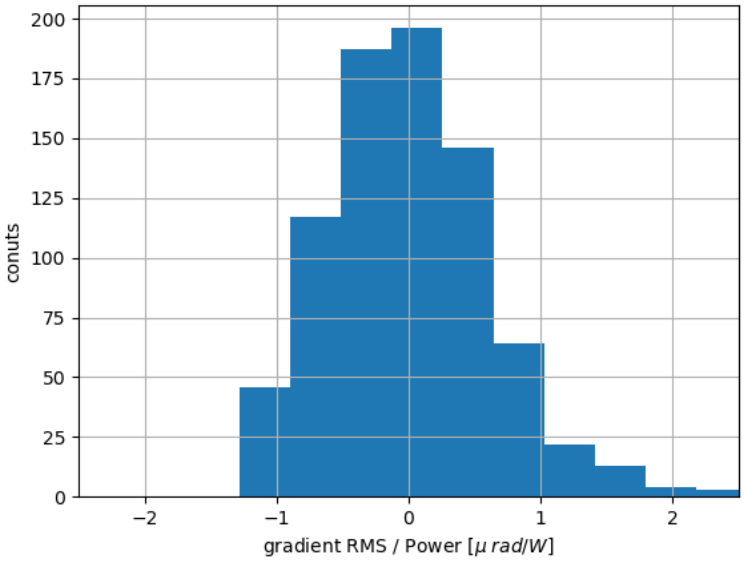

Figure 5.2: Histogram of variation in RMS Gradient normalised by the power in the heating beam.

The distribution appears to be largely normally distributed but has a slight asymmetry perhaps due to the increase in temperature of the Hartmann Wavefront Sensor (HWS) due to the large number of consecutive frames recorded.

To test this another set of Hartmann images was recorded as above while recording camera temperature. A scatter plot of the normalized RMS of the gradient field vs the camera temperature is plotted in Figure 5.3, showing a correlation. The recording scheme for the data used to calculate the absorption coefficient was thus modified.

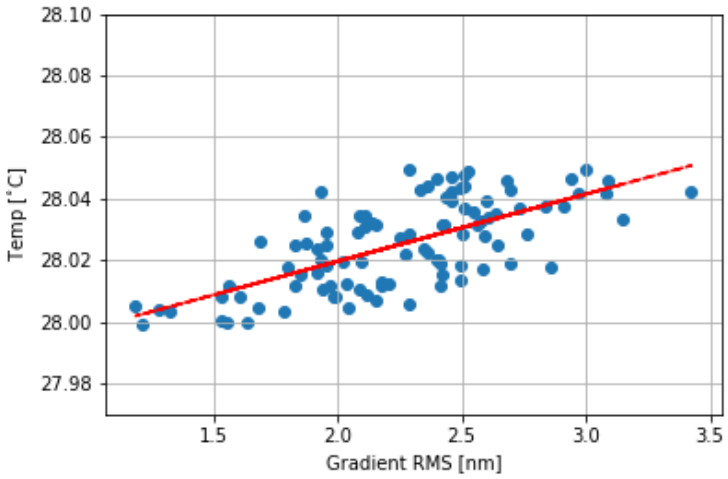

Figure 5.3: RMS gradient normailised by incident power as a function of temperature.

5.2 Averaging of HWS images

The procedure to generate the averaged frames for final calculation of the absorption coefficient was as follows:

- Record reference frame with $N_{avg} = 100$.
- Turn on heating beam allowing for system to come into thermal equilibrium.
- Record voltage from power-monitor photodiode.
- Record live frame with $N_{avg} = 100$.
- Record voltage from photodiode.

- Turn off heating laser
- Calculate average voltage and determine incident power.
- Calculate gradient map and remove global prism.

This procedure was repeated five times with a delay of 30 seconds between each Hartmann image to allow for the system to cool. The average of the resultant gradient map was calculated and used to determine the numerical wavefront as shown in Figure 5.4.

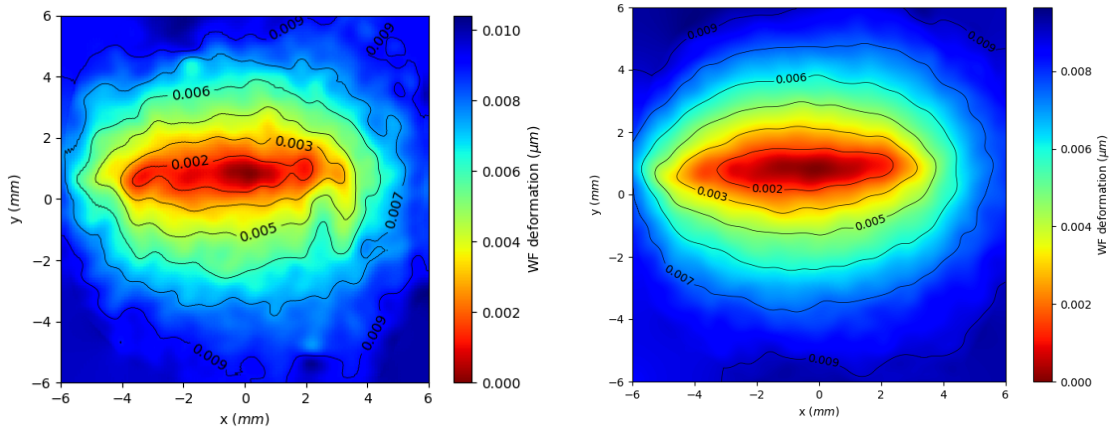

Figure 5.4: Single wavefront map (a) where $N_{avg} = 100$ for both reference and live images showing aberation in wavefront and averaged wavefront map (b) created from five gradient maps of separate Hartmann images each $N_{avg} = 100$.

An overlay of the WFD and the centroid locations is shown in Figure 5.5.

5.3 Absorption Coefficient in FS

The optimum value of absorption coefficient (α) was calculated using the following process:

1. Calculate predicted WFD in x and y directions, $\mathrm{WFD_x}$ and $\mathrm{WFD_y}$, for an initial set of α values.
2. Calculate RMS of difference between the predicted and measured WFD.

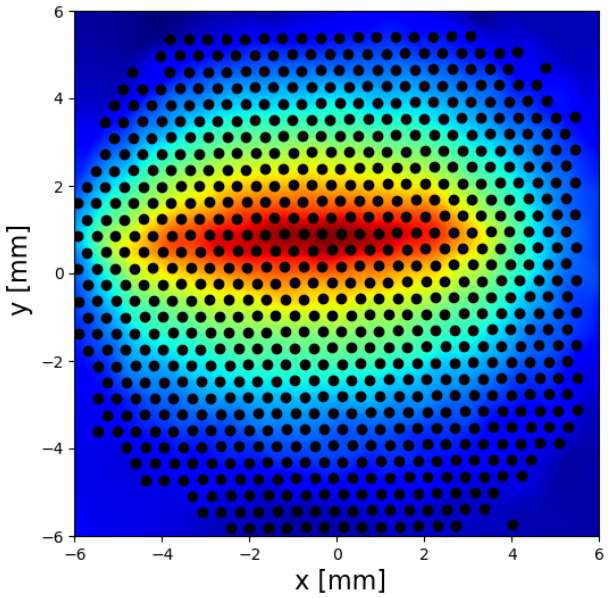

Figure 5.5: Numerical wavefront and location of centroids used to determine wavefront deformation showing reduced number of spots in region if interest for y versus X profile.

3. Adjust lateral postion and peak value of measured WFD to minimise RMS difference for each α.

4. Identify optimum α_x and α_y values.

5. Calculate predicted $\mathrm{WFD_x}$ and $\mathrm{WFD_y}$ for finer grid of α values around optimum values from step 4.

6. Repeat steps 2 to 5 several times to better resolve absorption coefficient.

The RMS difference as a function of α is plotted in Figure 5.6. The estimated absorption coefficient is thus:

$$\alpha_{semi-major(x)} = 43.5 \pm 0.5\mathrm{ppm/cm} \pm 3\%$$

$$\alpha_{semi-major(y)} = 46.5 \pm 0.5\mathrm{ppm/cm} \pm 3\%$$

The predicted and measured $\mathrm{WFD_x}$ and $\mathrm{WFD_y}$ for the optimum α values are plotted in Figures 5.7 and 5.8 respectively.

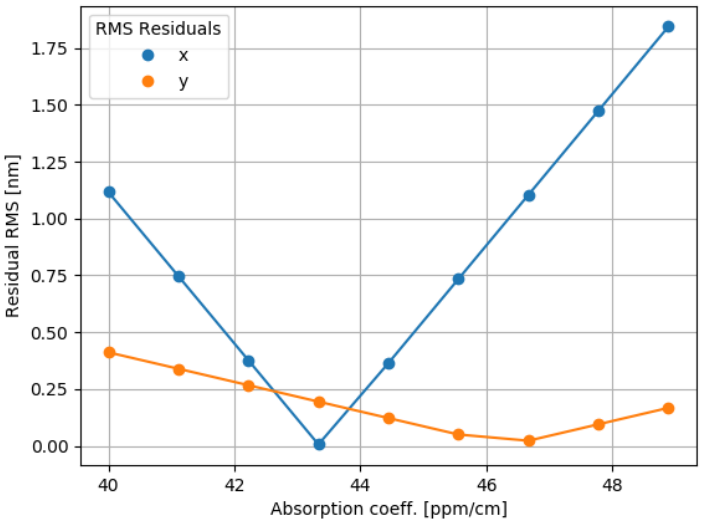

Figure 5.6: RMS difference as a function of absorption coefficient used to optimise calculation of α.

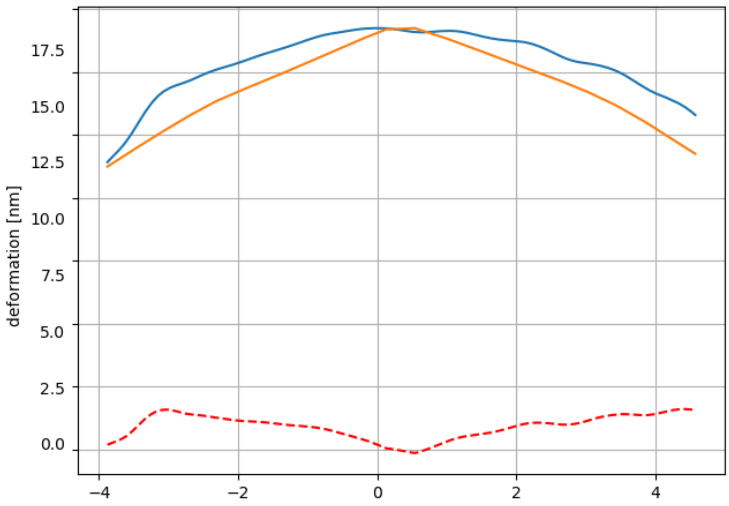

Figure 5.7: Wavefront slice in horizontal profile, x, (blue) matched to predicted FEA profile (orange) and residual (dashed).

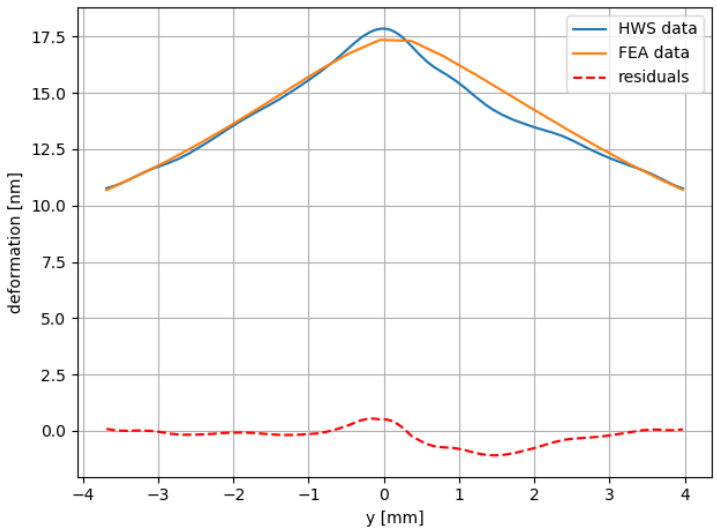

Figure 5.8: Wavefront slice in vertical profile, y, (blue) matched to predicted FEA profile (orange) and residual (dashed).

5.4 Discussion

The profiles in x and y were analysed independently due to the apparent mismatch, which may in part be due to a slight astigmatism in the heating beam.

The heating beam was initially collimated using a f = 15 mm BK7 lens. Beam profiles taken along the heating beam path revealed structure in the heating beam that might affect the temperature profile in the test sample. Calcium fluoride and Infrasil[1] lenses were also tested and all showed structure as seen in Figure 5.9. Images were also taken with no collimating lens in place, diverging from the fibre, and no structure was seen. Hence, the structure, assumed to be interference be caused by reflections from internal surfaces of the collimating lens. The lenses used were AR 'D' type lenses which have approximately 1% reflection at 2 µm. To minimise distortion due to structure in the beam the heating laser was focused at the centre of the optic.

The test sample was removed and the $1/e^2$ value was calculated for the heating beam. This was measured at the input and exit faces and the centre of the 24 cm sample. Figure 5.10 shows the ellipticity of the heating beam as to propagates along the test optic. This astigmatism is partialy the cause of the mismatch in x and y profiles.

[1]Infrasil is a high quality quartz glass manufactured by fusion of natural quartz as opposed to FS.

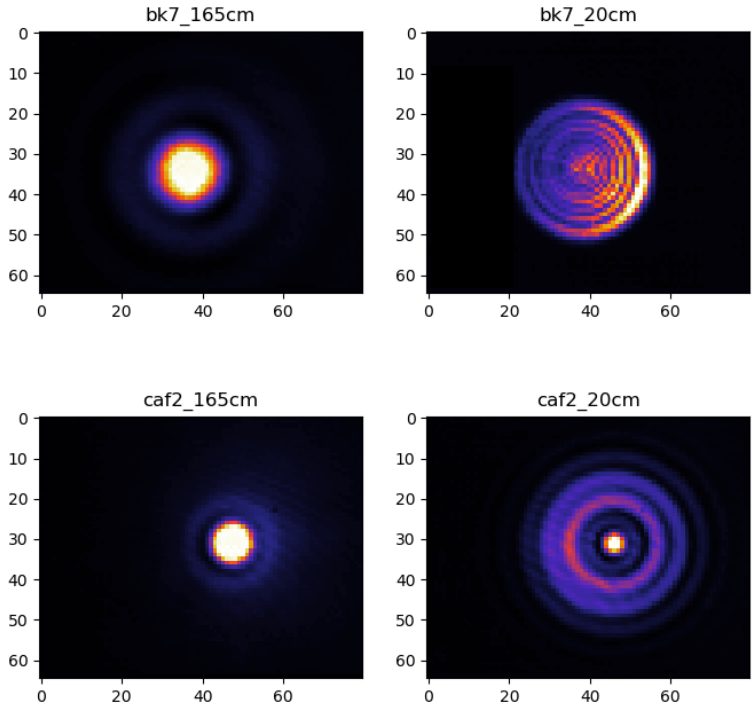

Figure 5.9: Heating beam focused to a spot (left) and in the near field (right) showing structure in the beam

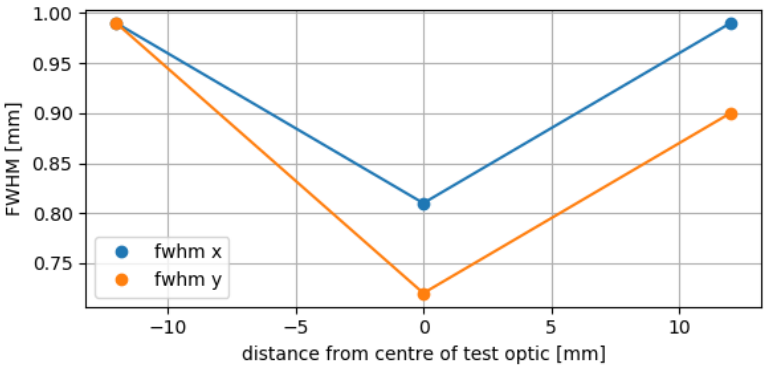

Figure 5.10: FWHM of heating beam profile along the test optic. Astigmatism leads to a mismatch in heating profiles.

Table 5.1: Power and absorption comparison for current aLIGO detector (1064 nm science beam) and proposed next generation Gravitational-Wave detectors operating at $2\,\mu\mathrm{m}$ assuming a 6 cm thick beamsplitter.

	Arm Cavity Power	PRC Power	Abs. Power in BS
aLIGO (O3)	200 kW	1.6 kW	0.3 W
aLIGO (design)	750 kW	6 kW	1.1 W
Voyager	3 MW	2.82 kW	0.61 W
OzHF	5 MW	27 kW	5.8 W

The heating beam is refracted due to the difference in angle of incidence in x and y planes causing elongation in the x axis. The resulting astigmatism is less than 0.01% and hence does not lead to a significant elipicity of the heating beam and thus can be ignored.

With the determined value of α for 3002 FS of 45 ppm/cm fused silica appears to be a possible choice for axillary optics such as the beamsplitter in current Voyager design as shown in Section 5.4 although other materials with a heavier molecular mass, such as fluoride, should be considered. For other designs such as OzHF FS absorption may be a problem due to the higher finesse Power Recycling Cavity resulting in higher recirculating power and additional absorption when compared with thhe Voyager design.

The differential measurement approach used and the small WFD means that imperfections in the alignment of the lenses in the imaging telescope and their separation (from the image relay condition) are common mode and so should not significantly affect the result.

Chapter 6

Conclusion

6.1 Summary

This thesis describes the development of a system to measure optical absorption in weakly absorbing material, and its application to measure the absorption coefficient of Heraeus 3002 fused silica at 2 µm.

A review of loss mechanisms in transparent materials and current techniques for measuring absorption in low loss materials was presented in Chapter 2. The photothermal technique, in which a probe beam is distorted due to absorption of a beam at the wavelength of interest, was identified as the preferred appproach as it is unaffected by scatter loss.

The system used to measure the probe beam distortion was described in Chapter 3. We chose to use a differential HWS for its proven sensitivity, reproducibility and low cost when compared with other methods. The HWS has the added benifit of imaging the probe beam which leads to more detailed information of the test sample.

Unfortunately, the initial coaxial method was hampered by absorption in the dichroic mirrors used to inject the heating beam. The WFD due to these mirrors was of similar magnitude to that of the test sample necessitating an alternative setup. An off-axis method whiuch allowed injection of the heating beam into the test sample without the use of dichroic mirrors was developed. However, this resulted in an elliptical heating profile rather than a mainly circular profile of the coaxial setup.

The Finite Element Analysis model used to predict the wavefront distortion resulting from optical absorption is described in Chapter 4. The model was validated, at least for highly absorbing material, using a BK7 window.

Examining the reproducibility of the probe beam wavefront when transmitted through the unheated test sample indicated an additional source of noise. A speckle-like aberration due to the rod was observed in the WFD when the heating beam was incident on the dichroic mirror only.

In Section 5.3 we describe a method to reduce the effect of speckle on the Wave Front Deformation by averaging. Comparison of the predicted and measured WFD along semi-major and semi-minor transects yielded a systematic difference between the predicted values with

$$\alpha_{semi-major(x)} = 43.5 \pm 0.5\text{ppm/cm} \pm 3\%$$

$$\alpha_{semi-major(y)} = 46.5 \pm 0.5\text{ppm/cm} \pm 3\%$$

where the 3% systematic error is due to the uncertainty in the calibration of the power meter.

This led to an absorption coefficient of $45 \pm 0.5\text{ppm/cm} \pm 3\%$ for the 3002 FS rod under examination. This is shown in Figure 6.1. This is promising for next generation Gravitational-Wave detectors based on Voyager technologies but may be an issue for higher power detectors such as the proposed OzHF detector.

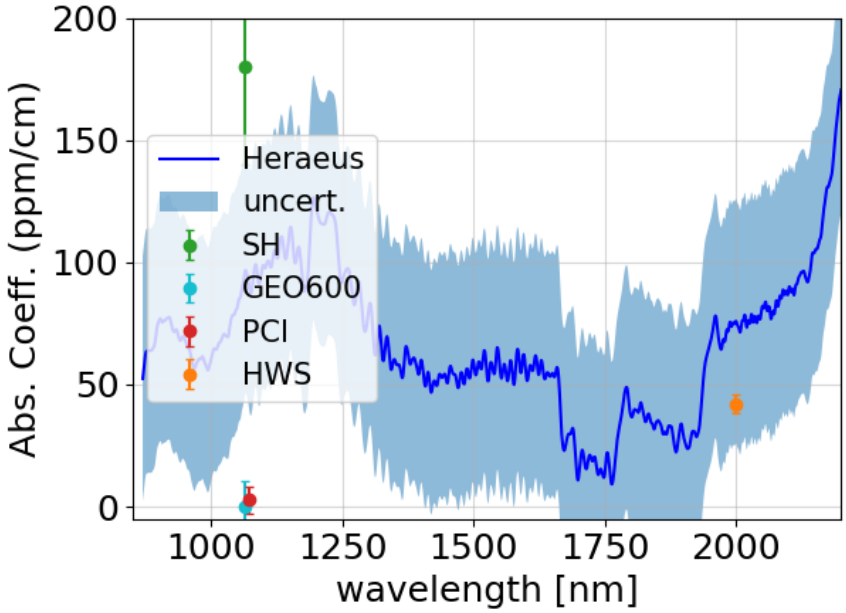

Figure 6.1: Absorption in FS. The blue line indicates the measurements made by Heraeus [1] with shaded region indicating the uncertainty in the measurement (SH [2], GEO600 [3], PCI [4]).

6.2 Future work

The source of the difference between the semi-major and semi-minor axis is unknown. Possible explanations include aberration of the heating beam, as discussed in Section 5.4, and the simple method used to calculate the WFD. We should therefore investigate using alternative methods such as that proposed by Sharma et al. [80] where the optical path length was computed using a series expansion of the refractive index.

It would also be beneficial to fit to the entire wavefront rather than the current method of two transects, as this should improve accuracy of the measurement. This is difficult to implement dut to the off-axis heating beam leaning to higher order deformation of the probe beam.

The source of the speckle-like pattern is also unknown. It could be due to refractive inhomogeneity in the rod or perhaps due to poor polish on the faces of the rod. The source of this need to be investigated.

Preliminary tests have shown that reducing the length of the test sample to 4 com will still resolve a signal large enough to accurately determine the absorption coefficient. If the speckle is due to the inhomogeneity of the test sample then the reduction in optical path length should reduce the noise seen in the WFD.

Reinstating the on-axis measurement system would be beneficial as this may simplify many of the above issues such as fitting to the elliptical gradient field and should reduce profile mismatch due to angle of incidence. To implement this dichroic mirrors with absorption < 10 ppm are required.

In addition to as refining the current measurement technique to place better bounds on uncertainties it is proposed to investigate the other materials such as Silicon and CaF_2 as well as investigate the effect of wavelength on absorption to optimize wavelength choice for next generation detectors.

Appendix A

Linear Approximation of Lambert Beer Law

For short OPL and weakly absorbing material Lambert Beer Law $I = I_0 exp\,[-\alpha z] \approx 1 - \alpha z$ as shown in Figure A.1 using $\alpha = 80$ ppm/cm the linear approximation, orange, does not deviate significantly from the exponential, blue.

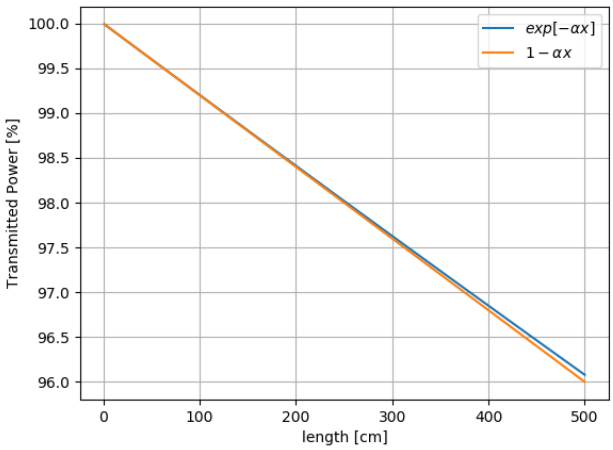

Figure A.1: linear approximation of Lambert Beer Law where $\alpha = 80$ ppm/cm.

Appendix B

Cartesian to spherical transformation

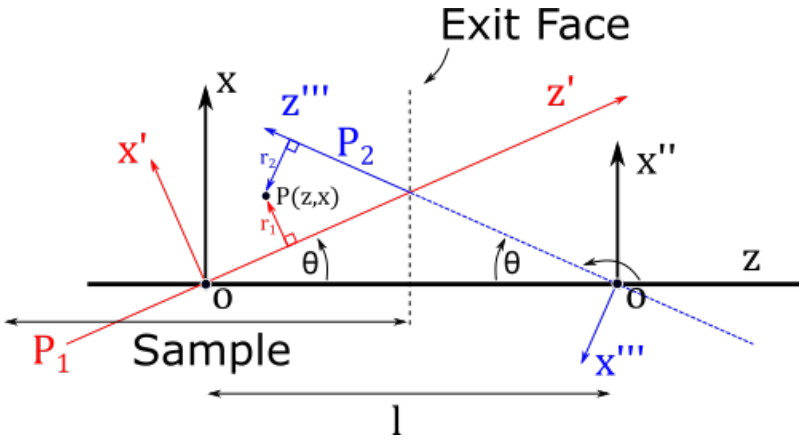

Figure B.1

Coordinate rotation for (1)

$$\begin{bmatrix} z' \\ x' \end{bmatrix} = \begin{bmatrix} cos\theta & sin\theta \\ -sin\theta & cos\theta \end{bmatrix} \begin{bmatrix} z \\ x \end{bmatrix}$$

Coordinate rotation for (2)

$$\begin{bmatrix} z''' \\ x''' \end{bmatrix} = \begin{bmatrix} cos\,(\pi-\theta) & sin\,(\pi-\theta) \\ -sin\,(\pi-\theta) & cos\,(\pi-\theta) \end{bmatrix} \begin{bmatrix} z'' \\ x'' \end{bmatrix}$$

$$= \begin{bmatrix} -cos\theta & sin\theta \\ -sin\theta & -cos\theta \end{bmatrix} \begin{bmatrix} z'' \\ x'' \end{bmatrix}$$

As $P(z,x) = P(z''', x''')$ and $z''' = -l + z, x''' = x$

$$\therefore r_1^2 = (x')^2 = (xcos\theta - zsin\theta)^2 + y^2$$

$$r_2^2 = (x''')^2 = (x''cos\theta - z''sin\theta)^2 + y^2$$

$$= [(xcos\theta - (l + z)\, sin\theta)]^2 + y^2$$

Appendix C

Thermal expansion

Taken from Books [64] Assuming there is a small and uniform increase in temperature, ΔT ,of the Hartmann plate. The increase in separation between two Hartman holes, Δx_{themal}, is given by

$$\Delta x_{themal} = \alpha h_p \Delta T$$

where h_p is the nominal distance between Hartmann Holes and α is the thermal coefficient of expansion of the Hartmann plate.

$$\frac{\partial \Delta W}{\partial x} = \frac{\delta x_{thermal}}{L}$$

$$= \frac{\alpha h_p \Delta T}{L}$$

or more generally

$$\frac{\partial \Delta W}{\partial x} = \frac{\alpha \Delta T}{L} x$$

for a the distance x between any two points. The apparent change in gradient is linear in x and therefore, the apparent change in wavefront is quadratic in x. That is the thermal expansion of the Hartmann Plate (HP) results in a measurement of the primary aberration defocus [83] with a coefficient $S_{thermal}$ given by

$$S_{thermal} = \frac{\alpha \Delta T}{L}$$

Appendix D

Variance in digital value

Determination of the variance in a digitized value. Suppose ones wishes to determine the variance in a value, Ne, which has been digitized on an n-bit scale. The gain, g_D, of this digitization is the ratio of the highest possible value of N_e, $N_{e_{max}}$, and the total number of digital values, 2^n.

$$g_D = \frac{N_{e_{max}}}{2^n} \tag{D.1}$$

All values between ig_D and $(i+1)g_D$ will be rounded down to ig_D in the digization process. Therefore the effective mean of these values is ig_D. If a series of M measurements, x_{e_i}, are made, such that they are all rounded to ig_D, then the variance is given by

$$\begin{aligned} \sigma^2_{digital,M} &= \sum_{j=1}^{M} \frac{\left(x_{e_j} - ig_D\right)^2}{M-1} \\ &= \frac{1}{g_D} \sum_{j=1}^{M} \left(x_{e_j} - ig_D\right)^2 \frac{g_D}{M-1} \end{aligned} \tag{D.2}$$

In the limit that $M \to \text{inf}$, the set of values becomes $\left(x_{e_j} - ig_D\right)$ approaches a continuum, x, that ranges between 0 and g_D, the value $g_D/\left(M-1\right)$ approaches dx, and the variance calculation becomes an integral

$$\begin{aligned} \lim_{M\to\infty} \sigma^2_{digital,M} &= \frac{1}{g_D} \int_0^{g_D} x^2 dx \\ &= \frac{g_D^2}{3} \end{aligned} \tag{D.3}$$

Hence the standard deviation is given by

$$\sigma_{digital} = \frac{1}{\sqrt{3}} \frac{N_{e_{max}}}{2^n} \tag{D.4}$$

Computer code

[ ]:
```
import numpy as np
from scipy.spatial import Delaunay
import math

"Find all edges of triangles from the output of scipy Delaunay triangulation␣
 ↪simplices"

def edgeTri(dt):

#find the maximum index corresponding to the number of points

    max_idx = np.amax(dt)

    dt_shape = np.shape(dt)

    #Row index of an element in dt (#point constructing a triangle)

    dt_row = np.indices(dt_shape)[0]

    #Column index of a element in dt (#triangle)

    dt_col = np.indices(dt_shape)[1]

    edge = np.array([[0,0]])

    for kk in range (0,max_idx): #Looping through all points

        idxrow = np.where(dt == kk)[0] #Find row index of a point in dt

        idxcol = np.where(dt == kk)[1] #Find column index of a point in dt

        noidx  = idxrow.shape[0] #Number of triangles a point is in

        iedge = np.zeros([2*noidx,2]) #For every point ctreate two edges to␣
 ↪connect to other 2 points,

        iedge[:,0] = kk #First column contains origin point

        for idx in range (0,noidx): #Looping through all triangles that apoint␣
 ↪exists in

            #Depending on the column index of apoint, the column indices of the␣
 ↪other points differ
            if idxcol[idx] == 0:

                idx1 = 1
```

```
                idx2 = 2
            elif idxcol[idx] == 1:
                idx1 = 0
                idx2 = 2
            elif idxcol[idx] == 2:
                idx1 = 0
                idx2 = 1
            iedge[2*idx,1] = dt[idxrow[idx],idx1]
            iedge[2*idx+1,1] = dt[idxrow[idx],idx2]
        #Combine all edges:
        edge = np.concatenate((edge,iedge),axis = 0)
    #Delete first row in edge:
    edge = np.delete(edge,0,0)
    #Sort each row into increasing order:
    edge = np.sort(edge,axis=1)
    #Delete duplicate row
    duptest = np.vstack({tuple(row) for row in edge})
    #edge = np.unique(duptest)
    #Rearrange to increasing order of column 1
    edge = edge[edge[:,0].argsort()]
    return edge
```

[ ]:
```
In [1]: %matplotlib widget
```

[ ]:
```
In [2]: # import sys and os
import sys
import os
```

```
# if all the classes are in one folder and this script is in its subfolder,
# one can do this to make the classes available for import:
hspath = os.path.abspath('../..')
if hspath not in sys.path:
sys.path.append(hspath)
# Above code checks first whether the folder containing HS classes are
# already in Python system path, and if not, it includes the folder to
# sys.path so that the classes can be imported. Checking the path first
# ensures that sys.path does not get duplicate entries.

## Import the modules
from HS_Camera import *
from HS_Image import *
from HS_Centroids import *
from HS_Gradients import *
from HS_WFP import *
import HSM_WFN
from scipy.spatial import Delaunay
# for plotting
import matplotlib.pyplot as plt

#find edges
from edgeTri import *
```

[ ]:
```
In [3]: cam = HS_Camera(device_no=0)
```

```
The camera is accessible
```

[ ]:
```
In [9]: fig = plt.figure()
ax1 = fig.add_subplot(111)

# while True:
       for ii in range(100):
        hsi = cam.take_and_average_frames(no_of_frames=1)
%    #hsi = HS_Image(**plane1)
        hsi.background = 200
        hsi.read_image()
        hsi.process_image()

        hsc = HS_Centroids()
        hsc.hsimage = hsi
        hsc.find_centroids()
        cents = hsc.centroids
```

```
            #Use Delaunay triangulation
            tri = Delaunay(cents)
            dt = tri.simplices
            dte = edgeTri(dt)

            dte = dte.astype(int)
            ss = np.sqrt(np.sum((cents[dte[:,0],:]-cents[dte[:,1],:])**2,axis=1))
            ss_sorted = np.sort(ss)
            noe = np.shape(ss_sorted)[0]

            #Take a small sample of sorted spot spacings, calculate mean ans␣
↪stdev
            ss_sample = ss_sorted[(np.int(np.round(noe/2)-10)):np.int((np.
↪round(noe/2)+10))]

            #Mean:
            mean_sample = np.mean(ss_sample)

            #Stdev
            stdev_sample = np.std(ss_sample)

            #     print ("Mean length of sampled edges at plane 1: ",␣
↪mean_sample1)
            #     print ("Standard deviation of sampled edges at plane 1: ", ␣
↪stdev_sample1)

            ax1.clear()
            ax1.grid()
            ax1.hist(ss, bins=25, range=[34, 38], density = False)
            # ax1.hist(ss, bins=20, density = False)
            plt.xlabel('Spacing length')
            plt.ylabel('Count')
            plt.title(f'mean = {mean_sample:0.5}, \n standard deviation␣
↪{stdev_sample:0.5}')
            fig.canvas.draw()
```

```
FigureCanvasNbAgg()
```

[ ]:
```
In [5]: # plt.savefig('col_test.png')

In [6]: plt.figure()
plt.imshow(hsi.original_image, origin='lower')
plt.triplot(cents[:,0], cents[:,1], tri.simplices)
plt.xlim(250,750)
plt.ylim(250,750)
```

```
    # plt.scatter(cents[:,0],cents[:,1], s = 20, color = 'r')

    # plt.plot(points[:,0], points[:,1], 'o')
    # plt.show()
    plt.savefig('collimation_simp.png')
```

```
FigureCanvasNbAgg()
```

[ ]:
```
In [7]: def create_circular_mask(h, w, center=None, radius=None):

    if center is None: # use the middle of the image
    center = [int(w/2), int(h/2)]
    if radius is None: # use the smallest distance between the center and image␣
↪walls
    radius = min(center[0], center[1], w-center[0], h-center[1])

    Y, X = np.ogrid[:h, :w]
    dist_from_center = np.sqrt((X - center[0])**2 + (Y-center[1])**2)

    mask = dist_from_center <= radius
    return mask
```

[ ]:
```
In [8]: plt.figure()
    plt.imshow(hsi.modified_image, origin='lower')
    # plt.plot(cents[:,0], cents[:,1], 'o')

    plt.triplot(cents[:,0], cents[:,1], tri.simplices)
```

```
FigureCanvasNbAgg()
```

```
Out[8]: [<matplotlib.lines.Line2D at 0x7efd931909b0>,
<matplotlib.lines.Line2D at 0x7efd93190da0>]
```

[ ]:
```
In [ ]:
```

Bibliography

[1] Bodo Kuehn. personal communication.

[2] Sanichiro Yoshida, David H Reitze, David B Tanner, and Justin D Mansell. Method for measuring small optical absorption coefficients with use of a shack-hartmann wave-front detector. *Applied optics*, 42(24):4835–4840, 2003.

[3] Stefan Hild, Harald Lück, Walter Winkler, Ken Strain, Hartmut Grote, Joshua Smith, Michaela Malec, Martin Hewitson, Benno Willke, James Hough, and Karsten Danzmann. Measurement of a low-absorption sample of oh-reduced fused silica. *Appl. Opt.*, 45(28):7269–7272, Oct 2006.

[4] K V. Vlasova, Alexandre Makarov, N Andreev, and A Yu. Konstantinov. High-sensitive absorption measurement in transparent isotropic dielectrics with time-resolved photothermal common-path interferometry. *Applied Optics*, 57:6318, 08 2018.

[5] B. P. Abbott, R. Abbott, T. D. Abbott, and et al. Observation of gravitational waves from a binary black hole merger. *Phys. Rev. Lett.*, 116:061102, Feb 2016.

[6] LIGO Scientific Collaboration, Virgo Collaboration, et al. Gwtc-1: a gravitational-wave transient catalog of compact binary mergers observed by ligo and virgo during the first and second observing runs. *arXiv preprint arXiv:1811.12907*, 2018.

[7] Benjamin P Abbott, Rich Abbott, TD Abbott, Fausto Acernese, Kendall Ackley, Carl Adams, Thomas Adams, Paolo Addesso, RX Adhikari, VB Adya, et al. Gw170817: observation of gravitational waves from a binary neutron star inspiral. *Physical Review Letters*, 119(16):161101, 2017.

[8] Benjamin P Abbott, R Abbott, TD Abbott, F Acernese, K Ackley, C Adams, T Adams, P Addesso, RX Adhikari, VB Adya, et al. Gravitational waves and gamma-rays from a binary neutron star merger: Gw170817 and grb 170817a. *The Astrophysical Journal Letters*, 848(2):L13, 2017.

[9] Henri Poincaré. *La dynamique de l'électron (On the dynamics of electron)*. A. Dumas, 1913.

[10] Gregory M Harry, LIGO Scientific Collaboration, et al. Advanced ligo: the next generation of gravitational wave detectors. *Classical and Quantum Gravity*, 27(8):084006, 2010.

[11] Korey Haynes and Eric Betz. A wrinkle in space-time confirms einstein's gravitation. *Astronomy May*, pages 23–5, 2016.

[12] B. P. Abbott, R. Abbott, T. D. Abbott, and et al. Properties of the binary black hole merger gw150914. *Phys. Rev. Lett.*, 116:241102, Jun 2016.

[13] Benjamin P Abbott, R Abbott, TD Abbott, F Acernese, K Ackley, C Adams, T Adams, P Addesso, RX Adhikari, VB Adya, et al. First narrow-band search for continuous gravitational waves from known pulsars in advanced detector data. *Physical Review D*, 96(12):122006, 2017.

[14] David G Blair, EJ Howell, L Ju, and C Zhao. *Advanced gravitational wave detectors*. Cambridge University Press, 2012.

[15] Joseph Romano and Neil. Cornish. Detection methods for stochastic gravitational-wave backgrounds: a unified treatment. *Living Reviews in Relativity*, 20(1):1–223, 2017.

[16] Nelson Christensen. Stochastic gravitational wave backgrounds. *Reports on Progress in Physics*, 82(1):016903, Nov 2018.

[17] Johannes Noller and Scott Melville. The coupling to matter in massive, bi- and multi-gravity. *Journal of Cosmology and Astroparticle Physics*, 2015(01):003, 2015.

[18] Junaid Aasi, BP Abbott, Richard Abbott, Thomas Abbott, MR Abernathy, Kendall Ackley, Carl Adams, Thomas Adams, Paolo Addesso, RX Adhikari, et al. Advanced ligo. *Classical and quantum gravity*, 32(7):074001, 2015.

[19] Muzammil A. Arain and Guido Mueller. Design of the advanced ligo recycling cavities. *Opt. Express*, 16(14):10018–10032, Jul 2008.

[20] LIGO Scientific Collaboration. Instrument science white paper, ligo-t1600119–v4. Technical Report LIGO-T1600119–v4, California Institute of Technology, Massachusetts Institute of Technology, LIGO Hanford Observatory, LIGO Livingston Observatory, October 2016.

[21] M G Beker, J F J van den Brand, E Hennes, and D S Rabeling. Newtonian noise and ambient ground motion for gravitational wave detectors. *Journal of Physics: Conference Series*, 363:012004, jun 2012.

[22] Daniel Sigg. The advanced ligo detectors in the era of first discoveries. In *Interferometry XVIII*, volume 9960, page 996009. International Society for Optics and Photonics, 2016.

[23] Giles Hammond, Stefan Hild, and Matthew Pitkin. Advanced technologies for future laser-interferometric gravitational wave detectors. *Journal of Modern Optics*, 61, 02 2014.

[24] Aaron Gillespie and Fred Raab. Suspension losses in the pendula of laser interferometer gravitational-wave detectors. *Physics Letters A*, 190(3-4):213–220, 1994.

[25] AV Cumming, AS Bell, L Barsotti, MA Barton, G Cagnoli, D Cook, L Cunningham, M Evans, GD Hammond, GM Harry, et al. Design and development of the advanced ligo monolithic fused silica suspension. *Classical and Quantum Gravity*, 29(3):035003, 2012.

[26] Michele Heurs. Gravitational wave detection using laser interferometry beyond the standard quantum limit. *Philosophical Transactions of the Royal Society A: Mathematical, Physical and Engineering Sciences*, 376(2120):20170289, 2018.

[27] Stefan L. Danilishin and Farid Ya. Khalili. Quantum measurement theory in gravitational-wave detectors. *Living Reviews in Relativity*, 15(1):5, Apr 2012.

[28] Junaid Aasi, J Abadie, BP Abbott, Richard Abbott, TD Abbott, MR Abernathy, Carl Adams, Thomas Adams, Paolo Addesso, RX Adhikari, et al. Enhanced sensitivity of the ligo gravitational wave detector by using squeezed states of light. *Nature Photonics*, 7(8):613, 2013.

[29] Aidan F Brooks, Benjamin Abbott, Muzammil A Arain, Giacomo Ciani, Ayodele Cole, Greg Grabeel, Eric Gustafson, Chris Guido, Matthew Heintze, Alastair Heptonstall, et al. Overview of advanced ligo adaptive optics. *Applied optics*, 55(29):8256–8265, 2016.

[30] Patrice Hello and Jean-Yves Vinet. Analytical models of thermal aberrations in massive mirrors heated by high power laser beams. *Journal de Physique*, 51(12):1267–1282, 1990.

[31] Walter Winkler, Karsten Danzmann, Albrecht Rüdiger, and Roland Schilling. Heating by optical absorption and the performance of interferometric gravitational-wave detectors. *Physical Review A*, 44(11):7022, 1991.

[32] Aidan F Brooks, Thu-Lan Kelly, Peter J Veitch, and Jesper Munch. Ultrasensitive wavefront measurement using a hartmann sensor. *Optics express*, 15(16):10370–10375, 2007.

[33] A Rocchi, E Coccia, V Fafone, V Malvezzi, Y Minenkov, and L Sperandio. Thermal effects and their compensation in advanced virgo. *Journal of Physics: Conference Series*, 363, 06 2012.

[34] Aidan Brooks, Gabriele Vajente, Daniel Brown, Hiro Yamamoto, Evan Hall, GariLynn Kasprzack, Marie Billingsley, et al. The point absorbers and aligo, ligo-g1900203-v5. Technical Report LIGO-G1900203-v5, California Institute of Technology, Massachusetts Institute of Technology, LIGO Hanford Observatory, LIGO Livingston Observatory, October 2016.

[35] N. Smith, A. Brooks, E. Gustafson, D. Coyne, R. Adhikari, L. Barsotti, and B. Shapiro. Ligo voyager upgrade concept. *https: //dcc.ligo.org/LIGO-T1400226.*, 2019.

[36] Heraeus Transmission Calculator, Jun 2019. [Online; accessed 11. Jun. 2019].

[37] A K Sivadasan. *Optical Properties of AlGaN Nanostructures.* PhD thesis, Indira Gandhi Centre for Atomic Research Chennai, Tamil Nadu, India, 03 2017.

[38] Frank L. Pedrotti. *Introduction to optics.* Pearson Prentice Hall, Upper Saddle River, N.J. ; Sydney, 3rd ed. / frank l. pedrotti, leno s. pedrotti, leno m. pedrotti. edition, 2007.

[39] Harold Earl Bennett. Scattering characteristics of optical materials. *Optical Engineering*, 17(5):175480, 1978.

[40] RJ Shine, AJ Alfrey, and RL Byer. 40-w cw, tem 00-mode, diode-laser-pumped, nd: Yag miniature-slab laser. *Optics letters*, 20(5):459–461, 1995.

[41] Xu Chen, Li Ju, Raffaele Flaminio, Harald Lück, Chunnong Zhao, and David G Blair. Rayleigh scattering in fused silica samples for gravitational wave detectors. *Optics Communications*, 284(19):4732–4737, 2011.

[42] Laura Johnson, Faezah Jasman, R.J. Green, and Mark Leeson. Recent advances in underwater optical wireless communications. *Underwater Technology*, 32:167–175, 09 2014.

[43] Heraeus Quarzglas and Germany Hanau. Catalogue "quartz glass for optics. *Data and properties*, 2017.

[44] ME Lines. Can the minimum attenuation of fused silica be significantly reduced by small compositional variations? *Journal of non-crystalline solids*, 171(3):209–218, 1994.

[45] M Sparks and LJ Sham. Theory of multiphonon absorption in insulating crystals. *Physical Review B*, 8(6):3037, 1973.

[46] M.E. Lines. Can the minimum attenuation of fused silica be significantly reduced by small compositional variations? ii. combined fluorine and alkali metal dopants. *Journal of Non-Crystalline Solids*, 171(3):219–227, 1994.

[47] CR Elliott and GR Newns. Near infrared absorption spectra of silica: Oh overtones. *Applied Spectroscopy*, 25(3):378–379, 1971.

[48] Oliver Humbach, H Fabian, U Grzesik, U Haken, and W Heitmann. Analysis of oh absorption bands in synthetic silica. *Journal of non-crystalline solids*, 203:19–26, 1996.

[49] Sieghard Albert, Karen Keppler Albert, and Martin Quack. High-resolution fourier transform infrared spectroscopy. *Handbook of High-resolution Spectroscopy*, 2011.

[50] John Chalmers and Peter Griffiths. *Handbook of Vibrational Spectroscopy, 5 volumes set.* Wiley, 2002.

[51] Maurice Hui, Rongqing ; O'Sullivan. *Fiber Optic Measurement Techniques*. Elsevier Science, 2008.

[52] RCC Leite, RS Moore, and JR Whinnery. Low absorption measurements by means of the thermal lens effect using an he–ne laser. *Applied Physics Letters*, 5(7):141–143, 1964.

[53] DC Burnham. Simple measurement of thermal lensing effects in laser rods. *Applied optics*, 9(7):1727–1728, 1970.

[54] J Murray. Pulsed gain and thermal lensing of nd: Liyf 4. *IEEE Journal of Quantum Electronics*, 19(4):488–491, 1983.

[55] Warren B Jackson, Nabi1 M Amer, AC Boccara, and D Fournier. Photothermal deflection spectroscopy and detection. *Applied optics*, 20(8):1333–1344, 1981.

[56] Vincent Loriette and Claude Boccara. Absorption of low-loss optical materials measured at 1064 nm by a position-modulated collinear photothermal detection technique. *Appl. Opt.*, 42(4):649–656, Feb 2003.

[57] Alexei Alexandrovski, Martin Fejer, A Markosian, and Roger Route. Photothermal common-path interferometry (pci): new developments. *Proceedings of SPIE - The International Society for Optical Engineering*, 7193, 02 2009.

[58] Alexander Chernyshov, Uwe Sterr, Fritz Riehle, Jürgen Helmcke, and Johannes Pfund. Calibration of a shack–hartmann sensor for absolute measurements of wavefronts. *Applied optics*, 44(30):6419–6425, 2005.

[59] H Lehmann. Application of hartmann's method of zonal testing to astronomical objectives. *Zt. Instrumentenkd*, 22:325–330, 1902.

[60] J. A. Miller and R. W. Marriott. Zone-tests of telescope objective. *J. Franklin I*, 178:465 – 481, 1914.

[61] Daniel Malacara-Hernandez and Zacarias Malacara. Testing and centering of lenses by means of a hartmann test with four holes. *Optical Engineering*, 31(7):1551–1556, 1992.

[62] François Roddier. *Adaptive optics in astronomy*. Cambridge university press, 1999.

[63] Ben C Platt and Roland Shack. History and principles of shack-hartmann wavefront sensing. *Journal of refractive surgery*, 17(5):S573–S577, 2001.

[64] Aidan Francis Brooks. *Hartmann wavefront sensors for advanced gravitational wave interferometers*. PhD thesis, The University of Adelaide, 7 2007.

[65] J.L Rayces. Exact relation between wave aberration and ray aberration. *Optica Acta: International Journal of Optics*, 11(2):85–88, 1964.

[66] JL Rayces. Exact relation between wave aberration and ray aberration. *Optica Acta: International Journal of Optics*, 11(2):85–88, 1964.

[67] William H Southwell. Wave-front estimation from wave-front slope measurements. *JOSA*, 70(8):998–1006, 1980.

[68] Zhiling Jiang, Shunsheng Gong, and Yang Dai. Monte-carlo analysis of centroid detected accuracy for wavefront sensor. *Optics & Laser Technology*, 37(7):541–546, 2005.

[69] Stacy R Kamasz, Surendra P Singh, S Gareth Ingram, Martin J Kiik, Queintin Tang, and Brian Benwell. Enhanced full well for vertical antiblooming, high sensitivity time-delay and integration (tdi) ccds with ghz data rates. *IEEE Workshop on Charge-Coupled Devices and Advanced Image Sensors*, 06 2001.

[70] DALSA Inc. *Application Note: Vertical Antiblooming*, 2004.

[71] DALSA Inc. *Pantera TF 1M60 and 1M30, 1K × 1K Progressive Scan Monochrome Camera, User's Manual and Reference*, 2004.

[72] DALSA Inc. *1M Frame Transfer CCD Image Sensor*, 2004.

[73] Peter J Winzer. Shot-noise formula for time-varying photon rates: a general derivation. *JOSA B*, 14(10):2424–2429, 1997.

[74] B Picinbono, C Bendjaballah, and Jean Pouget. Photoelectron shot noise. *Journal of Mathematical Physics*, 11(7):2166–2176, 1970.

[75] Spectral calculator-hi-resolution gas spectra. `https://www.spectralcalc.com/calc/spectralcalc.php`. (Accessed on 11/14/2019).

[76] Francois Roddier. Wavefront sensing and the irradiance transport equation. *Applied optics*, 29(10):1402–1403, 1990.

[77] 0yvind Hjelle and Morten Dæhlen. *Triangulations and Applications*. Mathematics and Visualization. Springer Berlin Heidelberg, Berlin, Heidelberg, 2006.

[78] Anthony F. Mills. *Heat transfer / A.F. Mills.* Prentice Hall, Upper Saddler River, N.J., 2nd ed. edition, 1999.

[79] COMSOL AB. Comsol multiphysics ®.

[80] Anurag Sharma. Computing optical path length in gradient-index media: a fast and accurate method. *Applied Optics*, 24(24):4367, 1985.

[81] Jihoon Kim, Junghwan Oh, and Thomas E Milner. Measurement of optical path length change following pulsed laser irradiation using differential phase optical coherence tomography. *Journal of biomedical optics*, 11(4):041122, 2006.

[82] Refractive index info. [Online:Accessed on 09/20/2019].

[83] Zacarias Malacara and Manuel Servin. *Interferogram analysis for optical testing*. CRC press, 2016.